Effects of Surface Properties on Solder Bump Formation by Direct Droplet Deposition

by

Wen-Kai Hsiao

S.B. Mechanical Engineering
University of California, Santa Barbara, 1995

M.S. Mechanical Engineering
Massachusetts Institute of Technology, 1998

Submitted to the Department of Mechanical Engineering
in Partial Fulfillment of the Requirements for the Degree of

DOCTOR OF PHILOSOPHY IN MECHANICAL ENGINEERING

at the

MASSACHUSETTS INSTITUTE OF TECHNOLOGY

June 2004

© 2004 Massachusetts Institute of Technology
All Rights Reserved

Signature of Author:______________________________________
Department of Mechanical Engineering
April 30, 2004

Certified by:______________________________________
Jung-Hoon Chun
Professor of Mechanical Engineering
Chairman, Doctoral Thesis Committee

Accepted by:__________________________
Ain A. Sonin
Professor of Mechanical Engineering
Chairman, Department Graduate Committe

MASSACHUSETTS INSTITUTE OF TECHNOLOGY

JUL 20 2004

LIBRARIES

BARKER

Effects of Surface Properties on Solder Bump Formation by Direct Droplet Deposition

by

Wen-Kai Hsiao

Submitted to the Department of Mechanical Engineering
on April 30, 2004 in Partial Fulfillment of the Requirements for the Degree of
Doctor of Philosophy in Mechanical Engineering

ABSTRACT

Recent advances in microdroplet generation and deposition processes have made it possible to directly form solder bumps on integrated circuits using micron-sized molten metal droplets. The direct droplet deposition bumping process can potentially produce uniform-sized bumps more economically than the existing processes such as plating and stencil printing. However, the development of this new bumping method is still in its infancy, particularly because of a lack of understanding about the post-impact deposition behavior of molten droplets on solid targets. A deposited molten droplet can sometimes recoil violently after the initial spreading and rebound off the target surface. Such behavior, known as bouncing, has a strong influence on the deposition efficiency, as well as on the final bump size and shape.

The present study investigates the effects of wetting and surface roughness on droplet bouncing during solder bump formation. The potential for droplet bouncing is modeled based on the energy difference between the maximum spreading and equilibrium sessile stages of a deposited droplet. Validated by experimental results, the model shows that strong droplet-surface wetting can significantly reduce the tendency for a deposited droplet to bounce. The effect of surface roughness on the bouncing potential is represented by the roughness-induced incomplete wetting during droplet deposition, a phenomenon quantified by a change in the effective contact area under the deposited droplet. An idealized surface model is used to represent the real surface and to describe the relationship between various roughness parameters to changes in the effective contact area. The theoretical analysis, validated by empirical data, shows that surface roughness promotes bouncing during solder bump formation.

The results from this study suggest that droplet bouncing during solder bump formation may be effectively controlled by improving the surface wetting and minimizing the substrate surface roughness. The knowledge gained is also relevant to other droplet-based manufacturing processes such as spray forming, coating, and rapid prototyping.

Thesis Committee:

Prof. Jung-Hoon Chun (Chairman), Department of Mechanical Engineering
Prof. Rafael Reif, Department of Electrical Engineering and Computer Science
Dr. Nannaji Saka, Department of Mechanical Engineering

ACKNOWLEDGMENTS

There are many people without whose helps this thesis may never come to be (many of them would say that sometimes it looked like it never will).

First and foremost, I would like to thank my advisor, Prof. Jung-Hoon Chun, for his guidance and patience over the years.

My sincere gratitude also goes to my thesis committee members, Prof. Rafael Reif and Dr. Nannaji Saka, for their feedbacks and suggestions. I will particularly miss those discussion (and pipe-puffing) sessions I had with Dr. Saka behind Building 35 and in the smoking garden.

This research was sponsored by the DBM Consortium member companies and the Singapore-MIT Alliance. I would also like to acknowledge the contributions of the following parties: Dr. Ronald Morrissey and Mr. John Litterio of Technic Inc. for their helps in preparing the test substrates, Mr. Gene O'Connell of Tech Imaging Services Inc. for providing the high-speed imaging equipment, and Mr. Brian Anthony of Xcitex Inc. for the image processing software and support. In addition, I am grateful to Dr. James Bales for introducing me to the nuances of high-speed imaging techniques and Ali Mazalek for helping me processing the image data. I would also like to express my appreciation to Yin-Lin Xie and Dr. Nil Chatterjee for their assistances with preparing and imaging my many metallographic samples.

I am honored to have the chance to work with many truly excellent students and researchers during my tenure in LMP and the DBM Laboratory. Special thanks to Dr. Ho-Young Kim, whose research seeded my own exploration. I am especially grateful to have Dr. Jeanie Cherng as my sole companion in the lab during the later years, whose intelligence and determination always set a high standard for me. I would also like to thank Fred Cote, my surrogate father in MIT, for his continuous support in the machine shop and those canoe trips down the mighty Neponset River.

I am grateful to my friends, whose fellowships are indispensable parts of my experience here in MIT. I would particularly like to thank Kevin Otto, Raj Suri, Kan Ota, and Javier Gonzalez-Zugasti for their tolerance of my constant whining.

I credit my relative sanity after years of graduate study to the Thirsty Ear Pub and the fellow bartenders whom I have the pleasure to work with.

Finally, I would like to dedicate this thesis to my parents, Chin-Kun Hsiao and Mei-Chih Yeh, for their unwavering support while I indulged in this endeavor for as long as I did.

TABLE OF CONTENTS

ABSTRACT **2**

ACKNOWLEDGMENTS **3**

TABLE OF CONTENTS **4**

LIST OF FIGURES **6**

LIST OF TABLES **9**

CHAPTER 1. INTRODUCTION **10**

1.1 Background 10
1.2 Solder Bumping Methods 11
1.2.1 Evaporation 11
1.2.2 Electroplating 12
1.2.3 Stencil printing 12
1.2.4 Ball placement 13
1.2.5 Direct droplet deposition 13
1.3 Developmental Issues of Direct Droplet Deposition Bumping 14
1.3.1 Generation of uniform-sized solder droplets 14
1.3.2 Deflection and trajectory control of the solder droplets 15
1.3.3 Post-deposition solder bump formation 15
1.4 Thesis Motivation and Scope 17
1.5 Thesis Organization 18

CHAPTER 2. ANALYTICAL WORK **29**

2.1 Introduction 29
2.2 Isothermal, Post-impact Droplet Deformation Processes 32
2.2.1 Stage 1: Impact 33
2.2.2 Stage 2: Maximum spreading 34
2.2.3 Stage 3: Maximum retraction 37
2.2.4 Stage 4*: Bouncing (complete and partial) 38
2.2.5 Stage 4: Equilibrium 40
2.3 Potential for Droplet Bouncing 42
2.3.1 Estimation of the maximum spreading diameter 44
2.4 Effect of Roughness on Droplet-Surface Wetting During Deposition 47
2.4.1 Modeling of melt-surface interaction 50
2.5 Bouncing Criterion 53
2.5.1 Effect of droplet-surface wetting 54
2.5.2 Effect of surface roughness 55
2.6 Summary 56

CHAPTER 3. EXPERIMENTAL WORK...71

3.1 Introduction...71
3.2 Droplet Generation...71
3.3 Substrate Preparation...72
3.4 Solder Bump Morphology Study...76
3.4.1 Experimental apparatus and procedures...76
3.4.2 Observations...77
3.5 High-speed Imaging Study...80
3.5.1 Experimental apparatus and procedures...82
3.5.2 Observations...84

CHAPTER 4. MODEL VALIDATION AND DISCUSSION...116

4.1 Introduction...116
4.2 Concept Validation: Differential Surface Energy as Bouncing Potential...119
4.2.1 Image processing and droplet diameter evolution...119
4.2.2 Droplet surface area evolution...124
4.2.3 Differential surface energy dynamics...127
4.3 Concept Validation: Roughness Effect on Droplet-Surface Wetting...128
4.3.1 Characterization of the test substrate surfaces...129
4.3.2 Effective area fraction and adjusted contact angle...131
4.4 Bouncing Criterion Quantification...132
4.4.1 Estimations of the maximum spreading diameter...133
4.4.2 Bouncing criterion trends and threshold of transition...133
4.5 Summary...136

CHAPTER 5. CONCLUSIONS...153

5.1 Summary of Findings...153
5.2 Future Work...156

REFERENCES...158

APPENDIX...163

LIST OF FIGURES

Figure 1.1 An integrated circuit (IC) based electronic system.................................. 19

Figure 1.2 Integrated circuit technology trends... 20

Figure 1.3 I/O capacities of the peripheral and area-array packages compared to the projected requirements... 21

Figure 1.4 Schematic of a continuous-jetting, direct droplet deposition bumping system...23

Figure 1.5 Schematic of a Uniform Droplet Spray (UDS) generator........................... 24

Figure 1.6 Schematic of the droplet trajectory control system.................................. 25

Figure 1.7 Splashing of molten droplet...26

Figure 1.8 Bouncing of a Sn droplet deposited on heated Al surface..........................27

Figure 1.9 Sticking and bouncing regime map of molten Sn droplet deposition..............27

Figure 1.10 Images of (a) a quenched Sn splat (original droplet diameter: 2.6mm), and (b) contact pads shorted after the deposited droplets are reflowed..................... 28

Figure 2.1 Sn bumps formed on surfaces with different roughness..............................58

Figure 2.2 The four regions of low to moderate We droplet deposition.........................59

Figure 2.3 Post-impact droplet deformation processes...60

Figure 2.4 Dynamics of the apparent melt-surface contact angle.................................61

Figure 2.5 Apparent contact angle as a function of the contact line velocity.................. 62

Figure 2.6 Energy difference between the maximum spreading and equilibrium states as potential for droplet bouncing...63

Figure 2.7 Highlighted void formations shown at the interface of a Sn bump deposited on Au-plated, as-rolled Al plate... 64

Figure 2.8 Roughness-induced gas entrapments and the resulting composite melt-surface interface.. 64

Figure 2.9 Schematic describing the effective area fraction, $F_a = A_{eff} / A_{real}$.................. 64

Figure 2.10 Schematic of the force components controlling melt penetration 65

Figure 2.11 Schematic of the generalized rough surface model....................................66

Figure 2.12 Characteristics of the interfacial voids formed between solder bumps and rough surfaces... 67

Figure 2.13 Illustration of the waviness, roughness, and general form of a surface............67

Figure 2.14 Force balance at the interface between the penetrating melt and the trapped gas in a conical notch.. 68

Figure 2.15 The melt penetration ratio y_p/h, as a function of the notch angle Φ..............69
Figure 2.16 The effective area fraction, F_a, as a function of melt penetration ratio, y_p/h.....69
Figure 2.17 The effect of melt-surface wetting, represented by the equilibrium contact angle, θ_e, on the bouncing criterion..70
Figure 2.18 The effect of surface roughness, represented by the effective area fraction, F_a, on the bouncing criterion..70
Figure 3.1 Uniform Droplet Spray generator..87
Figure 3.2 Schematic of a typical solder bump interconnect.....................................89
Figure 3.3 Quantification procedures for the wetting property of the prepared substrate....89
Figure 3.4 Schematic and images of the apparatus for the droplet deposition experiments..91
Figure 3.5 Details of the testing jig for the bump morphology study..........................92
Figure 3.6 Break-up of the uniform –sized pure Sn droplets.......................................93
Figure 3.7(a) Morphologies of Sn bumps formed on polished Al surface........................94
Figure 3.7(b) Morphologies of Sn bumps formed on polished Cu surface........................95
Figure 3.7(c) Morphologies of Sn bumps formed on Ni-P-plated surface........................96
Figure 3.7(d) Morphologies of Sn bumps formed on Sn-plated surface..........................97
Figure 3.7(e) Morphologies of Sn bumps formed on Rh-plated surface..........................98
Figure 3.7(f) Morphologies of Sn bumps formed on Au-plated surface..........................99
Figure 3.7(g) Morphologies of Sn bumps formed on Pd-plated surface..........................100
Figure 3.8 Remnant and residue of a Sn bump on Ni-P surface..................................101
Figure 3.9 Formation of satellites in a UDS spray..102
Figure 3.10(a) Morphologies of Sn bumps formed on Au-plated, 180μm Al_2O_3 sandblasted surface..103
Figure 3.10(b) Morphologies of Sn bumps formed on Au-plated, 27μm Al_2O_3 sandblasted surface..104
Figure 3.10(c) Morphologies of Sn bumps formed on Au-plated, 0.3μm Al_2O_3 slurry polished surface..105
Figure 3.11 Residue next to a Sn bump on Au-plated, 27μm Al_2O_3 sandblasted surface....106
Figure 3.12 Schematics of (a) the test coupon and (b) the optical set-up of the high-speed imaging experiments...107
Figure 3.13 Details of the testing jig for the high-speed imaging experiments................108
Figure 3.14 Schematic and image of the apparatus for the high-speed imaging study........109
Figure 3.15(a) Droplet exhibits bouncing behavior on Sn (oxide)-plated surface................110
Figure 3.15(b) Droplet exhibits partial bouncing behavior on Rh-plated surface................111

Figure 3.15(c) Droplet exhibits sticking behavior on Pd-plated surface........................112
Figure 3.16(a) Droplet exhibits sticking behavior on Au-plated, 0.3μm Al_2O_3 slurry polished surface........................113
Figure 3.16(b) Droplet exhibits sticking behavior on Au-plated, 27μm Al_2O_3 sandblasted surface........................114
Figure 3.16(c) Droplet exhibits necking behavior on Au-plated, 180μm Al_2O_3 sandblasted surface........................115
Figure 4.1 Measurement uncertainty induced by the blurring of the high-speed image.....138
Figure 4.2 Feature tracking of an object in motion........................138
Figure 4.3 Schematics of image processing using the 1-D line tracking function...........139
Figure 4.4 Processing high-speed images using the 1-D line tracking function in MiDAS........................140
Figure 4.5 Tracking errors introduced by highlight intercepting with the measuring line........................140
Figure 4.6 Evolution of the droplet base diameter on surfaces with different melt-surface wetting conditions........................141
Figure 4.7 Cylindrical shape model for a deforming droplet........................142
Figure 4.8 Evolution of the droplet surface area, extracted from the diameter data using the cylindrical shape model........................142
Figure 4.9 Evolution of the differential surface energy (ΔSE_d) of droplets deposited on surfaces with different melt-surface wetting conditions........................143
Figure 4.10 Zygo NewView 5000 optical profilometer system........................144
Figure 4.11(a) Surface characteristics of 0.3 Al_2O_3 slurry polished surface with Au-plating... 145
Figure 4.11(b) Surface characteristics of 27 Al_2O_3 particle sandblasted surface with Au-plating........................146
Figure 4.11(c) Surface characteristics of 180 Al_2O_3 particle sandblasted surface with Au-plating........................145
Figure 4.12 Droplets exhibit similar initial spreading dynamics when deposited on surfaces with different wetting conditions........................149
Figure 4.13 Threshold of transition determined by comparing empirical data to the model predictions........................150
Figure 4.14 Local variations of the surface wetting condition on 27μm Al_2O_3 sandblasted surface........................151
Figure 4.15 Variations of the droplet deformation processes on poor-wetting and roughened surfaces........................152
Figure A.1 Droplet spreading model for spreading time estimation........................ 166

LIST OF TABLES

Table 1.1 Solder bumping methods summary..22

Table 3.1 The droplet generation parameters for the experimental study.......................88

Table 3.2 Summary of the substrate preparations and the resulting wetting properties...... 90

Table 3.3 Summary of the substrate preparations and the resulting roughness properties.... 90

Table 4.1 Measured and simulated defect characteristics of the test substrates..............148

Table 4.2 Measured and simulated wetting characteristics of the test substrates........... 148

Chapter 1. INTRODUCTION

1.1 Background

The electronics systems industries, spurred on by the inventions of integrated circuits (IC) in 1958, have been growing steadily at a rapid pace. The new generation of electronics products is based on semiconductor IC chips packaged and mounted on circuit boards and interconnected with other parts of the electronic systems, as shown in Figure 1.1. The advancements made in semiconductor technology and the induction of the information age, signified by the popularizations of the internet, mobile computing and telecommunication, have made possible and created demands for smaller electronic devices with more functionalities. The reduced sizes and enhanced capabilities of these microelectronic devices are results of high performance IC chips that are increasingly more complex. Consequently, packaging of these IC chips has become a considerable manufacturing challenge.

Packaging of a semiconductor IC chip involves providing an input/output (I/O) interconnection system that injects power and relays signals to and from the encapsulated chip. The number of I/Os required per chip is shown to be proportional to the complexity of the IC chip [Bakoglu, 1990]. The exponential growth in the chip complexity, as shown in Figure 1.2, has rendered the traditional peripheral packaging solutions, such as dual inline package (DIP) and quad flat pack (QFP), inadequate when compared to the newer area-array packaging solutions. Instead of peripheral fine-pitched leads, the area-array packages place their interconnections on the interior chip surface area. As shown in Figure 1.3, the area-array arrangement allows a much greater number of connections for a given package size.

The most common of the area-array packages consists of ball grid array (BGA) packages and flip chips; packages that utilize solder bumps formed on connection pads on either printed circuit board (PCB) substrates or IC chips as interconnections. The advantages of using solder bumps as interconnections include short lead lengths with lower inductance, better thermal performance, and lower overall profiles. However, realizing these advantages requires forming these bumps,

commonly referred to as solder bumping, reliably and efficiently. There have been a number of manufacturing processes developed to perform solder bumping and they will be reviewed below.

1.2 Solder Bumping Methods

The established and developing solder bumping processes currently comprise evaporation, electroplating, stencil printing, ball placement, and direct droplet deposition. Each process will be described in detail in the following sections. A summary is shown in Table 1.1 that lists the advantages and disadvantages of each process.

1.2.1 Evaporation

Evaporation solder bumping has been developed by IBM as a core technology of its controlled collapse chip connection (C4) process for wafer bumping [Miller, 1969]. The multi-step process involves deposition of metals onto a processed semiconductor wafer through vapor evaporation. The solder bump materials are deposited onto wafer contact pads selectively using metal masks. Two masks are generally required. A mask with smaller openings is used first to deposit the metals needed for the under-bump metallurgy (UBM), which typically consist of layers of chromium (Cr), copper (Cu) and gold (Au). A second mask with larger opening is then used to deposit lead (Pb)-tin (Sn) solders over the UBMs. The deposited solders are then reflowed to form truncated spherical bumps on wafer. The method is a mature process employing standard wafer fabrication techniques and equipment. However, due to the significant difference in the evaporation rates of Pb and Sn, the process is usually applied only to form bumps using high-Pb solders such as Pb-95wt% Sn and Pb-97wt% Sn. As the electronics industries progress to adapt Pb-free solders, the process may become less appropriate. The evaporation solder bumping is generally done in batches of more than 10 wafers due to the slow evaporative deposition rate. A process failure, therefore, may result in the loss of a complete wafer batch. As the wafer size and chip complexity increase, the value of a fully processed wafer becomes very high by the time it reaches the evaporation bumping stage. Estimates of wafer value at this point are $10,000 for 200 mm wafers and $40,000-$50,000 for microprocessor-laden 300 mm wafers [Marx *et al.*, 1998]. The monetary risk hence makes a faster process that allows single-wafer bumping desirable.

1.2.2 Electroplating

Alternatively, solder bump materials may be deposited onto the wafer contact pads through electroplating. The plating process involves overlaying a processed wafer with resist and defining the bump pattern into the resist coating using a mask and standard lithography techniques. The coated wafer is then placed in a plating bath where UBM metals and a final layer of Pb-Sn solders are deposited sequentially into the resist openings. After the metal plating is completed, the resist is removed and the solders are reflowed to form bumps over the wafer pads. The process has become increasingly popular since it allows deposition of solders in any composition, including Pb-37wt% Sn eutectic solder. In addition, it is generally more economical than the evaporation process since only one mask is required. However, bump height irregularity is a major issue of the electroplating method. The deposition rate of the electroplating process is proportional to the current density. Since the electrical current is generally applied at the edge of the wafer during the plating process, the current density variations across the wafer often result in greater bump heights for the dies at the edge than those near the center of the wafer [Lao and Pao, 1997]. In addition, the plating process is slow at 0.5-1μm per minute, and hence limits the sizes of the bumps it can form economically.

1.2.3 Stencil printing

Wafer bumping by stencil printing is a low-cost alternative to both evaporation and electroplating processes. The solder materials are mixed with fluxes to produce solder pastes. The pastes are then printed onto electroless nickel (Ni-P)-Au UBMs on wafer pads through a stencil. The solder pastes are then reflowed to form solder bumps. This bumping method is particularly attractive to electronics system manufacturers since stencil printing of solder paste is a common and mature process for the manufacturing of surface mount technology (SMT) devices. However, achieving uniform bump heights using the stencil printing method requires careful controls of the rheology of the solder paste, squeegee force and speed, and quality and cleanliness of the stencil used. In addition, printing fine pitch bumps is difficult using this method, and the current pitch limit for volume production is around 0.15mm.

1.2.4 Ball placement

The main issues of the electroplating and stencil printing methods, as described in the previous sections, are low metal deposition rate and non-uniform bump heights. To address these issues, a process has been developed to place and reflow preformed solder spheres onto wafer or PCB substrates to form solder bumps. The ball placement method transfers the required volumes of solder onto the contact pads in one step to achieve very uniform bump heights. In addition, the method is applicable for solders in any compositions, provided they can be formed into spheres. However, handling small solder spheres needed for fine-pitched bumping is difficult and the repeatability of the process is a significant issue.

1.2.5 Direct droplet deposition

Recently, solder bumping by transferring molten solder droplets directly onto substrate contact pads to form bumps has received a lot of attention. The typical implementation of this method involves adapting a solder jetting device that converts molten solders into micron-sized droplets. The solder droplets are then deposited onto contacts pads on wafer or PCB substrate. The deposited solder droplets may require reflowing to form into bumps. Direct droplet deposition bumping systems are generally classified into two categories based on the droplet generation methods used. A drop-on-demand system employs a solder jetting device similar to the print heads used in ink-jet printers. Solder droplets are generated on-demand as the solder print head scans and positions itself over the targeted contact pads. The droplets produced with the demand-mode system range from 25 to 125μm in diameter at rates up to 2000 droplets per second [Lau, 2000]. The small droplet sizes and moderate throughput of a demand-mode system make it more suitable for rework application and small-batch production of specialized circuits [Hayes *et al.*, 1993]. A continuous-jetting system generates a stream of uniform-sized droplets at rate up to 24,000 droplets per second. The jetting device is typically stationary while the droplets are deflected and directed electrostatically to the substrate contact pads. A typical continuous-jetting system produces droplets ranging from 75 to 800μm. The higher throughput of the continuous-jetting bumping process allows it to compete directly with other bumping methods for volume production. In contrast to the evaporation, electroplating and stencil printing methods, the direct droplet deposition method is capable of achieving very uniform

bump heights. Unlike the ball placement method, the direct droplet deposition method generates and deposits solder droplets in one step, thus eliminates the need to handle small solder spheres. In addition, the bump pattern produced using this method is data-driven and programmable. Therefore, no expansive, custom-made mask or pattern is required. However, most droplet-based bumping systems are still in the conceptual and prototyping stages. Additional developmental work is still needed to realize their potentials.

1.3 Developmental Issues of Direct Droplet Deposition Bumping

The schematic of a continuous-jetting droplet bumping system is shown in Figure 1.4. As shown in the figure, uniform droplets are produced using a continuous solder jetting device. The spray of droplets are selectively deflected in-flight and directed onto the contact pads on the target substrate. Upon reaching the contact pads, the molten droplets impact and form solder bumps on the substrate. The developmental issues associated with these functional requirements are discussed in detail below.

1.3.1 Generations of uniform-sized solder droplets

In order to achieve uniform bump heights, the solder jetting device employed needs to produce solder droplets of uniform size. A continuous-jetting process called Uniform Droplet Spray (UDS) process has been developed at MIT [Chun and Passow, 1993] to produce a spray of molten metal droplets that are uniform in size. The schematic of a UDS generator is shown in Figure 1.5. As shown in the figure, solder materials are loaded and melted inside a crucible. A laminar jet of molten solder is then produced by pressurizing the crucible with inert gas and ejecting the melt through an orifice mounted at the bottom of the crucible. The laminar jet is broken into uniform droplets by imposing sinusoidal vibrations generated by a stack of piezoelectric crystals to the melt through a vibration rod. DC voltage applied to a charging ring is used to apply static charge to these droplets as they break from the jet. The electrical repulsion of the charged droplets prevents them from merging with each other in flight. The spray process can produce droplets with a narrow size distribution (± 3% from mean size) at high rate (up to 24,000 droplets per second). The process has been widely employed to produce solder spheres

for ball placement bumping. Therefore, it can be considered as a proven droplet generation process for this application.

1.3.2 Deflection and trajectory control of the solder droplets

Since the droplet generator is stationary in the continuous-jetting droplet bumping system, the uniform droplets need to be deflected and directed in-flight to the contact pads on the target substrate. The deflection system also serves to reduce the droplet throughput of the UDS process down to a more manageable rate. In practice, droplets in the spray can be electrostatically deflected to control their trajectory [Shin, 1998, Liu *et al.*, 2000]. The deflection system consists of a set of deflection plates positioned below the droplet charging ring, as shown schematically in Figure 1.6. A constant DC voltage is applied across the defection plates so that a steady electrical field is maintained horizontally between these plates. A voltage controller is connected to the droplet charging ring to provide variable high-voltage pulses periodically. Droplets formed between voltage pulses are uncharged. Therefore, these neutral droplets are not affected by the electrical field as they travel through the deflection plates and are collected below in a heated catcher for recycling. A droplet formed during a voltage pulse is statically charged according to the magnitude of the pulse. As the charged droplet travels through the deflection plates, it is deflected horizontally by the electrical field. The extent of the deflection is proportional to the amount of charge it carries. By actively altering the charging voltage magnitudes to synchronize with the substrate motions, droplets can be selectively deposited to form the desired bump pattern.

1.3.3 Post-deposition solder bump formation

Once the droplets are generated and directed to the targeted contact pads, the subsequent forming of solder bumps are controlled by the post-impact, droplet deposition behavior. The deflected UDS droplets typically travel at 3-4m/s when they impact the contact pads. Deposition of a fully-molten solder droplet at this velocity is characterized by a rapid initial droplet deformation and radial spreading, if the post-impact solidification is slow. Generally, the initial expansion will be followed by a series of oscillations and the deposited droplet will reform into a truncated spherical bump. However, a droplet may also exhibit other deposition behavior such as splashing and bouncing which are undesirable for bump formation.

Splashing, defined by a spreading droplet that develops finger-shaped instabilities at its periphery, is a well-known droplet deposition behavior that had been studied extensively for decades [Levin and Hobb, 1971; Stow and Hadfield, 1981; Mundo *et al.*, 1995; Thoroddsen and Sakakibara, 1998; Marmanis and Thoroddsen, 1996; Aziz and Chandra, 2000; Shakeri and Chandra, 2002; Kim *et al.*, 2000]. In the extreme case of droplet splashing, these instabilities may form secondary droplets. The consequent disintegration of the deposited droplet prevents efficient delivery of the solder volume needed to form a bump. Splashing occurs when the impacting droplet has significant kinetic energy as compared with surface energy; a comparison which is typically quantified by the Weber number (We), defined as,

$$\mathrm{We} = \frac{\rho u_{ini}^2 D_{ini}}{\gamma_{mg}} \tag{1.1}$$

where ρ, u_{ini}, D_{ini}, and γ_{mg} are the solder density, the impact velocity, the initial droplet diameter, and the molten solder-gas surface tension, respectively. Experimental observations have indicated that droplet splashing generally takes place at We in the order of 100 [Mundo et al., 1995; Aziz and Chandra, 1999]. Kim *et al.* [2000] developed an analytical model based on linear perturbation theory to predict the number and temporal evolution of the fingers of a splashing droplet. Their simulations, shown in Figure 1.7, have concluded that splashing in the parameter regime of the direct droplet deposition bumping (We $\leq$ 50) is relatively mild and may not be a serious concern.

Bouncing is a phenomenon when a deposited droplet, after the initial expansion, recoil and rebound off the target surface, as shown in Figure 1.8. The bouncing behavior had been observed as early as Worthington's pioneering work on high-speed imaging of droplet depositions in 1877. However, very few analytical studies on the bouncing of molten metal droplets have been conducted. Schiaffino and Sonin [1997] noted that a mercury droplet deposited on glass rebounds completely off the surface at Weber number exceeding 1.2. Aziz and Chandra [2000] observed bouncing behavior when a molten Sn droplet was deposited on a heated stainless steel target at We $\approx$ 26. These results hence indicate that a deposited solder droplet may have a strong tendency to bounce in the parameter regime of the direct droplet

deposition bumping. In an effort to devise a strategy to control droplet bouncing, Kim [1999] investigated the effect of solidification on bouncing in the moderate Weber number regime. His model assumed that the bouncing of a molten droplet on a non-wetting surface is dependent upon the relative magnitude of its oscillation and solidification times. Representing his experimental data in a sticking-bouncing regime map, as shown in Figure 1.9, the results indicate that rapid solidification of a deposited droplet is effective in preventing bouncing. However, a quenched droplet typically forms a splat with large diameter on the target surface. Such deposit morphology is undesirable in the fine-pitched solder bumping application since it may bridge and short adjacent contact pads upon reflow, as shown in Figure 1.10. Increasing the substrate surface temperature during deposition reduces the droplet solidification rate and may allow the deposited droplet to retract back to a more desirable, spherical cap shape. However, the tendency for bouncing also increases with the slower solidification rate, according to Kim's bouncing regime map. Therefore, alternative schemes to control bouncing may need to be developed.

1.4 Thesis Motivation and Scope

The work presented in this thesis focuses on investigating the alternative factors that may be employed to control droplet bouncing in direct droplet deposition bumping. The motivation for the current investigation sterns, in part, from the observed irregularities of the droplet deposition behavior in Kim's 1999 study. Shown in Figure 1.9 as stars, Sn droplets deposited on freshly-formed Sn surface are shown to stick even when the associated solidification times indicate bouncing should occur. The phenomenon suggests that strong wetting between a deposited droplet and the target surface may retard bouncing. The droplet-surface wetting effect is relevant to solder bumping since typical contact pads on a bumping substrate are coated with adhesion layers that are wetting to the solder bump materials. However, the effect of wetting on the bouncing of molten metal droplets has not been studied systematically.

Since wetting quantifies the interaction between the droplet materials and the target surface, other factors affecting the droplet-surface interaction may also have effects on the droplet bouncing behavior. It may be noted that the typical bumping targets exhibit a range of surface roughness, from Ra = 0.06μm for the UBMs on wafers to around Ra = 0.5μm for the contact

pads on BGA substrates. Ra, or the arithmetic average of the deviations from the mean height of a surface, is a standard measure of surface roughness [ANSI, 1985]. Surface roughness is known to affect liquid-solid wetting and correlations between roughness and the liquid-solid contact angle, a quantitative measure of wetting, have been developed [Wenzel, 1936; Shuttleworth and Bailey, 1948]. However, the wetting between a deposited droplet and the target surface is a transient phenomenon. The effect of surface roughness on the transient droplet-surface wetting is still not well understood. Therefore, further investigative work is required to establish the impact of surface roughness on droplet deposition behavior.

The present study aims to examine the effects of droplet-surface wetting and target surface roughness on the droplet bouncing behavior. Physical descriptions of droplet deposition and deformation processes will be developed and the mechanisms responsible for the wetting and roughness effects on bouncing will be presented analytically and verified empirically. The investigations will focus on the isothermal droplet deposition behavior in the parameter regime relevant to a UDS-based droplet bumping process. The goal of this study is to develop a simple, quantitative criterion for process engineers to evaluate the tendency for a deposited droplet to bounce.

1.5 Thesis Organization

The current chapter has presented the background and motivation of this thesis. Chapter 2 examines the post-impact droplet deformation processes and develops an expression for the potential for droplet bouncing based on the energy conservation between the discrete deformation stages. The energy states of a deformed droplet will be presented as a function of the specific droplet-surface contact angle to incorporate the wetting effect. The effect of surface roughness on bouncing will be represented indirectly by quantifying the roughness-induced changes in transient droplet-surface wetting. The experimental work, consisting of bump morphology study and high-speed imaging of the droplet deposition, are presented in Chapter 3. The data obtained from the experimental study are processed and compared with the analytical predictions in Chapter 4 to verify the modeling concepts and the assumptions made. A threshold for the transition from droplet sticking to bouncing behavior is also identified. Summary of the conclusions made and the suggested areas of future work will be presented in Chapter 5.

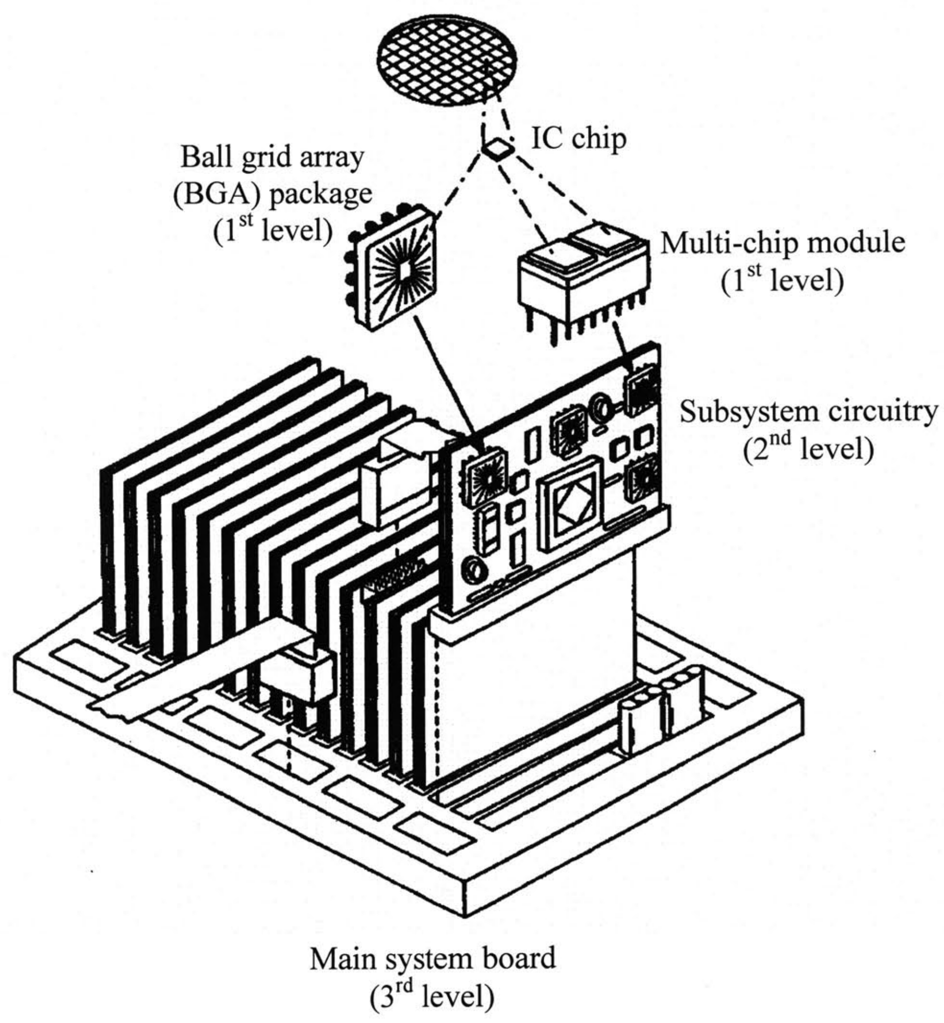

Figure 1.1. An integrated circuit (IC) based electronic system. Three levels of electronic packaging are shown. (Adapted from Lau, 2000)

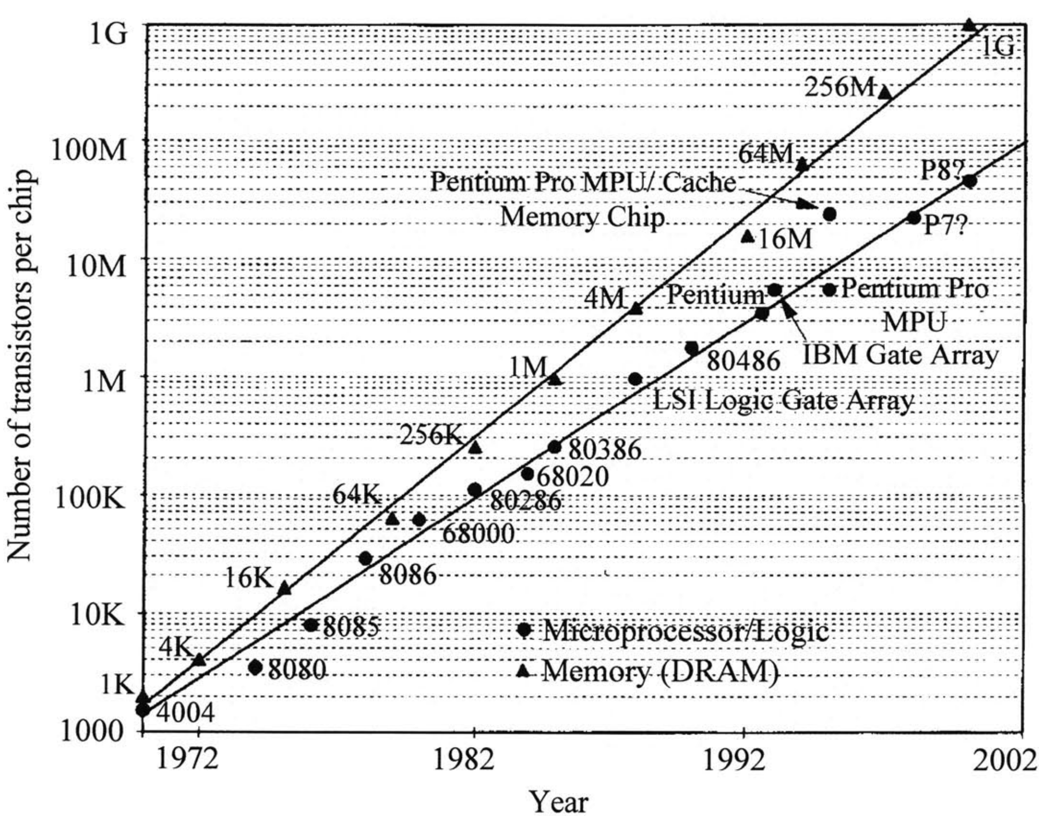

Figure 1.2. Integrated circuit technology trends (Adapted from Lee and Chen, 1998)

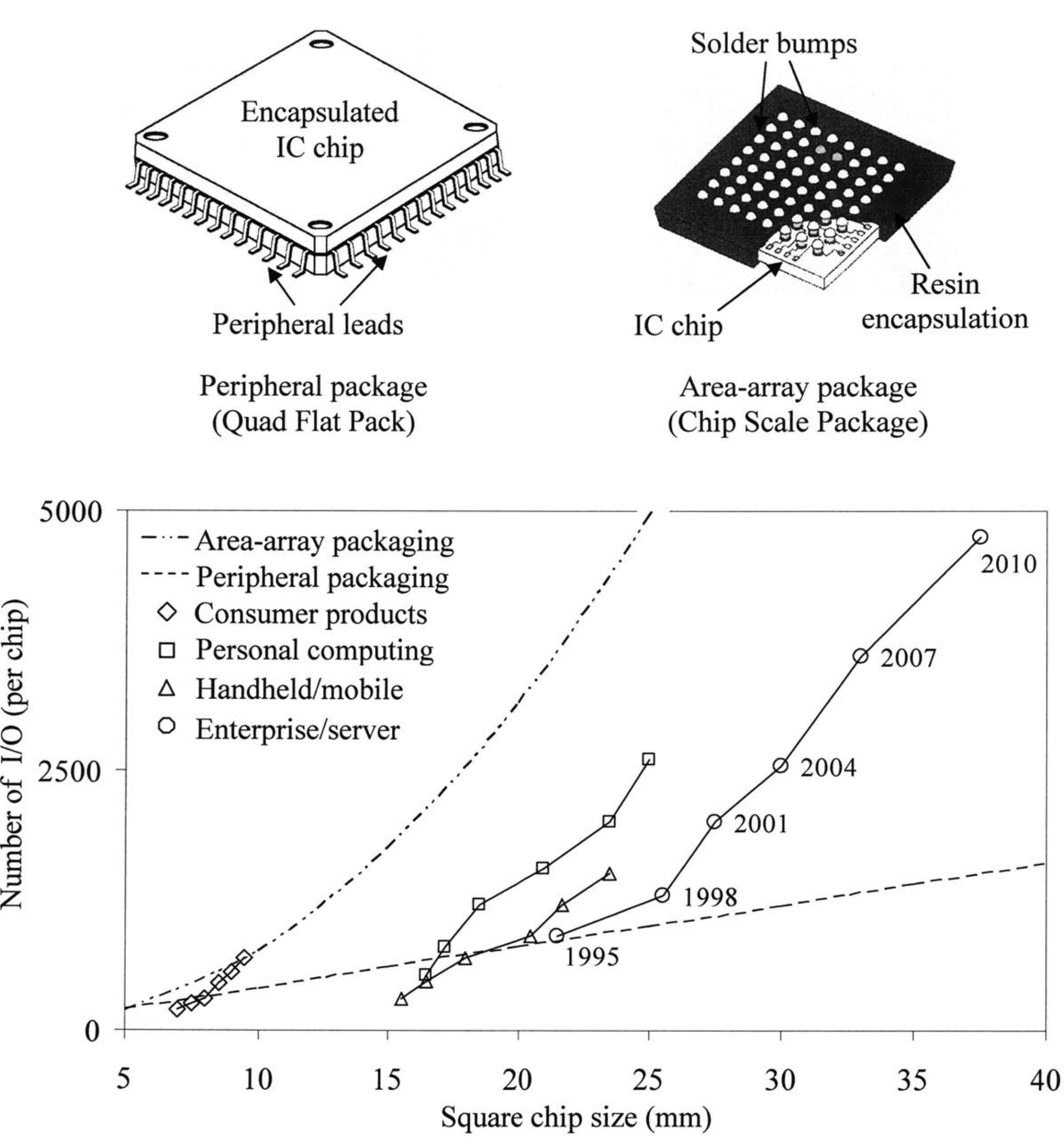

Figure 1.3. I/O capacities of the peripheral and area-array packages compared to the projected requirements. (Data source: 1994 Semiconductor Industry Association technology roadmap)

Table 1.1. Solder bumping methods summary.

Bumping Method	Advantages	Disadvantage
Evaporation	– Proven technology – Employing standard processing equipments	– High cost – Slow deposition rate – Limited material selections
Electroplating	– Proven technology – Lower cost comparing to evaporation method	– Slow deposition rate – Non-uniform bump heights
Stencil printing	– Lower cost – Material flexibility – Employing SMT manufacturing equipments – High throughput	– Stencil required – Bump pitch limitation – Non-uniform bump heights
Ball placement	– Uniform bump heights – Material flexibility – High throughput	– Sphere handling – Fixed bumping pattern
Direct droplet deposition	– Uniform bump heights – Material flexibility – Data-driven bumping pattern	– Moderate bumping rate – New technology /Require further developments

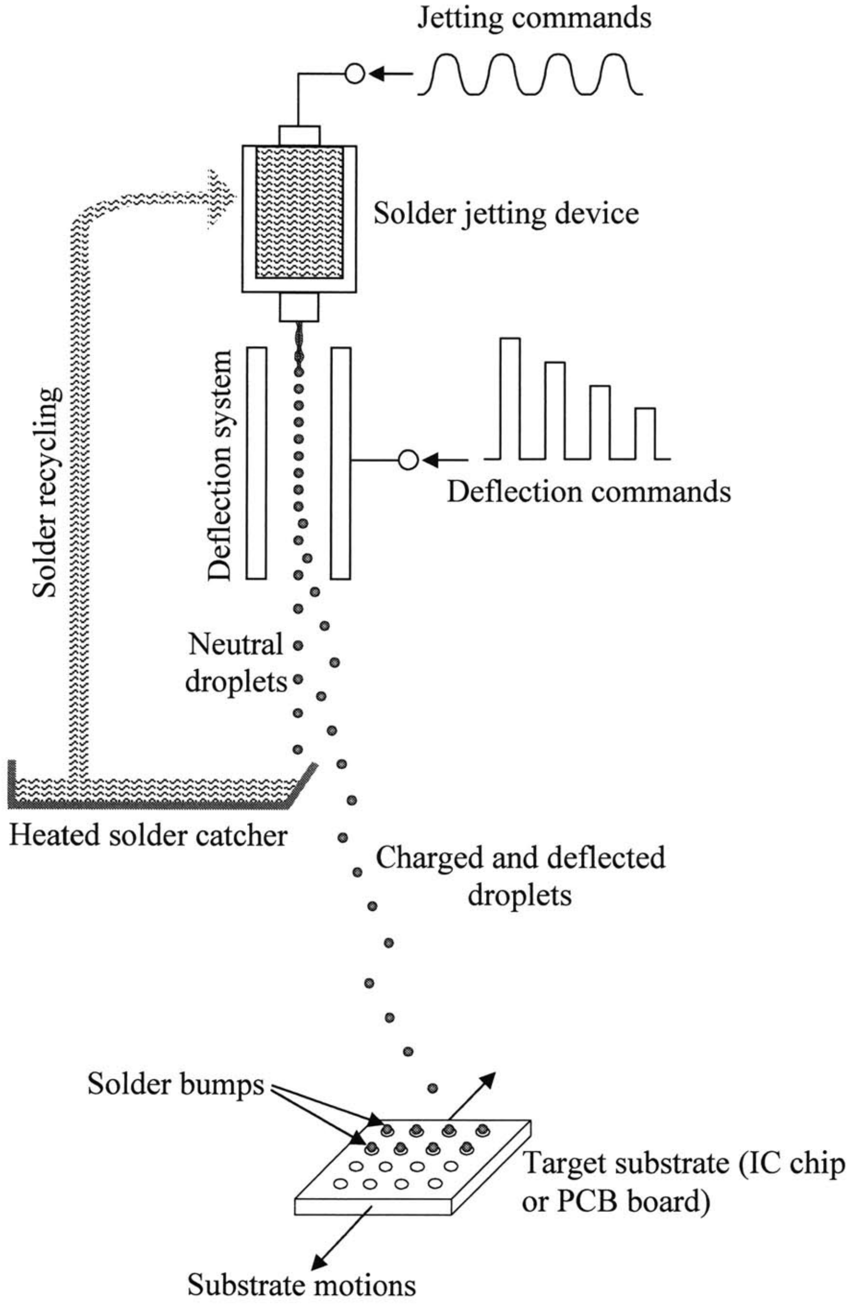

Figure 1.4. Schematic of a continuous-jetting, direct droplet deposition bumping system.

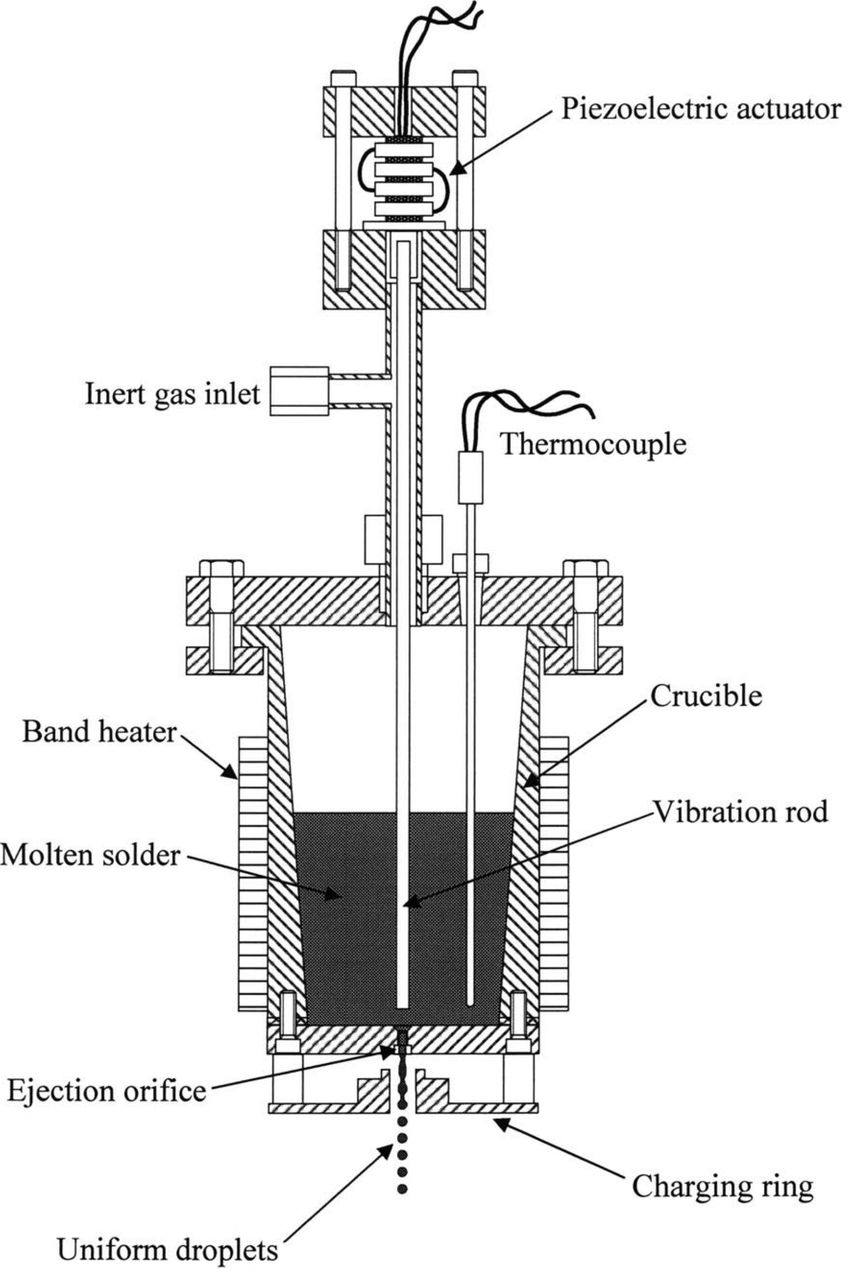

Figure 1.5. Schematic of a Uniform Droplet Spray (UDS) generator.

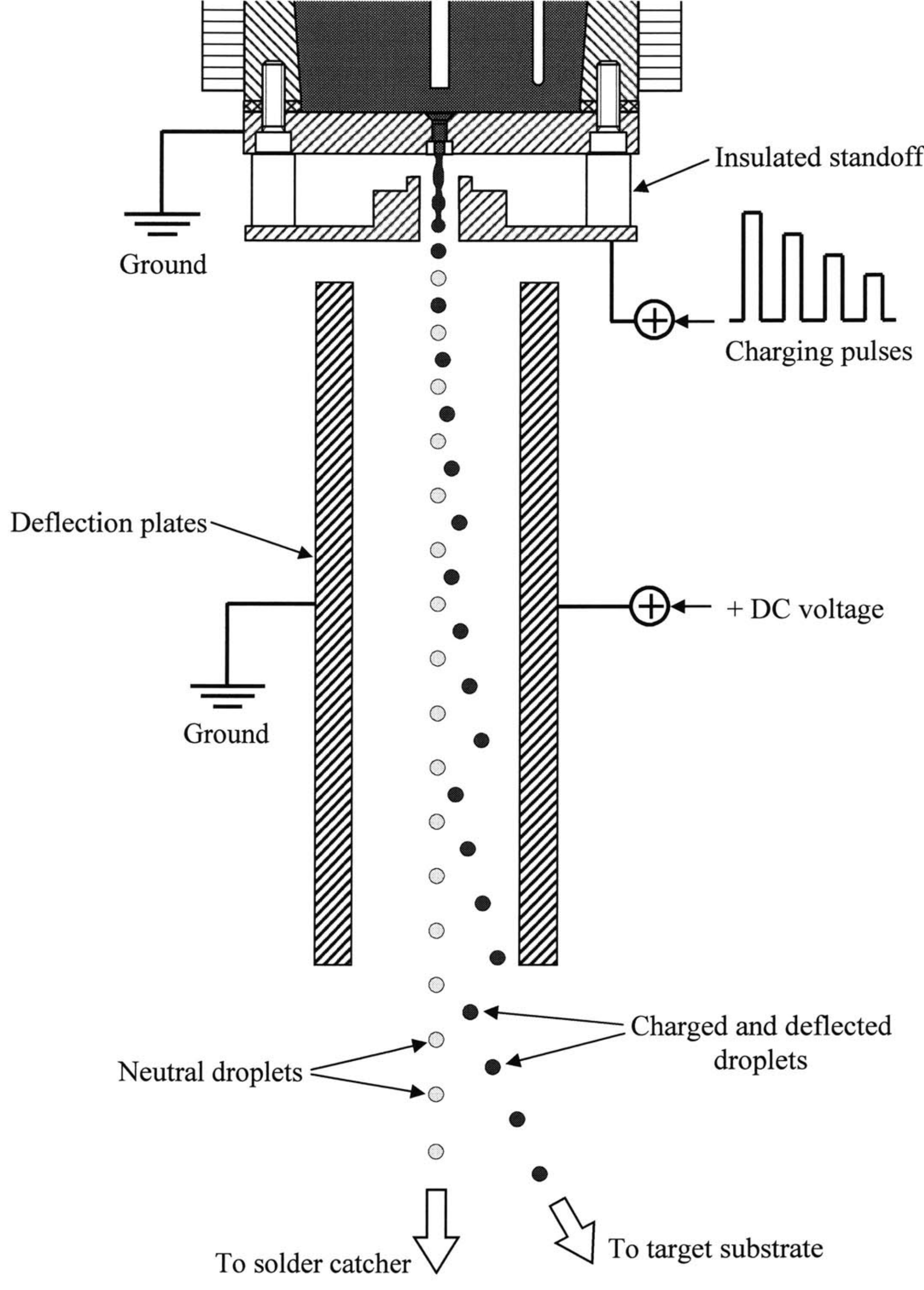

Figure 1.6. Schematic of the droplet trajectory control system.

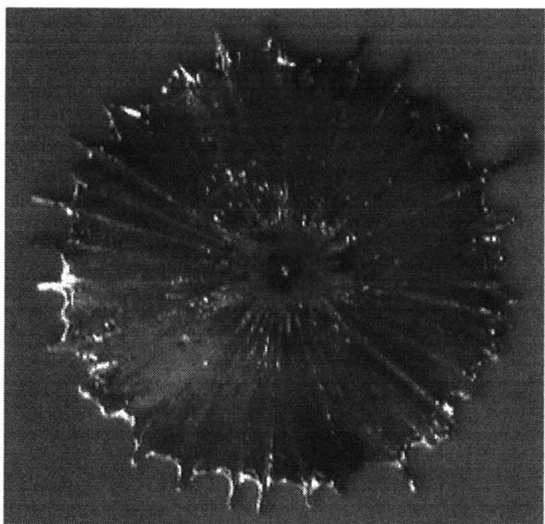

Splashed Sn droplet

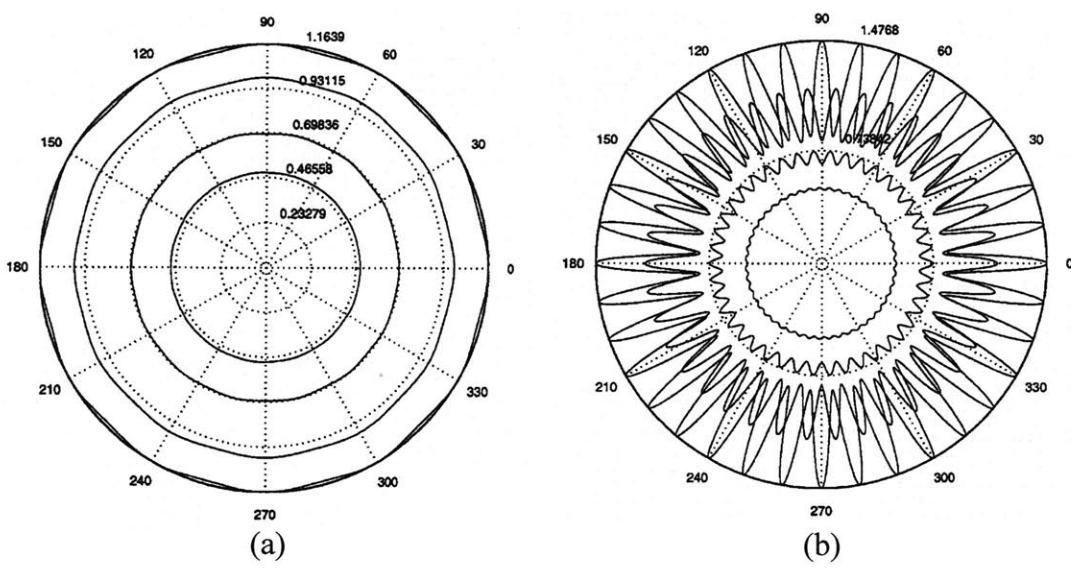

Figure 1.7. Splashing of molten droplet. (a) Simulation of the splashing shape evolution when We = 50. (b) Simulation of the splashing shape evolution when We = 500. [Kim *et al.*, 2000]

Figure 1.8. Bouncing of a Sn droplet deposited on heated Al surface.

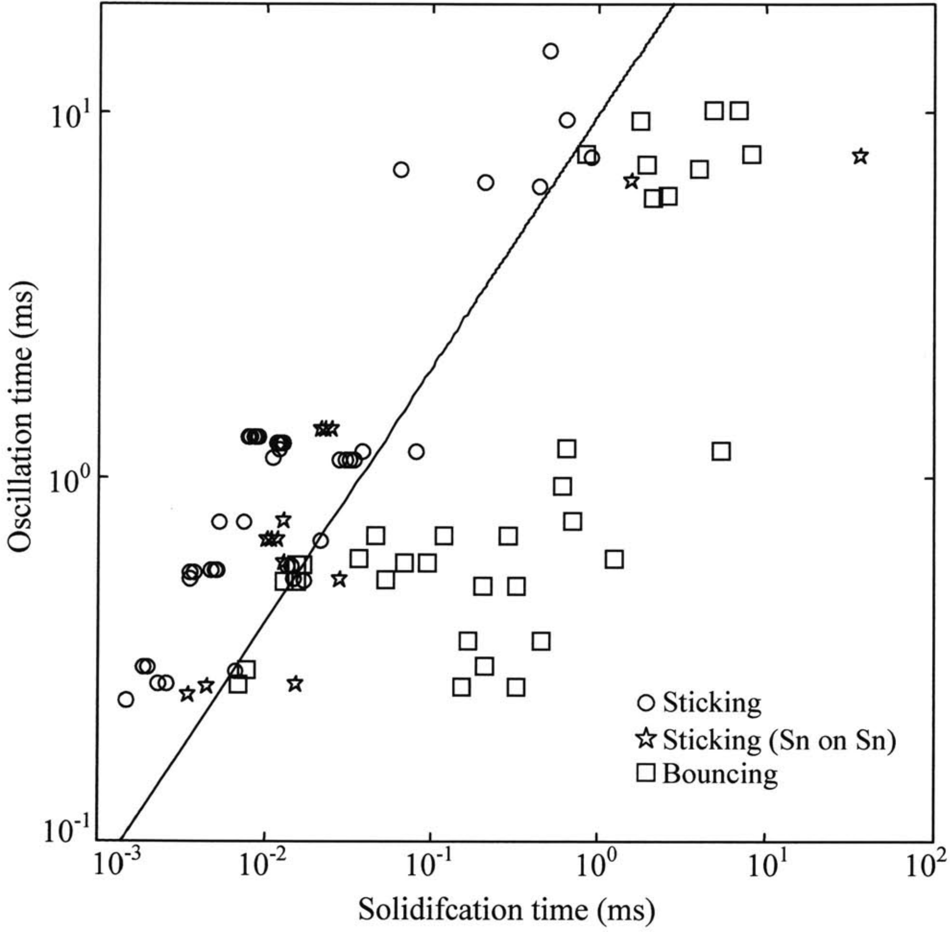

Figure 1.9. Sticking and bouncing regime map of molten Sn droplet deposition. Circles and Squares denote sticking and bouncing behaviors on non-wetting surfaces, respectively. Stars represent sticking behavior on freshly-formed Sn surface.

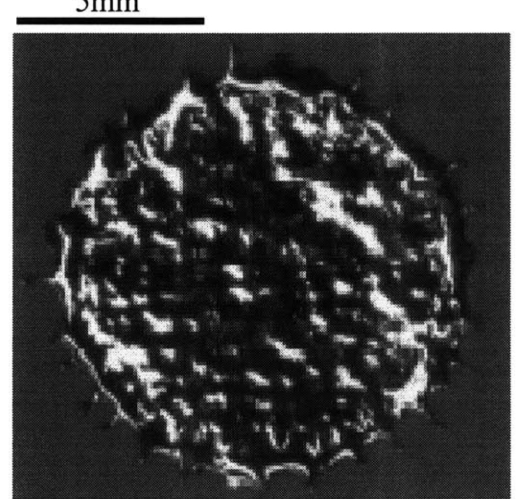

(a) Quenched Sn splat

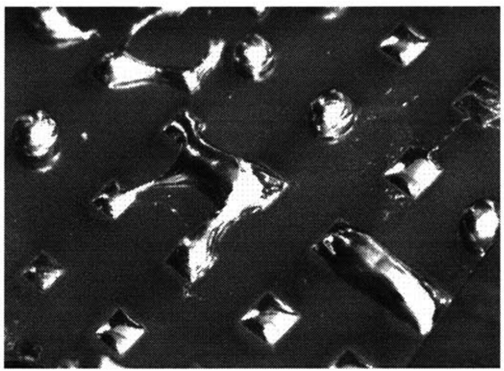

(b) Shorted contact pads after reflow

Figure 1.10. Images of (a) a quenched Sn splat (original droplet diameter: 2.6mm), and (b) contact pads shorted after the deposited droplets are reflowed.

Chapter 2. ANALYTICAL WORK

2.1 Introduction

The results of Kim's [1999] droplet deposition experiments, as introduced in Chapter 1, suggest that the interactions between droplet and the target surface during deposition may have significant influence on the occurrence of droplet bouncing. Therefore, factors that affect the droplet-surface interactions, such as the specific droplet-surface wetting property and the surface roughness, may be good candidates for exploring the potential for controlling droplet bouncing.

Kim's results specifically suggest that strong affinity, commonly described as wetting, between a droplet and the surface it is deposited on, may retard or even prevent bouncing. A survey of the published studies on the droplet bouncing phenomenon yielded similar observations. Chandra and Avedisian [1991] reported bouncing of n-heptane (C_7H_{16}) droplets when deposited on a polished stainless steel surface at or above the Leidenfrost temperature, defined as the temperature at which a vapor film is formed between the droplet and the surface. The presence of a vapor film during deposition that prevents the liquid droplet-surface wetting was assumed to cause the observed bouncing behavior. Sequences of images of water droplets deposited on paraffin wax blocks, stainless-steel plates and glass slides from the study by Mao *et al.* [1997] clearly showed the tendency for droplet bouncing to increase as the target surfaces become more hydrophobic. By studying the impact of dyed water droplets on complexed stearic acid coated glass plates and on bare Ti plates, Vignes-Adler [2002] also demonstrated that droplets exhibited a stronger tendency for bouncing when deposited on the more hydrophobic surfaces.

Surface roughness is also known to affect liquid-surface interactions. Specifically, its effects on liquid-surface wetting and interfacial thermal contact resistance are well reported [Wenzel, 1936; Nakae *et al.*, 1998; Chen and Duh, 2000; Wang and Matthys, 1996, Bernardin *et al.*, 1997]. In addition, preliminary experiments have shown significant bump morphology differences when Sn bumps were formed on the 50μm Al_2O_3 sandblasted and 0.3μm Al_2O_3 slurry polished surfaces, post-plated with 0.5μm layers of Au, as shown in Figure 2.1. However, only few

studies relevant to the effect of surface roughness on droplet bouncing are available. Shakeri and Chandra [2002] showed that a greater tendency for the deposited Sn droplets to splash when the surface roughness levels of the target steel plates were increased. Their study had also correlated variations in the splat recoiling behavior with changes in the target surface roughness. Mao *et al.* [1997] reported, without quantification, changes in the liquid-surface contact angle and the initial spreading behavior when water droplets were deposited on stainless steel and paraffin wax surfaces roughened with low-grit emery cloth.

Although the preliminary experiments and reviews of the existing studies provide evidence that droplet bouncing may be influenced by the surface wetting property and roughness characteristics, the physical mechanisms behind their effects need to be understood before their effects on bouncing can be quantified. Since droplet bouncing is observed to be preceded by vigorous retraction after the initial spreading of a deposited droplet, analyzing the effects of wetting and roughness on the dynamics of a recoiling droplet may elucidate their influences on bouncing. In principle, the motion of a deforming droplet may be obtained by solving the full Navier-Stokes equations. However, the internal flow dynamics of a deforming droplet are highly transient and analytical solutions are generally not available. Instead, numerical methods are often employed to obtain simulated results. Many researchers have analyzed the droplet deformation processes numerically [Harlow and Shannon, 1967; Tsurutani et al., 1990; Trapaga and Szekely, 1991, Fukai et al., 1993]. However, most of these modeling works focused only on the initial spreading stage and typically neglected the surface interaction effects. Therefore, their analyses and models often fail to accurately simulate the recoiling and bouncing behavior. Fukai *et al.* [1995] refined their earlier finite-element based numerical scheme to improve its ability to simulate the droplet recoiling behavior. The surface effect, i.e., the wetting condition, is considered by incorporating the measured advancing and receding contact angles in the contact line boundary conditions during the spreading and recoiling phases, respectively. The results from their simulations agree well with the observed oscillatory behavior of water droplets deposited on Pyrex glass with or without a wax coating. However, their numerical simulation did *not* account for the effect of surface roughness. Interestingly, the wetting properties of their test surfaces were altered by intentionally employing glass plates with different surface roughness levels. Therefore, their experimental results might have been unintentionally affected by the surface roughness. The surface roughness levels of the glass plates used in their

experiments, however, were not quantitatively reported. Their study hence did not link any change in the droplet deposition behavior specifically to the surface roughness variations.

The present study aims at investigating the effects of wetting and surface roughness on bouncing by analyzing their influences on the energy states of a deposited droplet. Since the motions of an oscillating droplet are inevitably controlled by the conservation of energy principle, the impacts of wetting and roughness variations on the droplet energy states during recoiling should translate into changes in the droplet bouncing behavior. Unlike the computationally intensive numerical methods, the energy approach may potentially yield a simple criterion that allows quick assessment of the potential for droplet bouncing for a given set of process parameters. Many studies have also analyzed the droplet spreading behavior based on energy conservation [Jones, 1971; Madejski, 1976; Chandra and Avedisian, 1991; Bennett and Poulikakos, 1993; Pasandideh-Fard et al., 1996]. Most of the existing studies focused on predicting the maximum spreading diameter of the deposited droplet, with or without solidification. Their results, although relevant in many industrial applications, such as irrigation and spray forming, did not offer a comprehensive description of the post-impact droplet deformation processes. Therefore, these results do not apply to droplet recoiling and the consequent bouncing behavior. The study by Mao *et al.* [1997] included a theoretical section that outlined the energy transfer processes governing the behavior of a deposited droplet from initial impact, spreading, to recoiling and ultimately bouncing. The effect of wetting was incorporated by introducing the surface energy of the droplet as a function of the static contact angle. Their droplet rebound model, however, does not consider the contact angle dynamically from spreading to recoiling. Fukai *et al.* [1995] calculated the droplet surface energy evolution during the spreading and recoiling phases, apparently based on droplet shape variations obtained from their numerical simulations. Using fixed, static contact angles to evaluate the droplet surface energies, their results nevertheless confirm the principle that the droplet surface energy at maximum spreading springboards the consequent recoiling phase. Neither of these two studies, nor other works reviewed, adequately quantifies the role of surface roughness in the energy transfer processes during droplet deposition.

The analytical work described in this chapter is aimed at addressing the issues that remain unresolved. The post-impact droplet deformation processes, from spreading and recoiling, to

either oscillation or rebound are described in detail and an analytical expression of the energy state at each discrete stage is presented. The effect of wetting is introduced by incorporating the concepts of dynamic contact angle and contact angle hysteresis into the descriptions of the energy states. The effect of surface roughness is described by its impact on the droplet to surface interactions during the deformation processes. Specifically, the wetting dynamics between an impacting droplet and an actual rough surface are modeled by the forced penetration of the deposited melt into an idealized surface defect with gas entrapment. Finally, a bouncing criterion is proposed based on the normalized surface energy difference between the maximum spreading and equilibrium states of a deposited droplet.

2.2 Isothermal, Post-impact Droplet Deformation Processes

Post-impact droplet deformation can be characterized as a continuous event where the energy of an impacting droplet transforms to distort the droplet shape and induce significant internal fluid flows. The initial potential, kinetic, and surface energies of an impinging droplet dictate whether a deposited droplet will oscillate, rebound, or splash following the initial spreading on a rigid surface [Vignes-Adler, 2002]. For a molten droplet deposited in the low to moderate Weber number, its deposition may be categorized by the dominant forces driving the initial spreading (impact or capillarity) and whether the viscous dissipation is significant [Schiaffino and Sonin, 1997]. The deposition regimes are presented graphically in Figure 2.2. The Weber number scales the driving force of the post-impact spreading. At high We, the spreading is driven by the impact-induced dynamic pressure gradient; at We below unity, the dominant driving force is the capillarity force at the contact line. The Ohnesorge number (Z) scales the force resisting the spreading and is defined by

$$Z = \frac{\mu}{\sqrt{\rho \gamma_{mg} D_{ini}}} \tag{2.1}$$

where μ is the viscosity of the deposited melt. At high Z, the resistance is dominated by viscosity. At low Z, the spreading is resisted by the stretching and deforming of the droplet surface. The impact conditions of the droplets used in the direct droplet deposition bumping

processes typically correspond to the inviscid, inertial-driven deposition regime. The droplets deposited in this parameter regime are characterized by an initial spreading and deformation phase that is dominated by the impact dynamic pressure. However, there are sufficient amounts of viscous and surface tension forces to prevent the spreading front from disintegrating and splashing onto the surface.

In contrast to the capillarity-driven spreading, where a droplet is allowed to expand to its equilibrium spreading state on its own, the impact-driven spreading forces the deposited droplet to flatten beyond its equilibrium spreading limit into a non-equilibrium disk shape. The tendency to restore surface equilibrium springboards a recoiling phase after the maximum spreading diameter is reached. Recoiling from maximum spreading leads either to droplet bouncing or, after a series of oscillation, to the equilibrium spreading state. The distinctive stages of the post-impact droplet deformation processes are shown schematically in Figure 2.3. The deformation processes analyzed in the present study are assumed to be isothermal, i.e., the effect of heat transfer and the subsequent solidification are not considered. The energy states at the discrete deformation stages are described in detail in the following sections.

2.2.1 Stage 1: Impact

A droplet on the verge of impinging a surface carries an initial energy, E_{ini}, which can be expressed as

$$E_{ini} = SE_{ini} + KE_{ini1} + PE_{ini} \tag{2.2}$$

where SE_{ini}, KE_{ini}, and PE_{ini} are the initial surface, kinetic, and potential energy, respectively. These energy states are functions of the initial conditions and properties of the droplet:

$$SE_{ini} = \pi D_{ini}^2 \gamma_{mg}, \tag{2.3}$$

$$KE_{ini} = \frac{1}{12} \pi \rho D_{ini}^3 u_{ini}^2, \tag{2.4}$$

$$PE_{ini} = \frac{1}{12}\pi\rho D_{ini}^4 g \tag{2.5}$$

where g is the acceleration due to gravity.

At the instant of impact, the potential energy is at least three orders of magnitude smaller than its surface and kinetic energy counterparts and is deemed negligible. Substituting Equation 2.3 and Equation 2.4 into Equation 2.2, the initial energy is estimated as

$$E_{ini} = \pi D_{ini}^2 \gamma_{mg} + \frac{1}{12}\pi\rho D_{ini}^3 u_{ini}^2 \tag{2.6}$$

In the high We regime, the first term of Equation 2.6, representing the surface energy portion of the impact energy, can often be neglected. However, the typical We for the deposition experiments described in the next chapter ranges from 10 to 30. In this regime, both energy terms are roughly of the same order of magnitude. Therefore, both terms are retained in the present analysis.

2.2.2 Stage 2: Maximum spreading

Immediately following the impact, the droplet deforms and the melt is driven by the dynamic pressure of impact into a radially expanding lamella, as shown in Figure 2.3(b). The spreading of the lamella is resisted by the surface tension and, in the late stage, viscosity, before eventually coming to a halt. At this moment, the shape of the deformed droplet can be approximated by a disk of diameter D_{max} and height h_m. Since the spreading ceases at this stage, the kinetic energy is negligible and the energy state at this instance is estimated only with the surface energy, SE_{max}, of the disk as

$$SE_{max} = \left[\frac{\pi}{4}D_{max}^2 + \pi D_{max} h_m\right]\gamma_{mv} + \frac{\pi}{4}D_{max}^2\left(\gamma_{ms} - \gamma_{sg}\right) \tag{2.7}$$

where γ_{ms} and γ_{sg} are the melt-solid and the solid-gas surface energies, respectively. Approximating the melt as an incompressible fluid, h_m can be written as a function of D_{ini} and D_{max} as

$$h_m = \frac{2}{3}\frac{D_{ini}^3}{D_{max}^2} \tag{2.8}$$

From Equations 2.7 and 2.8, the energy at the maximum spreading can be written as

$$SE_{max} = \left[\frac{\pi}{4}D_{\max}^2 + \frac{2\pi}{3}\frac{D_{ini}^3}{D_{max}}\right]\gamma_{mv} + \frac{\pi}{4}D_{max}^2\left(\gamma_{ms} - \gamma_{sg}\right) \tag{2.9}$$

The value of γ_{ms}, however, is not readily available. Therefore, the Young-Dupre equation is adapted to relate the difference, $\gamma_{ms} - \gamma_{sg}$, to γ_{mg} as

$$\gamma_{mg}\cos\theta = \gamma_{sg} - \gamma_{ms} \tag{2.10}$$

where θ is the intrinsic contact angle between the solid surface and the line tangent to the melt-gas interface at the meniscus contact point. Equation 2.9 can then be expressed as a function of θ as

$$SE_{max} = \left[\frac{\pi}{4}D_{max}^2\left(1-\cos\theta\right) + \frac{2\pi}{3}\frac{D_{ini}^3}{D_{max}}\right]\gamma_{mg} \tag{2.11}$$

To evaluate the droplet surface energy at maximum spreading using Equation 2.11, however, the value of θ needs to be known. The intrinsic contact angle θ, is not a unique quantity in the vicinity of maximum spreading and its value depends strongly on the dynamics of the bulk fluid motions, as shown in Figure 2.4. Further complicating the issue, multiple values of θ are possible for a stationary contact line depending on the history of the associated fluid motions, a

phenomenon known also as contact angle hysteresis. Dussan [1979] conducted a comprehensive review of research done on the contact angle dynamics. His conclusions, summarized graphically in Figure 2.5, illustrate the following points; (1) the value of θ depends on the velocity of the contact line, U_c, although the dependency at very low velocity is not well quantified, (2) the advancing dynamic contact angle, θ_{ad}, reaches an upper limit at relatively low U_c, in the order of sub-cm sec^{-1} [Ablett, 1923; Elliott and Riddiford, 1967]. It is generally believed that the receding dynamic contact angle, θ_{rd}, exhibits a similar limit. However, the experimental verifications of the receding limit are difficult to obtain due to the receding flow front instabilities [Elliott and Riddiford, 1967; Wilson, 1975], (3) the extrapolated advancing static contact angle, θ_{as}, is greater than the receding static contact angle, θ_{rs}. Ambiguities exist between the measured and the extrapolated limits of the static contact angle and the exact values of these limits are highly debatable [Elliott and Riddiford, 1967]. However, there is no question that for many material systems, an interval of uncertainty exists in the value of contact angle when the contact line is not in motion.

Therefore, in principle, the droplet surface energy at maximum spreading, as formulated in Equation 2.11, can be calculated dynamically if the states of the static contact angle are known *a priori*. However, analytical solutions of the contact angle dynamics at maximum spreading require thermodynamic modeling of the hysteresis behavior, which is outside the scope of the current study [Marmur, 1994]. Empirically resolving the contact angle dynamics is also far from straightforward. The high-speed imaging experiments, described in the next chapter, reveal that the contact angle hysteresis for a maximally spread droplet generally occurs faster than the temporal resolution of the imaging equipment. In view of these difficulties, the following compromises are made: The advancing static contact angle is approximated by the advancing dynamic contact angle, θ_{ad}. Since the spreading generally occurs over a period which is accessible by the high-speed imaging equipment, θ_{ad} can be reasonably measured from the high-speed images obtained. Nevertheless, resolving the evolution of θ_{ad} is still outside the capability of the imaging equipment. However, even though the dynamic contact angle is a function of contact line velocity, this dependence does not appear to be strong if the capillary effect is not dominant [Dussan, 1979], as is the case during the initial spreading phase. In addition, Pasandideh-Fard *et al.* have reported that the values of θ_{ad} for spreading water droplets on polished stainless steel surface reaches a maximum at velocity as low as 1m/s and does not

change with further increase in velocity. Since the spreading velocity for the deposited UDS droplets is expected to be at least of the same order of magnitude as the impact velocity ($u_{ini} \approx$ 3-4m/s), adapting constant values for θ_{ad} is justified. The receding static contact angle is approximated by the apparent static contact angle measured at the equilibrium state, θ_e. Since the contact line speed is minimal at the onset of the recoiling phase, this approximation is deemed appropriate.

Incorporating the compromised treatments of the dynamic contact angle into Equation 2.11, the droplet surface energy at maximum spreading is shown to be bounded by upper and lower limits represented as

$$SE^a_{max} = \left[\frac{\pi}{4}D^2_{max}\left(1-\cos\theta_{ad}\right)+\frac{2\pi}{3}\frac{D^3_{ini}}{D_{max}}\right]\gamma_{mg} \qquad (2.12a)$$

$$SE^r_{max} = \left[\frac{\pi}{4}D^2_{max}\left(1-\cos\theta_{e}\right)+\frac{2\pi}{3}\frac{D^3_{ini}}{D_{max}}\right]\gamma_{mg} \qquad (2.12b)$$

respectively. SE^a_{max} is the surface energy of the deposited droplet at the moment it reaches its maximum spreading diameter. SE^r_{max} is the surface energy of the deformed droplet on the verge of recoiling from its maximum spreading diameter. The dynamic surface energy state at maximum spreading is therefore reduced to two steady-state equivalents that can be determined empirically. The significance of this simplification will be evident in the later discussion.

2.2.3 Stage 3: Maximum retraction

If the maximum spreading diameter reached at the end of Stage 2 is greater than the diameter dictated by its equilibrium state, the deformed droplet will recoil to recover its surface equilibrium. The contact line may de-wet from the surface and recede while the melt at the periphery begins to propagate back toward the center of impact. As the melt begins to accumulate at the center of the retracting droplet, a bulk upward flow may result and a rising peak may develop at the center. The maximum extent of the droplet retraction without bouncing

is shown in Figure 2.3(c), where the rising peak has expanded to resemble a column momentarily at rest on the surface. If the column shape is assumed to be axisymmetric about z axis, its energy states may be represented as

$$PE_r = \pi\rho g \int_0^{h_r} yx^2 dz \tag{2.13}$$

$$SE_r = 2\pi\gamma_{mg}\left[\int_0^{h_r} x\sqrt{1+\left(\frac{dx}{dy}\right)^2}\,dz - \frac{1}{8}D_r^2\cos\theta_{rd}\right] \tag{2.14}$$

where h_r is the height of the column, D_r is the minimum base diameter and $x = f(z)$ defines the geometry of the column shape. The column shape, however, is not well defined, hence the generalized expression for $x = f(z)$ is not available. Therefore, the analytical solutions for the energy states at maximum retraction are not considered accessible for the scope of the current study.

2.2.4 Stage 4*: Bouncing (complete and partial)

In the case of very aggressive retraction, the aforementioned column grows rapidly as the contact line recedes quickly to reduce its base diameter. If the base diameter is reduced to zero, the detached column will retract into a droplet to minimize its free surface and complete bouncing will occur, as shown in Figure 2.3(d). For the case of complete bouncing, the droplet's energy states are represented as

$$SE_{cb} = \pi D_{ini}^2 \gamma_{mg} \tag{2.15}$$

$$KE_{cb} = \frac{1}{12}\pi\rho D_{ini}^3 \int_0^{h_{cb}} u_{cb}^2 dz \tag{2.16}$$

$$PE_{cb} = \frac{1}{6}\pi\rho D_{ini}^{3} g h_{cb} \tag{2.17}$$

where $u_{cb}=f(z)$ is the velocity of the rebounded droplet and h_{cb} is the rebound height.

If the surface of the column becomes unstable, surface waves may begin to develop on its surface. If the surface waves grow faster than the droplet base retraction, then a portion of the column may consequently be pinched off to form a sub-droplet, as shown in Figure 2.3(e). The phenomenon is termed partial bouncing. Assuming that the remaining portion of a partially bounced droplet forms an hemi-spherical, sessile drop on the surface defined by its θ_e, the instantaneous energy states of a partially rebound droplet are shown as

$$SE_{pb} = \pi\left\{D_{pb}^{2} + \frac{1}{4}D_{p}^{2}\left[\frac{2}{(1+\cos\theta_{e})} - \cos\theta_{e}\right]\right\}\gamma_{mg} \tag{2.18}$$

$$KE_{pb} = \frac{1}{12}\pi\rho D_{pb}^{3}\int_{0}^{h_{pb}} u_{pb}^{2}\,dz \tag{2.19}$$

$$PE_{pb} = \frac{1}{6}\pi\rho D_{pb}^{3} g h_{pb} \tag{2.20}$$

where D_{pb} is the sub-droplet diameter and D_p is the diameter of the remaining sessile drop on the surface. $u_{pb}=f(z)$ and h_{pb} are the sub-droplet velocity and height, respectively.

The equations above show that determining the dynamic energy states of either a completely or partially rebounded droplet requires information on its transient behavior at and after the instant when bouncing occurs. The analytical solution for the energy state of a partially bounced droplet requires the determination of the value of D_{pb}. The growth of the surface waves responsible for the formation of the secondary droplet is dictated by Rayleigh's instability triggered by random

disturbances. As a result, the location of the pinch-off point, and hence the size of the secondary droplet, cannot be predicted without first quantifying the disturbances.

The simplest approach for estimating the energy states at the bouncing stage may be by assuming a limiting configuration for the complete bouncing case. In this configuration, the rebounded droplet recovers its initial spherical shape and is on the verge of disengaging from the surface, as shown in the dashed outline in Figure 2.3(d). The energy states of the droplet are hence reduced to the surface energy and a simplified form of the kinetic energy, expressed as

$$KE_{cb} = \frac{1}{12}\pi\rho D_{ini}^3 u_b^2 \qquad (2.21)$$

where u_b is the instantaneous rebound velocity at $h_{cb} = 0$. The rebound energy state, E_b, can then be formulated as

$$E_b = \pi D_{ini}^2 \gamma_{mg} + \frac{1}{12}\pi\rho D_{ini}^3 u_b^2 \qquad (2.22)$$

However, it may be noted that even though the velocity of the rebound droplet no longer needs to be considered as a variable function of z, the value of u_b is still a transient value not readily determined by analytical means. Therefore, without further simplification, only an empirical solution for E_b may be possible.

2.2.5 Stage 4: Equilibrium

If the retraction immediately following the maximum spreading does not lead to bouncing, then the recoiling droplet dissipates its kinetic energy through a series of oscillations until its equilibrium sessile state is restored. Since the deposited droplet is not in motion when it reaches its equilibrium shape, the energy state at this stage can be describe by its surface energy alone, provided that its potential energy is negligible. Assuming the shape of the sessile drop as a spherical cap, as shown in Figure 2.3(f), its geometry may be described fully if θ_e and the

equilibrium spreading diameter, D_{equ}, are given. The surface energy of the deposited droplet at equilibrium, SE_{equ}, is determined by

$$SE_{equ} = \left[\frac{\pi D_{equ}^2}{2(1+\cos\theta_e)} \right] \gamma_{mg} + \left(\frac{\pi}{4} D_{equ}^2 \right) (\gamma_{ms} - \gamma_{sg}) \tag{2.23}$$

By applying the Young-Dupre equation, as in Equation 2.10, Equation 2.23 can be rewritten as

$$SE_{equ} = \frac{\pi}{4} D_{equ}^2 \left[\frac{2}{(1+\cos\theta_e)} - \cos\theta_e \right] \gamma_{mg} \tag{2.24}$$

If the droplet melt is consider as incompressible, the equilibrium spreading diameter can be determined by the principle of mass conservation as

$$D_{equ} = D_{ini} \left[\frac{4\sin\theta_e}{\tan^2(\theta_e/2)(2+\cos\theta_e)} \right]^{\frac{1}{3}} \tag{2.25}$$

Combining Equation 2.24 and Equation 2.25, the equilibrium surface energy can be shown as

$$SE_{equ} = \frac{\pi}{4} D_{ini}^2 \left[\frac{4\sin\theta_e}{\tan^2(\theta_e/2)(2+\cos\theta_e)} \right]^{\frac{2}{3}} \left[\frac{2}{(1+\cos\theta_e)} - \cos\theta_e \right] \gamma_{mg} \tag{2.26}$$

As shown in Equation 2.26, SE_{equ} can be determined if the initial droplet properties and the specific melt-surface wetting condition are quantified. Therefore, the energy of a deposited droplet of a given size in equilibrium is a unique function of its apparent static contact angle which can be readily measured. The implication is that the equilibrium energy state is well defined and independent of the deposition dynamics; it is not subject to the analytical complications associated with the energies at the retraction and bouncing stages.

2.3 Potential for Droplet Bouncing

From the energy conservation point of view, it is clear that the energy at each stage of the deformation processes directly affects the droplet's behavior in the subsequent stage. In principle, droplet bouncing can be predicted if the energy components of a deforming droplet can be accounted for exactly from impact to the end of recoiling when bouncing occurs. The energy balances for the isothermal droplet deposition can be approximated as follows,

$$SE_{ini} + KE_{ini} = SE_{max} + Diss_{1-2} \tag{2.27}$$

$$SE_{max} = PE_r + SE_r + Diss_{2-3} \tag{2.28}$$

$$PE_r + SE_r = E_b + Diss_{3-4^*} \tag{2.29}$$

Note that all three equations contain dissipation terms. The full energy descriptions of the droplet deformation processes will hence require quantifications of these dissipations. The most accessible form of dissipation involves viscous friction within the droplet's internal flow fields. However, only the viscous dissipation during the initial spreading stage, $Diss_{1-2}$, has received significant modeling attention [Chandra and Avedisian, 1991; Pasandideh-Fard *et al.*, 1996; Mao *et al.*, 1997], partly because the boundary conditions of the hydrodynamics problem are more easily defined. $Diss_{3-4^*}$ represents the dissipation work done when a droplet transforms from a column back to a sphere and the motions involved are relatively minor. Therefore, $Diss_{3-4^*}$ may be justifiably neglected. The internal flows during the retraction stage are not well defined. Therefore, analytical expression for $Diss_{2-3}$ is typically unavailable. Nevertheless, Mao *et al.* [1997] have obtained an empirical correlation for $Diss_{2-3}$, as part of their efforts to develop a droplet rebound model. Since their experimental results were based on the depositions of water/sucrose solution droplets, in contrast to the molten metal droplets used in this study, their empirical correlation requires verification before it can be included in the current analysis. Their solution was apparently based on digital processing of high-speed images of droplets at the

maximum retraction stages. As described earlier, the droplet shape at maximum retraction is highly unstable and not well-defined. Since the aim of the current study is to develop a simple analytical criterion, it is undesirable for its development to require characterizations of such highly transient phenomenon.

In response to these practical limitations, a simple estimation of the specific potential for droplet bouncing is proposed instead. Since recoiling, and hence bouncing, is driven by the affinity of a maximally spread droplet to minimize its surface energy and restore its equilibrium state, the difference between the surface energies of these two states can be regarded as the specific potential for droplet bouncing. The energy difference is formulated as

$$\Delta E = SE^{r}_{max} - SE_{equ} \tag{2.30}$$

Since ΔE represents the excess energy available to drive the droplet retraction, the droplet surface energy just prior to the onset of retraction, $SE^{r}_{\max}$, is used to represent the energy state at maximum spreading. By substituting Equations 2.12b and Equation 2.26 into Equation 2.30 and rearranging the terms, the specific potential for droplet bouncing can be shown to correlate with the configuration shown in Figure 2.6 as

$$\Delta E = \left(A^{max}_{mg} - A^{equ}_{mg} - \Delta A_{ms}\cos\theta_{e}\right)\gamma_{mg} \tag{2.31}$$

where A^{max}_{mg} and A^{equ}_{mg} are the melt-gas surface areas of a droplet at maximum spreading and equilibrium, respectively. ΔA_{ms} is the differential melt-surface contact area. The area terms are shown as

$$A^{max}_{mg} = \frac{\pi}{4}D^{2}_{max} + \frac{2\pi}{3}\frac{D^{3}_{ini}}{D_{max}} \tag{2.32}$$

$$A_{mg}^{equ} = \frac{\pi D_{equ}^2}{2(1+\cos\theta_e)} \tag{2.33}$$

$$\Delta A_{ms} = \frac{\pi}{4}\left(D_{max}^2 - D_{equ}^2\right) \tag{2.34}$$

It may be noted that the diameter of a droplet at equilibrium, D_{equ}, is a unique function of θ_e, according to Equation 2.25. Therefore, A_{mg}^{equ} is defined by the initial droplet size and droplet-surface wetting condition and is not subject to variations in the deposition conditions. A_{mg}^{max} and ΔA_{ms} are both functions of D_{max}, a dynamic property representing the droplet impact conditions. Increases in D_{max} will increase A_{mg}^{max} and hence the energy difference. However, a larger D_{max} will also increase ΔA_{ms}, which counteracts the simultaneous increase of A_{mg}^{max}, as shown in Equation 2.31. When a droplet is deposited on a wetting surface ($\theta_e < 90°$), the resultant melt-solid interfacial energy, as a function of γ_{ms}, is always lower than the energy of the solid-gas surface that it replaced. Therefore, the energy at the interface between a deposited droplet and target surface will have a stabilizing role by lowering the overall energy. Alternatively, the retraction following the maximum spreading may be viewed as being driven by the surface energy of the stretched droplet surface, represented by A_{mg}^{max}, and resisted by the interfacial tension as a function of ΔA_{ms}. Quantifying A_{mg}^{max} and ΔA_{ms} requires determination of D_{max}. Attempts to analytically evaluate D_{max} are described in the following section.

2.3.1 Estimation of the maximum spreading diameter

As shown in the previous section, the specific potential for droplet bouncing is a function of the maximum spreading diameter, D_{max}. D_{max} is a transient, extremal parameter available for measurement only during the initial, spreading-to-recoiling transition period of a deposited droplet. For a sub-millimeter droplet deposited with high initial velocity, as in the case of solder bumping, determining D_{max} can be difficult. However, it is possible to estimate the value of D_{max}

by solving the energy balance during the initial spreading phase, as shown in Equation 2.27. Since the initial spreading ceases when the droplet reaches it maximum spreading diameter, the upper bound of the surface energy at maximum spreading, SE^a_{max}, is substituted to represent SE_{max}. The energy balance then is

$$SE_{ini} + KE_{ini} = SE^a_{max} + Diss_{1-2} \tag{2.35}$$

To solve Equation 2.35, the viscous dissipation during the initial spreading stage, $Diss_{1-2}$, needs to be specified. However, no comprehensive model exists to describe the internal fluid flow and the associated viscous dissipation during droplet deformation and spreading. Nevertheless, many researchers have attempted to develop different approximate schemes. A review of the published approaches is available in Appendix A. The present study adapts the solution based on the work of Pasandideh-Fard *et al.* [1996]. Details of their model development are included in the Appendix. In summary, the work done in deforming the droplet against viscosity is formulated as

$$Diss_{1-2} = \int_0^{t_s}\int_v \varphi dv dt \approx \varphi v t_c \tag{2.36}$$

where φ and t_c are the viscous dissipation function and spreading time, respectively. $v = \pi/4\,\delta D^2_{max}$ is the volume of the viscous fluid, where δ is the internal flow boundary layer thickness. Assuming that the dissipation function is proportional to $\mu(u_{ini}/\delta)^2$ and approximating the flow within an impacting droplet as axisymmetric stagnation point flow, the dissipated energy may be estimated as

$$Diss_{1-2} \approx \frac{\pi}{3}\gamma_{mg} D^2_{max} \frac{\mathrm{We}}{\sqrt{\mathrm{Re}}} \tag{2.37}$$

where Re is the Reynolds number evaluated with the initial droplet impact parameters and shown as

$$\mathrm{Re} = \frac{\rho u_{ini} D_{ini}}{\mu} \tag{2.38}$$

By combining Equations 2.3, 2.4, 2.12(a), and 2.37, the energy balance shown in Equation 2.35 can be re-arranged to give D_{max} as

$$D_{max} = D_{ini} \sqrt{\frac{\mathrm{We}+12}{3(1-\cos\theta_{ad})+4\left(\mathrm{We}/\sqrt{\mathrm{Re}}\right)}} \tag{2.39}$$

As shown in Equation 2.39, the maximum spreading diameter of a deposited droplet of a given size is a function of the initial impact conditions and the advancing dynamic contact angle. The terms $(1-\cos\theta_{ad})$ and $\left(\mathrm{We}/\sqrt{\mathrm{Re}}\right)$ scale the effects of capillarity force and impact dynamic pressure in the initial spreading stage. At high We, the impact pressure will dominate and the capillarity effect may be neglected during initial spreading. If this assumption is true, then D_{max} may be predicted with sufficient accuracy without the knowledge of θ_{ad}. At very high We (We » 12), Equation 2.39 reduces to:

$$D_{max} = 0.5 D_{ini}\,\mathrm{Re}^{0.25} \tag{2.40}$$

A 300μm pure Sn droplet generated using the UDS process will typically be deposited with Re ≈ 3000-5000. The simplified form shown in Equation 2.40 hence yields an estimated D_{max} around 1100-1200μm. Judging from the diameters of the solder bumps formed in the preliminary study, the result overestimated the empirical data by at least 40%. Consequently, capillarity effect may not be neglected in the present deposition regime and the complete form shown in Equation 2.39 needs to be used. As noted in the earlier section, θ_{ad} needs to be determined empirically using

the high-speed images of droplet depositions. Therefore, the accuracy of Equation 2.39 will be verified in Chapter 4 where the experimental data are presented.

2.4 Effect of Roughness on Droplet-Surface Wetting During Deposition

The previous sections have correlated the surface energy difference between a droplet at maximum spreading and equilibrium to the potential for droplet bouncing. It may be noted that a decrease in θ_e, signifying an improvement in the droplet-surface wetting condition, will reduce the specific potential for droplet bouncing as shown in Equation 2.31. Therefore, the analyses have essentially laid the groundwork describing the effect of wetting on bouncing. The impact of surface roughness on liquid-to-surface wetting has been well documented [Wenzel, 1936; Cassie and Baxter, 1944; Johnson and Dettre, 1969; Drelich *et al*., 1996; Nakae *et al*., 1998]. In the context of capillarity-driven spreading, surface roughness is generally credited to enhance wetting by lowering the apparent liquid-surface contact angle [Wenzel, 1936]. However, for the highly transient wetting event such as the impingements of water droplets on glass and steel surfaces, increases in the surface roughness have been correlated to increases in the flow front instabilities during spreading and more aggressive retractions [Vignes-Adler, 2002]. These phenomena are consistent with the droplet deposition behavior exhibited on poor wetting surfaces, as shown in the high-speed images of water droplets deposited on paraffin wax block [Mao *et al*., 1997]. Consequently, these observations appear to indicate that increases in surface roughness deteriorate the transient wetting conditions. The contradictions of the observed effects of surface roughness on the droplet-surface wetting conditions are perplexing. However, the rate of spreading appears to be the key to understand the mechanisms behind these contrasting effects of surface roughness on wetting. For a gently deposited droplet spreading under the influence of the capillarity forces, the droplet liquids are allowed sufficient time to fill in and displace the gases trapped within the surface defects on the rough surface. Therefore, the presents of these defects increase the effective surface area under the droplets, and hence improve the overall droplet-surface wetting condition. For a droplet deposited with sufficient velocity that the impact forces are driving its initial spreading, the initial spreading rate may be several orders of magnitude higher compared with the capillarity-driven spreading rate. The consequent higher flow front velocity may prevent the droplet melts from entering and displacing the gases in the

surface defects. Therefore, the transient interfaces between the deforming droplet and the target surface may be populated with voids formed by the gas pockets trapped within the surface defects. The void formations observed at the bump-substrate interface from the preliminary study, as shown in Figure 2.7, appear to support this hypothesis. Gas entrapment at the droplet-surface interface effectively creates a composite interface, as shown schematically in Figure 2.8. The composite interface is a physical equivalence of incomplete wetting, and hence drastically increases the net melt-surface interfacial energy. To quantify the incomplete wetting due to the composite interface, a non-dimensional, effective area fraction, $F_a = A_{eff} / A_{real}$, is introduced. A_{real} is the total surface area of a rough surface including the contribution from the surface defects, while A_{eff} is the actual area that comes into contact with the droplet melts. The concept of F_a is interpreted schematically in Figure 2.9. The value of F_a varies from 0 to 1, corresponding to non-wetting to complete wetting, respectively. The effect of F_a on the melt-surface interfacial energy can be represented as

$$\gamma_{ms}^{*} = F_a \gamma_{ms} + (1 - F_a)\gamma_{sg} \tag{2.41}$$

where γ_{ms}^{*} is the effective melt-solid surface tension. For a liquid droplet deposited on a wetting, metallic surface where $\gamma_{sg} > \gamma_{ms}$, a less than unity value of F_a means that γ_{ms}^{*} will become greater than γ_{ms}, the intrinsic melt-solid surface tension. The effect of the resultant increase in the melt-surface interfacial energy may be quantified by calculating the adjusted contact angle, θ_e^{*}. By substituting γ_{ms}^{*} into the Young-Dupre equation, θ_e^{*} may be shown as

$$\theta_e^{*} = \cos^{-1}\left(\frac{\gamma_{sg} - \gamma_{ms}^{*}}{\gamma_{mg}}\right) \tag{2.42}$$

As shown in Equation 2.43, the adjusted contact angle will increase as γ_{ms}^{*} becomes greater than γ_{ms}, hence signify a overall deterioration of the droplet-surface wetting condition.

The direct effect of F_a on θ_e^* can be specified by combining Equation 2.41 and Equation 2.42 as

$$\theta_e^* = \cos^{-1}(F_a \cos\theta_e) \qquad (2.43)$$

For completely wetted surface (F_a = 1), Equation 2.43 shows that θ_e^* is reduced to the apparent static contact angle, θ_e. As the melt-surface wetting deteriorates and F_a is reduced toward zero, the value of θ_e^* increases toward 180° which specifies a non-wetting condition.

Therefore, the extent of the incomplete wetting caused by a composite melt-surface interface may be quantified using F_a. Consequently, the effect of surface roughness on the transient wetting condition can be specified if the value of F_a can be correlated to the particular target surface roughness level.

As shown in Figure 2.8, the actual contact area between the deposited melt and the rough surface, A_{eff}, is controlled by the extent of melt penetration into the surface defects. The amount of melt penetration is controlled by the local force balance at each surface defect. The force balance may be written as

$$P_a + P_c^n = P_g \qquad (2.44)$$

where P_a , P_c^n, and P_g are the applied pressure, the normal component of the capillarity pressure, and the pressure from the compression of the trapped gas. As shown in Figure 2.10, the melt is driven into a defect by the applied pressure and the capillarity forces, while being counteracted by the compression of the trapped gas. The extent of melt penetration on a rough surface, and hence the associated A_{eff} and F_a, can be determined if Equation 2.44 can be solved analytically. However, the capillarity forces and the gas compression are functions of the specific defect geometry. The surface defects on a rough surface are random in their shape and size. Therefore, solving Equation 2.44 requires a generalized model of an actual rough surface. A surface model generalizing the actual surface defects as conical notch indentations is presented in the following section.

2.4.1 Modeling of melt-surface interaction

The effective area fraction, F_a, may be proposed as a metric to evaluate the effect of surface roughness on wetting. However, empirical evaluation of F_a requires information on the transient melt-surface interface of a deposited droplet in real-time; an enormously difficult experimental challenge. Analytical estimation of F_a requires modeling of the melt penetration into surface defects with gas entrapment, as described in the previous section. The primary analytical challenge is that the geometries of the actual surface defects are random in nature. Addressing this issue, a generalized surface model, similar in concept to one proposed by Prasher [2001] in his study of the thermal contact resistance of thermal interface materials used in microelectronic packaging, is adapted to characterize the actual surfaces.

A typical surface defect on an actual rough surface is represented by a conical notch indentation. The overall rough surface is then characterized as an ideally flat surface populated by a densely packed array of identical notch indents, as shown in Figure 2.11. As shown in the figure, the notch geometry is fully described by r_c and h, the notch radius and depth, respectively. The actual rough surface is simulated using the generalized surface model by defining the geometry of the conical notches and empirically determined roughness parameters.

To select the proper roughness parameters to represent the notch geometry, the interfaces between deposited droplet and surfaces with different roughness characteristics were examined. Samples of Sn and Pb-37wt% Sn solder bumps formed on Au-plated, roughened surfaces were prepared and imaged using a scanning electron microscope (JEOL JXA-733). The bump-surface interfaces are shown in Figure 2.12. The images show that the gas pockets generally lay between adjacent peaks on the surfaces. In addition, the type of defects that entraps gas tends to be associated with surface waviness; that is, the medium-frequency irregularities on the surface on which the surface roughness is superimposed [Morton, 2002]. The definition of the surface waviness is shown schematically in Figure 2.13. Based on these observations, it is concluded that h and r_c may be represented by the 10-point heights, Rz, and the average period of the surface waviness, x_p, of the surface, respectively. Rz is a standard roughness parameter [ANSI, 1985) defined as the average height difference between the five highest peaks and five lowest valleys within the sampling length. No standardized definition for the wavelength is available.

Therefore, x_p is typically represented by the low wavelength applied to filter the data from surface profiling.

Once the generalized surface model is defined, the interactions between it and the deposited melt may be analyzed. When a droplet is deposited over the surface, it is driven into the conical notch by the applied pressure and the capillary pressure, as shown in Figure 2.14. The applied pressure is approximated by the stagnation pressure of an impacting droplet, which is represented as

$$P_a = \frac{1}{2}\rho u_{ini}^2 \tag{2.45}$$

where ρ and u_{ini} are the droplet melt density and the droplet impact velocity, respectively. The normal component of the capillary pressure is shown as

$$P_c = \frac{2\gamma_{mg}\sin(\theta_e + \Phi)}{r_c - y_p \cot\Phi} \tag{2.46}$$

where r_c, Φ , and y_p are the notch radius, notch angle, and melt penetration depth, respectively.

The forces are balanced by the back pressures from compressing the trapped gas in the notch. Assuming that (1) ideal gas law applied for the trapped gases, and (2) the gas volume contained within the spherical dome under the melt is negligible compared with the gas trapped in the conical volume of a notch, the back pressure is represented as

$$P_g = P_0 \frac{r_c^3}{(r_c - y_p \cot\Phi)^3} \tag{2.47}$$

where P_0 is the atmospheric pressure. The force balance shown in Equation 2.44 can hence be represented as

$$\frac{1}{2}\rho u_{ini}^2 + \frac{2\gamma_{mg}\sin(\theta_e + \Phi)}{r_c - y_p \cot\Phi} = P_0 \frac{r_c^3}{(r_c - y_p \cot\Phi)^3} \tag{2.48}$$

The melt penetration depth can be determined by solving equation above, a 3rd order polynomial in y_p. The equation indicates that y_p is a strong function of the notch angle, Φ. For pure Sn with $\gamma_{mg} \approx 0.54\,N/m$, depositing on a wetting surface (θ_e = 30°), the melt penetration is reduced as the notch angle decreases, as shown in Figure 2.15. The implication of this correlation is that if greater surface roughness is characterized by larger indentations with shallow notch angles, then an increase in the surface roughness may cause a reduction in melt penetration.

From the schematics shown in Figure 2.8, it is clear that the farther the melt is able to penetrate the notches, the greater the A_{eff}, and hence the effective area fraction, F_a, will become. Representing the extent of melt penetration with the penetration ratio, $\eta = y_p/h$, the relationship between the melt penetration and F_a is shown as

$$F_a = 1 - (1-\eta)^2 \tag{2.49}$$

As shown in Figure 2.16, the value of F_a exhibits a parabolic growth as the penetration ratio increases toward unity, representing complete fillings of the surface defects.

In summary, the effect of surface roughness on transient wetting is described by the incomplete penetration of the deposited melt into the surface defects due to the gas entrapment. To analytically determine the extent of the incomplete penetration, a generalized surface model representing the actual rough surface as an ideally flat surface populated with conical notches has been proposed. By solving the force balance that controls the melt penetration on this simulated surface, the actual melt penetration, and hence the extent of the roughness-induced incomplete wetting, may be estimated.

2.5 Bouncing Criterion

The goal of the analytical work is to introduce a simple criterion measuring the tendency for a deposited droplet to bounce during direct droplet deposition bumping based on the given process parameters. As shown in the previous section, exact prediction of droplet bouncing requires complete resolution of the energy conservation during the post-impact droplet deformation processes, a difficult analytical task and outside the scope of the current investigation. Alternatively, the specific potential for droplet bouncing may be represented by the surface energy difference between the maximum spreading and equilibrium sessile states of a deposited droplet. Therefore, the non-dimensional form of this energy difference may be adapted as a bouncing criterion. Normalizing the specific potential for droplet bouncing by the initial droplet energy, $E_{ini} = SE_{ini} + KE_{ini}$, the bouncing criterion can be shown as

$$\Delta E^* = \frac{1}{E_{ini}}\left[\left(A_{mg}^{max}\gamma_{mg} - A_{mg}^{equ}\gamma_{mg}\right) - \Delta A_{ms}\gamma_{mg}\cos\theta_e\right] \tag{2.50}$$

Incorporating definitions of A_{mg}^{max}, A_{mg}^{equ}, and ΔA_{ms} and rearranging, Equation 2.50 can be rewritten as

$$\Delta E^* = \frac{\pi D_{ini}^2}{4E_{ini}}\left[\left(\zeta_{max}^2 + \frac{8}{3\zeta_{max}}\right) - \frac{2\zeta_{equ}^2}{1+\cos\theta_e} - \left(\zeta_{max}^2 - \zeta_{equ}^2\right)\cos\theta_e\right]\gamma_{mg} \tag{2.51}$$

where ζ_{max} and ζ_{equ} are the maximum and equilibrium spreading ratio, represented by

$$\zeta_{max} = \left[\frac{We_{ini} + 12}{3(1-\cos\theta_{ad}) + 4\left(We_{ini}/\sqrt{Re_{ini}}\right)}\right]^{\frac{1}{2}} \tag{2.52}$$

$$\zeta_{equ} = \left[\frac{4\sin\theta_e}{\tan^2(\theta_e/2)(2+\cos\theta_e)}\right]^{\frac{1}{3}} \tag{2.53}$$

respectively. Note that the bouncing criterion, as defined by Equation 2.51 and supplemented by Equations 2.52 and 2.53, is a function of θ_e and θ_{ad} for deposition of a droplet with known size and impact conditions. Pasandideh-Fard *et al.* have shown experimentally by depositing droplets of surfactant solutions (sodium dodecyl sulphate in water) on polished stainless steel surfaces that the maximum values of θ_{ad} are independent to the specific droplet-surface wetting conditions. Therefore, θ_{ad}, and hence ζ_{max}, can be considered as independent of θ_e, which represents the specific surface wetting condition.

2.5.1 Effect of droplet-surface wetting

Figure 2.17 shows the effects of variations in the droplet-surface wetting condition on the bouncing criterion. The plot simulates the depositions of 300μm Pb-37wt% Sn solder droplets generated using the UDS process on surfaces with variable wetting conditions, ranging from wetting (θ_e = 10°) to non-wetting ($\theta_e \geq 90°$). The figure shows that as the surface wetting condition deteriorates from wetting to non-wetting, the bouncing criterion, indicated by the solid line, increases by nearly an order of magnitude. This large increase may be interpreted as a significant growth in the potential for droplet bouncing. The dynamics of the bouncing criterion variation may be elucidated by the interaction of factors driving and resisting droplet recoiling as described below.

As shown in Equation 2.50, droplet recoiling is driven by the melt-gas surface energy difference, represented by $A_{mg}^{max}\gamma_{mg} - A_{mg}^{equ}\gamma_{mg}$, and resisted by the differential melt-solid surface energy, represented by $\Delta A_{ms}\gamma_{mg}\cos\theta_e$. The dash-dotted and dashed lines in Figure 2.17 illustrate the magnitudes of these two terms, respectively. For brevity, they are referred to as $A_{mg}^{max} - A_{mg}^{equ}$ and ΔA_{ms}, respectively, in the following discussion and in the figure. As shown in the figure, $A_{mg}^{max} - A_{mg}^{equ}$ and ΔA_{ms} are comparable in magnitude up to approximately θ_e = 20°. The effect of ΔA_{ms} peaks near θ_e = 30° and decrease as the contact angle increases. In contrast, the magnitude of $A_{mg}^{max} - A_{mg}^{equ}$ continues to increase until a plateau is reach near θ_e = 70°. It may also be noted that ΔA_{ms} becomes less than zero after θ_e = 90°, indicating that the melt-solid

interfacial energy no longer retards, but promotes bouncing on non-wetting surfaces. Since the difference between $A_{mg}^{max} - A_{mg}^{equ}$ and ΔA_{ms} represents the potential for droplet bouncing, the effect of wetting on bouncing can be described as follows. When the surface is wetting to the deposited droplet, the equilibrium spreading diameter of the droplet is similar to its maximum spreading diameter. The difference between the melt-gas droplet surface areas at maximum spreading and equilibrium are consequently minor. Therefore, there is little potential for a deposited droplet to recoil. As the droplet-surface wetting deteriorates, the diameter and surface area differences become greater. The consequence increase in the bouncing potential is balanced by the energetically favorable melt-solid interface scaled by the differential melt-surface contact area. In the poor wetting case, the tendency for a deformed droplet to restore its surface equilibrium overwhelms the stabilizing effect of the melt-surface interaction. The resultant high bouncing criterion hence predicts aggressive recoiling that leads to bouncing.

2.5.2 Effect of surface roughness

The analysis from the previous section has demonstrated that the incomplete wetting induced by gas entrapment may be represented by the associated effective area fraction, F_a. By employing the proposed generalized surface model, F_a for a droplet deposited on a surface of given roughness characteristics may be determined analytically. Using Equation 2.43, the adjusted contact angle, θ_e^*, maybe then be calculated. In practice, θ_e^* may replace θ_e in Equation 2.51 and Equation 2.53 to represent the effect of surface roughness on the bouncing criterion as

$$\Delta E^* = \frac{\pi D_{ini}^2}{4E_{ini}}\left[\left(\zeta_{max}^2 + \frac{8}{3\zeta_{max}}\right) - \frac{2\zeta_{equ}^2}{1+\cos\theta_e^*} - \left(\zeta_{max}^2 - \zeta_{equ}^2\right)\cos\theta_e^*\right]\gamma_{mg} \tag{2.54}$$

$$\zeta_{equ} = \left[\frac{4\sin\theta_e^*}{\tan^2\left(\theta_e^*/2\right)\left(2+\cos\theta_e^*\right)}\right]^{\frac{1}{3}} \tag{2.55}$$

The effect of F_a on the bouncing criterion is shown in Figure 2.18. As shown in the figure, the values of the bouncing criterion for droplets deposited on a wetting surface increases as F_a

decreases, indicating increases in the potential for bouncing. However, the effect of F_a diminishes as wetting deteriorates. A transition is marked at θ_e = 90°, where F_a has no effect on the bouncing criterion. Beyond θ_e = 90°, increases in F_a begin to reduce the bouncing criterion. The physical explanations of the observed dynamics are as follows. The low values of θ_e defining the wetting regime signify that the melt-solid surface tension, γ_{ms}, is generally much smaller than the solid-gas surface tension, γ_{sg}, for wetting surfaces. Therefore, the melt-solid interface created by a deposited droplet is energetically favorable and acts to counter the tendency for the droplet to recoil and bounce. Consequently, the associated bouncing potential is low. If voids are introduced at the interface, the interfacial energy is increased. The magnitude of the increase is quantified as

$$\gamma_{ms}^{*} - \gamma_{ms} = (1 - F_a)(\gamma_{sg} - \gamma_{ms}) \tag{2.56}$$

As shown in Equation 2.56, a less-than-unity F_a results in a net increase in the interfacial energy, In addition, the increase will be magnified for a given value of F_a if the difference between γ_{sg} and γ_{ms} is large. Therefore, the effect of F_a is shown to be more predominant in the wetting regime. As the intrinsic surface wetting property deteriorates, $\gamma_{sg} - \gamma_{ms}$ becomes smaller and the effect of F_a diminishes. At θ_e = 90° where $\gamma_{sg} = \gamma_{ms}$, changes in F_a produce no change in the interfacial energy as dictated by Equation 2.56. In the non-wetting regime where θ_e > 90°, γ_{ms} becomes larger than γ_{sg} and it becomes energetically favorable for the deposited droplet to disassociate itself from the surface. Therefore, a decrease in F_a will act to lower the bouncing potential.

2.6 Summary

The post-impact droplet deformation processes and the associated energy states were described in detail. The transient behaviors of the apparent contact angle and their effects on the droplet surface energy in the vicinity of maximum spreading were addressed. The difference between the droplet surface energies at maximum spreading and equilibrium states was proposed as a

simple criterion for evaluating the tendency of droplet bouncing. Since the differential surface energy is a function of the wetting condition, the effect of wetting on droplet bouncing was hence implied. The effects of surface roughness on the transient melt-surface interactions were also analyzed. The roughness-induced gas entrapment and the resultant composite melt-surface interface were predicted as the mechanisms responsible for the effect of surface roughness on transient wetting during droplet deposition. The melt-surface interaction on a rough surface was analyzed by simulating the actual surface with a notched surface model and by approximating the effective contact area fraction. The roughness-induced incomplete wetting was then quantified by evaluating the adjusted contact angle using the analytically determined effective area fraction. Finally, a bouncing criterion was developed based on the differential surface energy concept. The criterion, incorporating the effects of wetting and surface roughness, indicates that enhancing the droplet-surface wetting and reducing the surface roughness may retard the occurrence of droplet bouncing in the direct droplet deposition bumping applications.

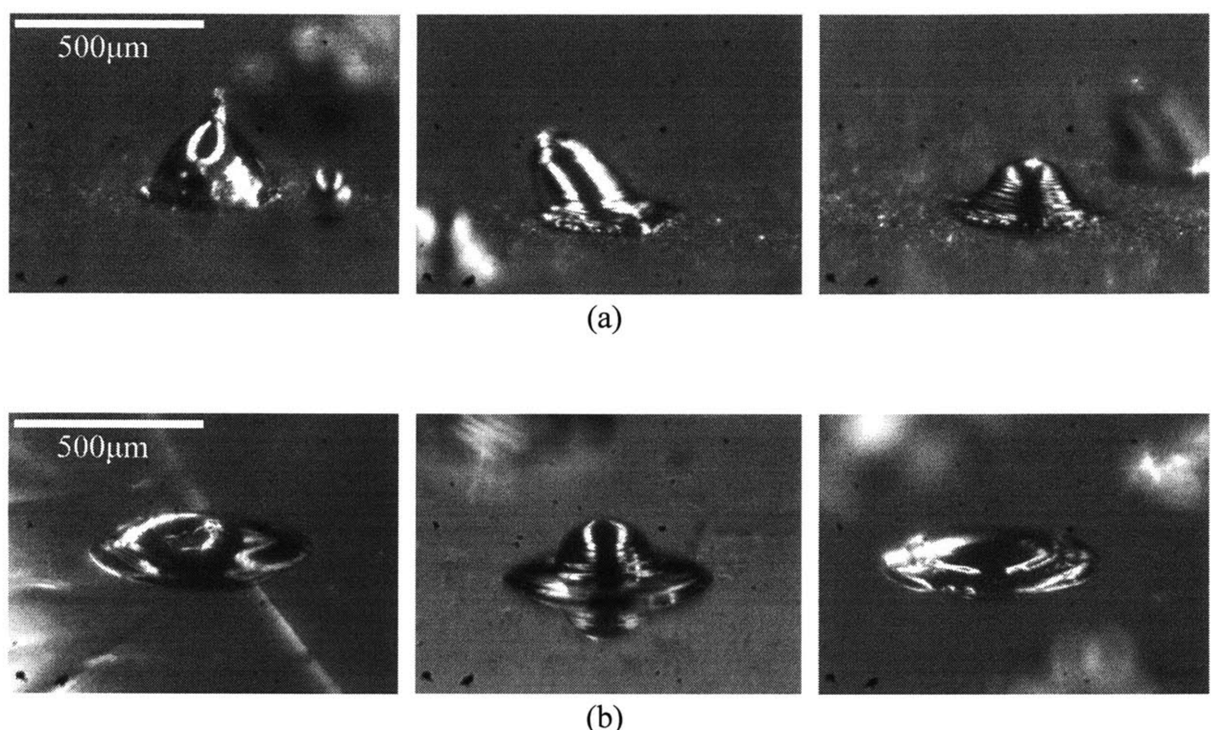

Figure 2.1. Sn bumps formed on surfaces with different roughness. (a) 50μm Al_2O_3 sandblasted Cu plate, post-plated with 0.5μm-thick layer of Au, Ra ≈ 1.0μm. (b) 0.3μm Al_2O_3 slurry polished Cu plate, post-plated with 0.5μm-thick layer of Au, Ra ≈ 0.15μm.

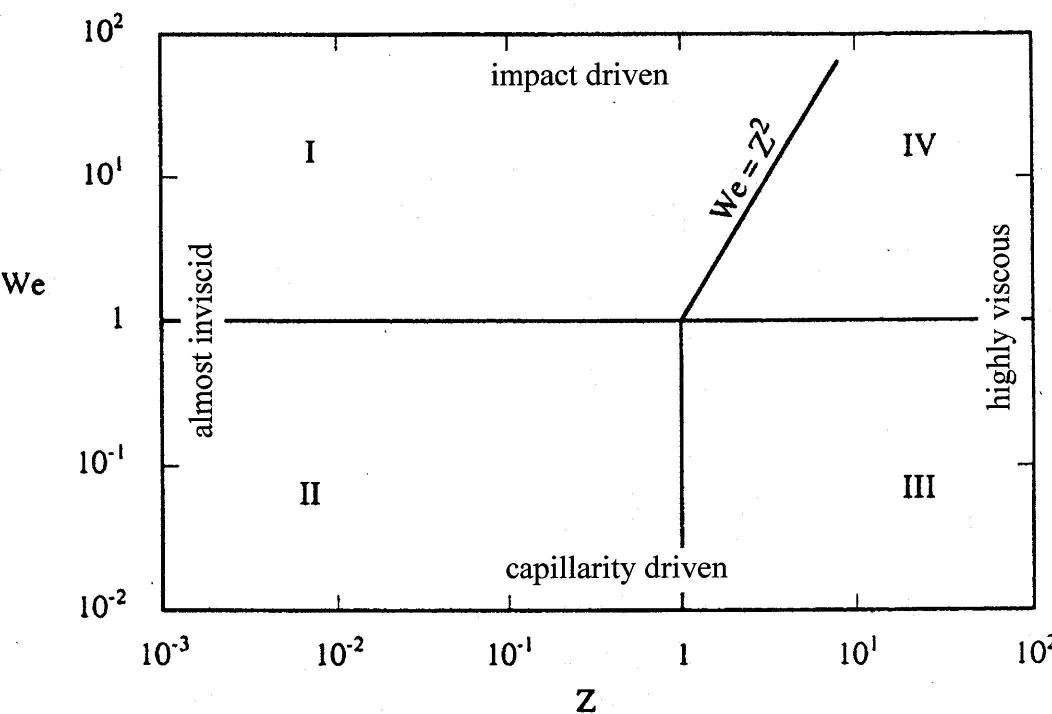

Figure 2.2. The four regions of low to moderate We droplet deposition. Map adopted from Schiaffino and Sonin [1997]. We and Z are the Weber number and Ohnesorge number, respectively.

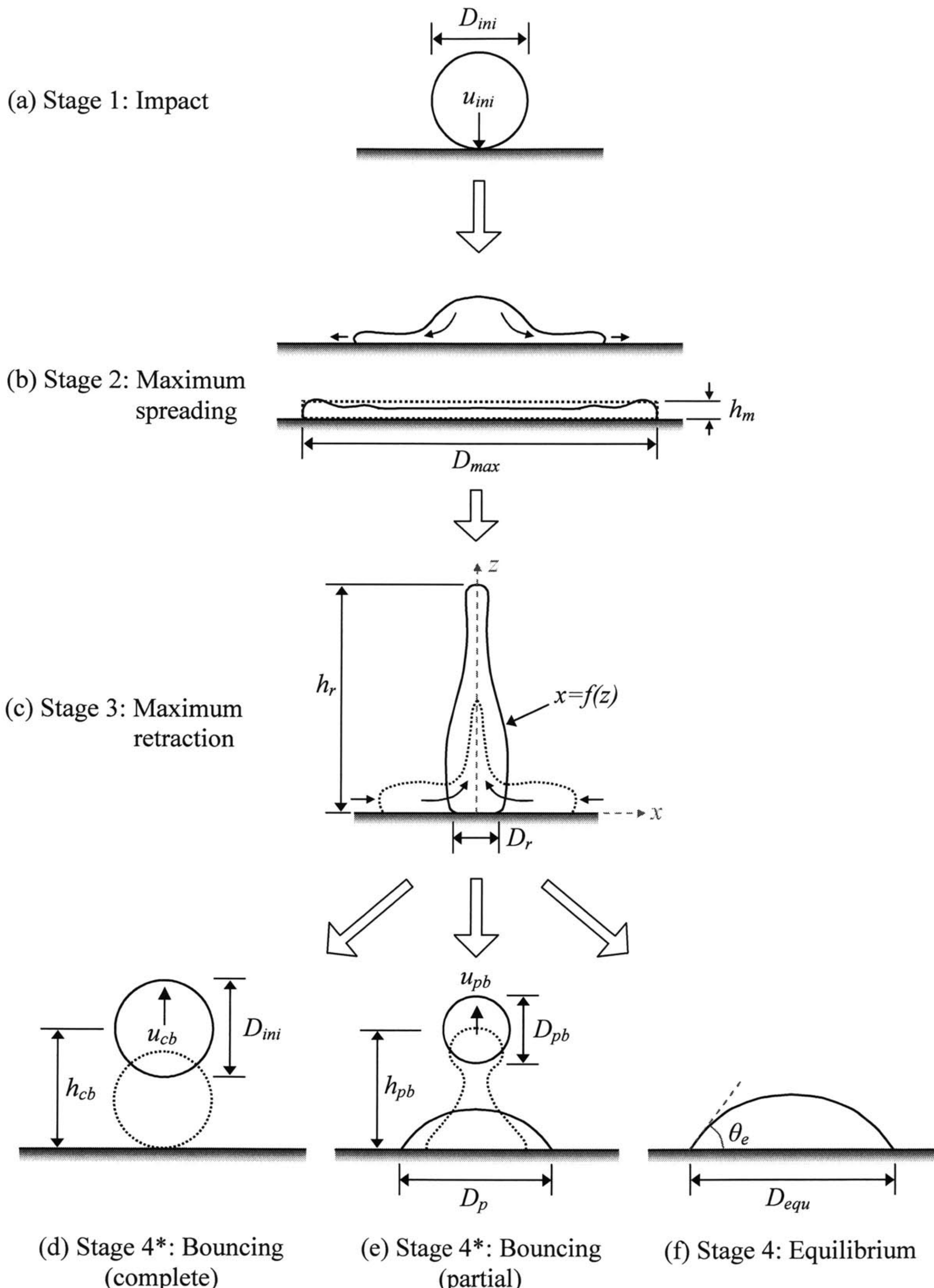

Figure 2.3. Post-impact droplet deformation processes.

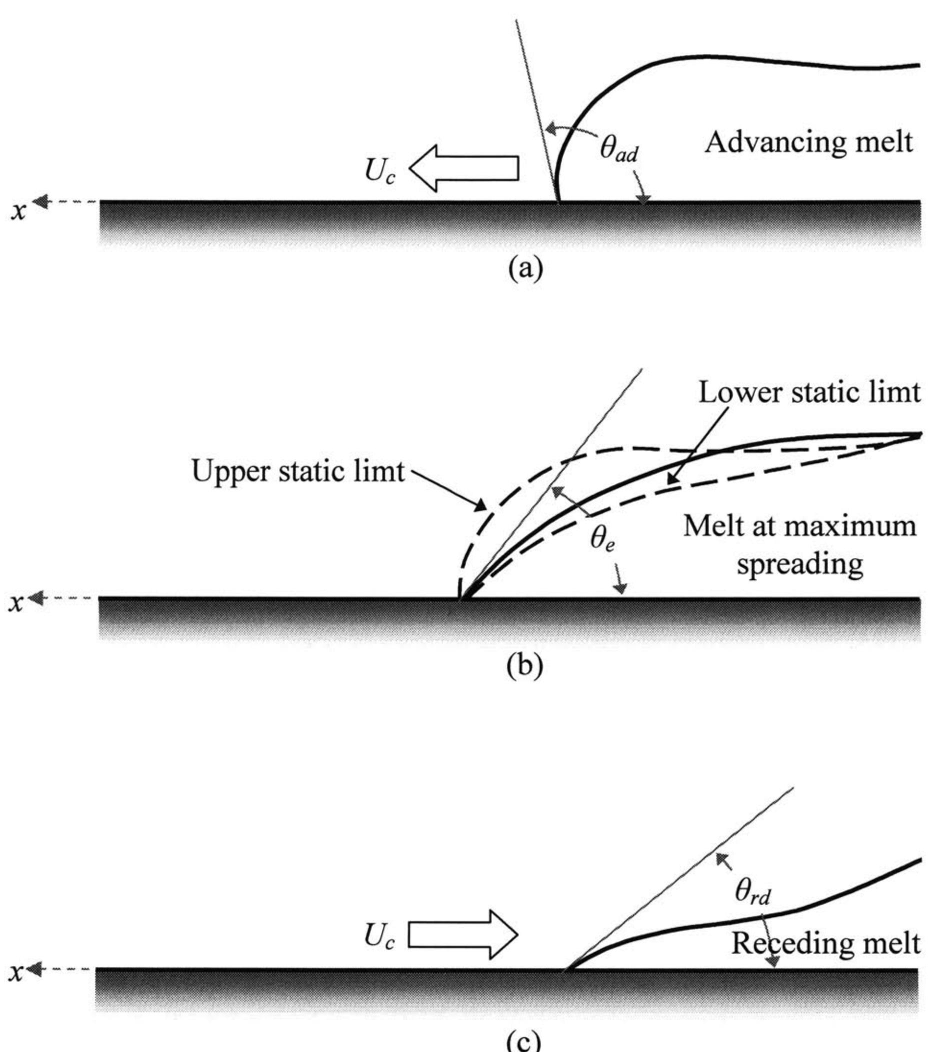

Figure 2.4. Dynamics of the apparent melt-surface contact angle: (a) Advancing contact line, i.e., $U_c > 0$, and the advancing dynamic contact angle, θ_{ad}. (b) Hyseresis at the stationary contact line and the static contact angle, θ_e. (c) Receding contact line, i.e., $U_c < 0$, and the receding dynamic contact angle, θ_{rd}.

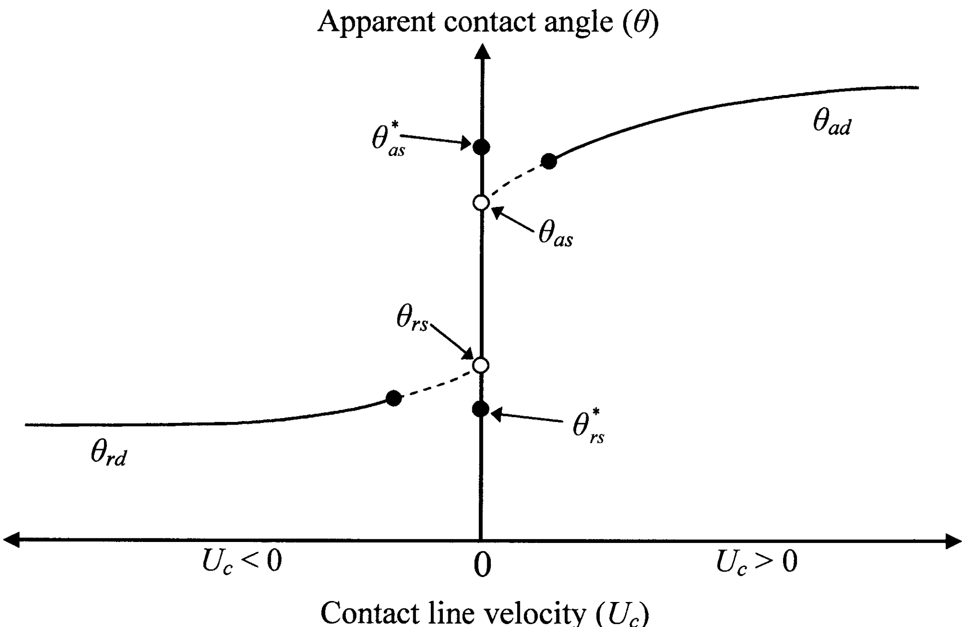

Figure 2.5. Apparent contact angle as a function of the contact line velocity [Dussan, 1979]. θ_{as} and θ_{rs} are the extrapolated advancing and receding limits of the static contact angle hysteresis, assuming the advancing or receding contact line is slowing to a stop. θ^*_{as} and θ^*_{rs} are the limits measured when an initially stationary contact line begins to move.

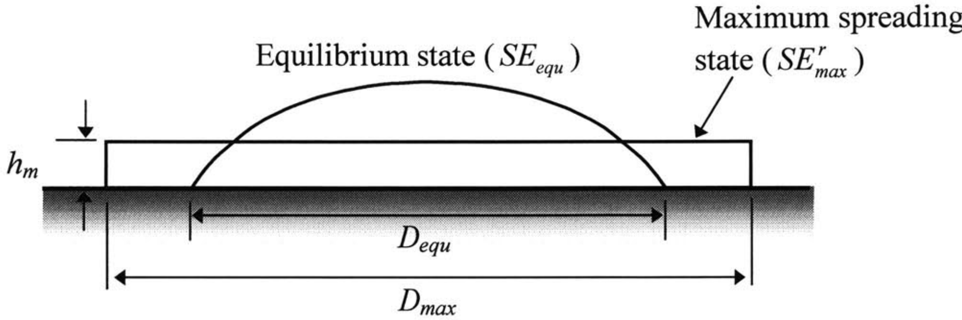

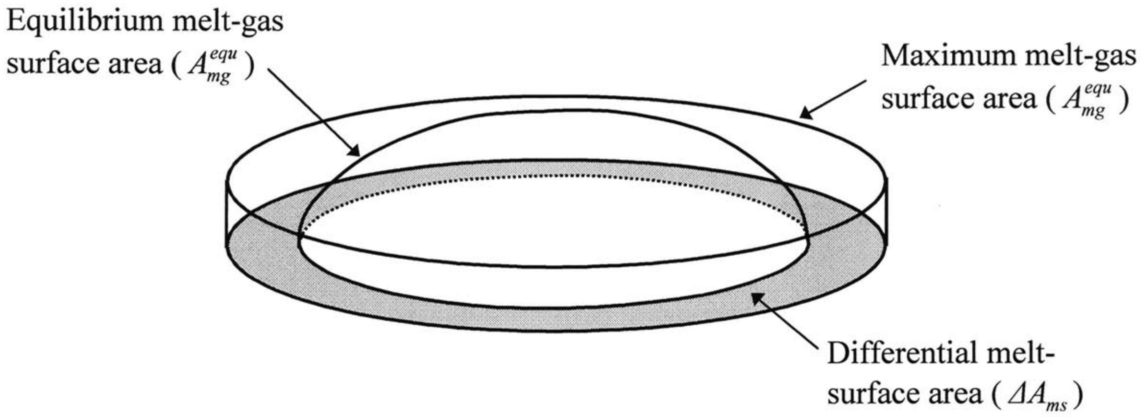

Figure 2.6. Energy difference between the maximum spreading and equilibrium states as potential for droplet bouncing.

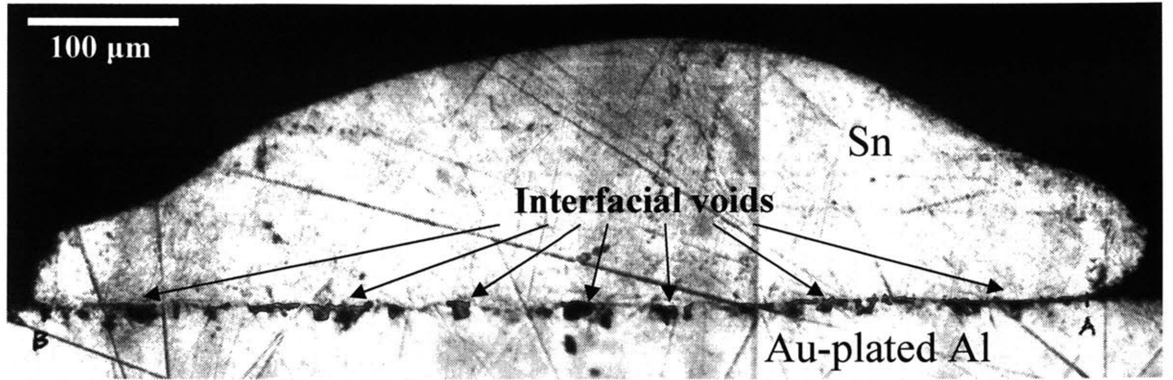

Figure 2.7. Highlighted void formations shown at the interface of a Sn bump deposited on Au-plated, as-rolled Al plate.

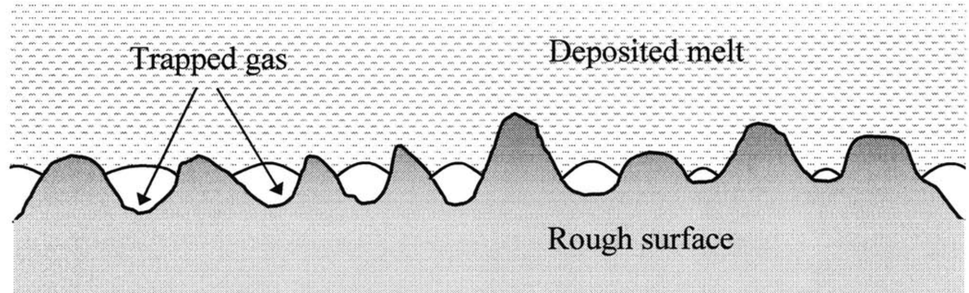

Figure 2.8. Roughness-induced gas entrapments and the resulting composite melt-surface interface.

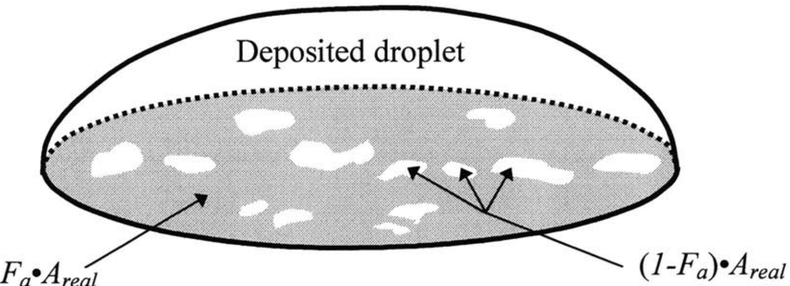

Figure 2.9. Schematic describing the effective area fraction, $F_a = A_{eff} / A_{real}$. A_{eff} is the contact area between the melt and surface, while A_{real} is the total area of a rough surface.

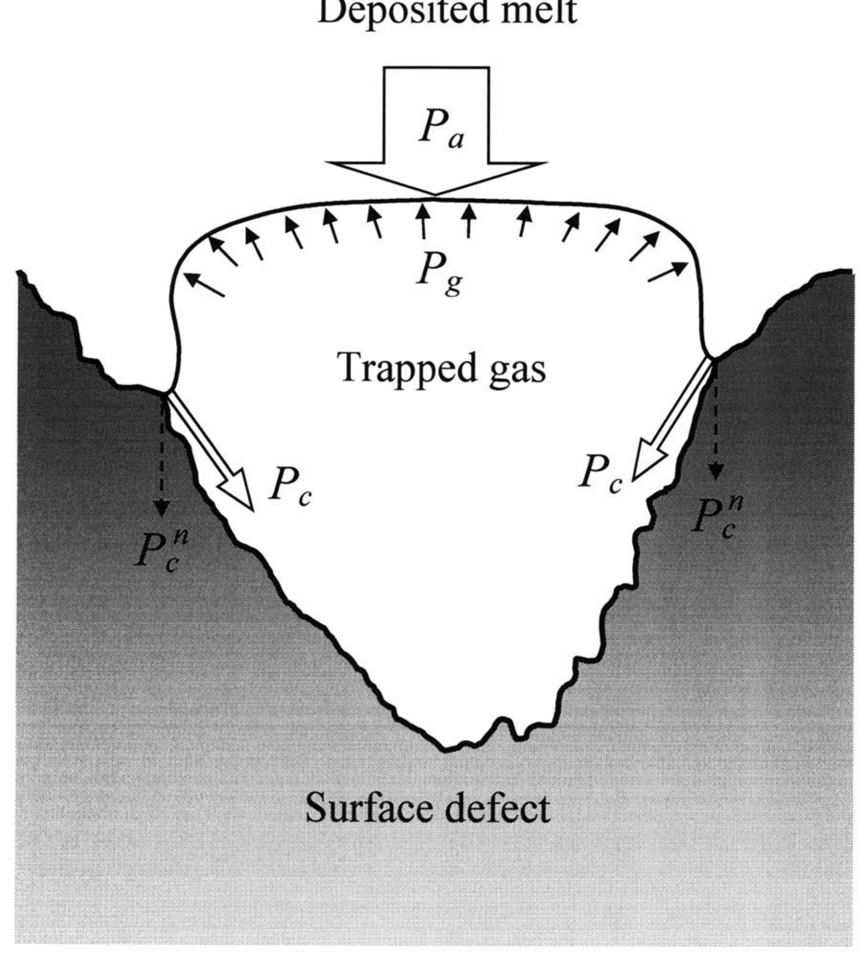

Figure 2.10. Schematic of the force components controlling melt penetration.

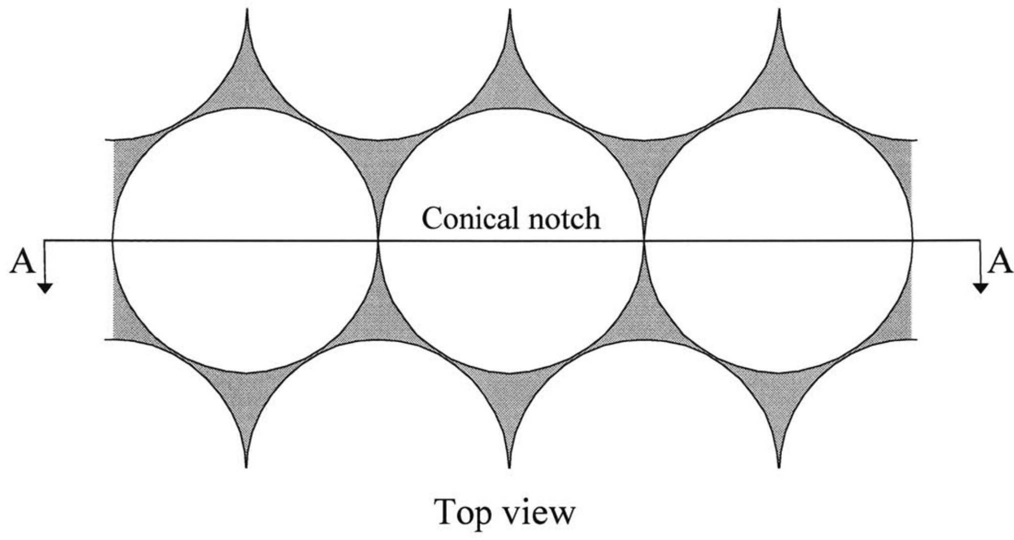

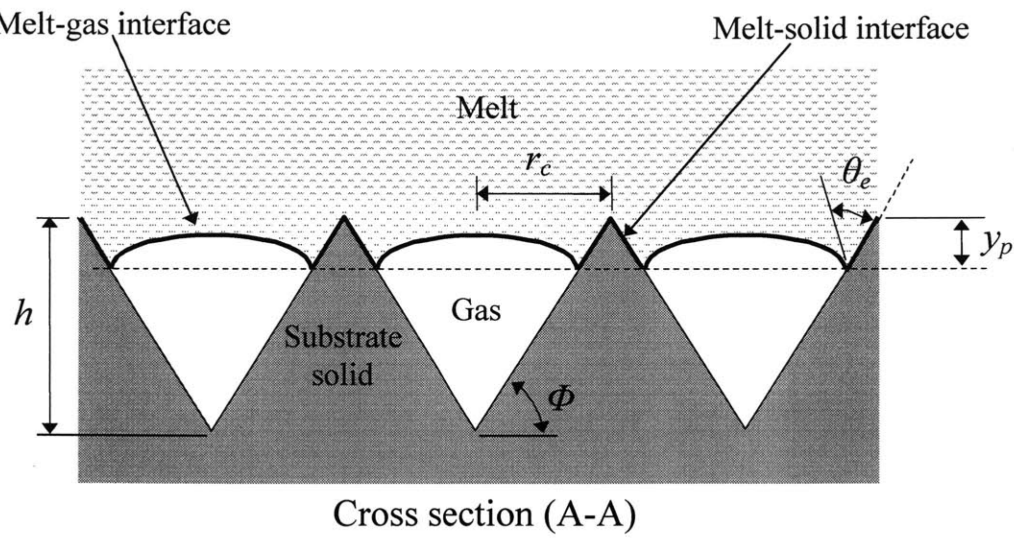

Figure 2.11. Schematic of the generalized rough surface model.

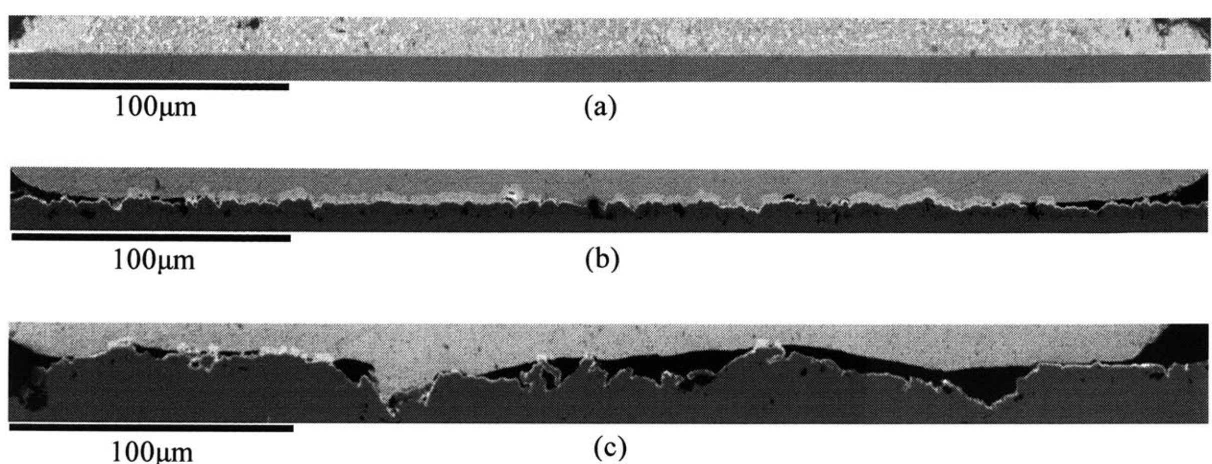

Figure 2.12. Characteristics of the interfacial voids formed between solder bumps and rough surfaces. (a) Pb-37wt% Sn bump on 0.3μm Al_2O_3 slurry polished, Au-plated surface. (b) Pure Sn bump on 27μm Al_2O_3 sandblasted, Au-plated surface. (c) Pure Sn bump on 180μm Al_2O_3 sandblasted, Au-plated surface.

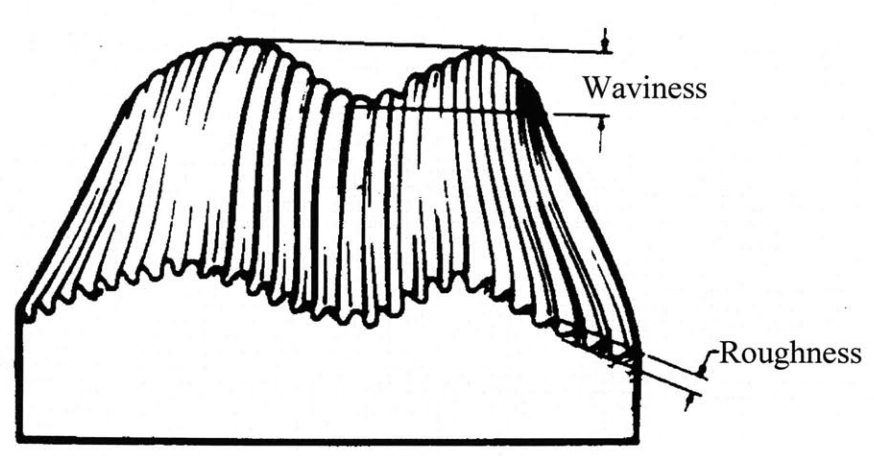

Figure 2.13. Illustration of the waviness, roughness, and general form of a surface. (Adapted from ASM Handbook, Volume 5: Surface Engineering)

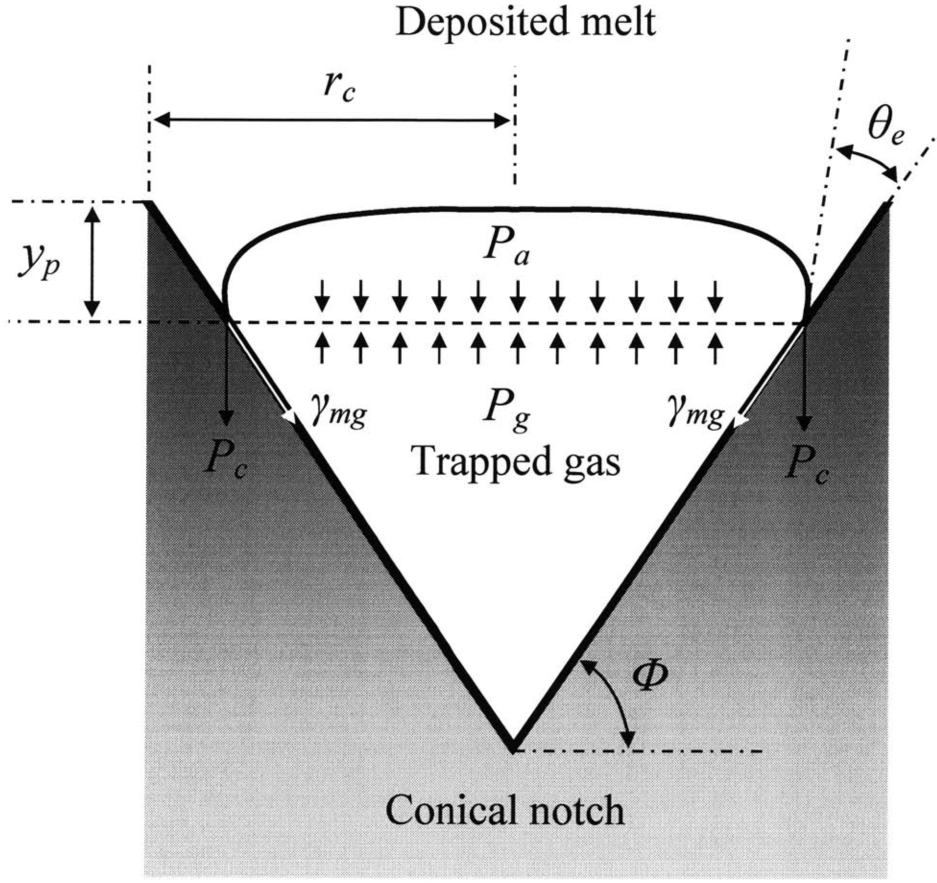

Figure 2.14. Force balance at the interface between the penetrating melt and the trapped gas in a conical notch.

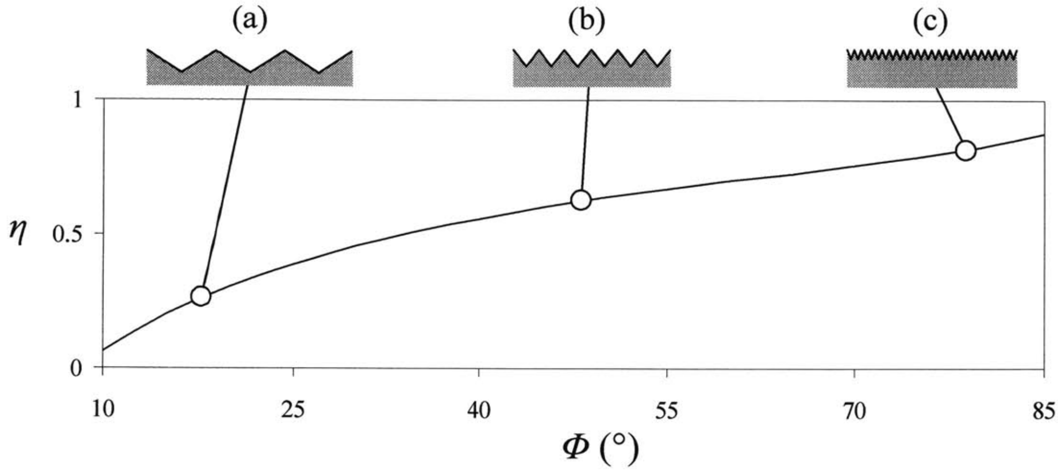

Figure 2.15. The melt penetration ratio y_p / h, as a function of the notch angle Φ. (a) rough surface with deep but shallow defects, (b) semi-rough surface with intermediately angled defects, and (c) smooth surface with small but sharply angled defects.

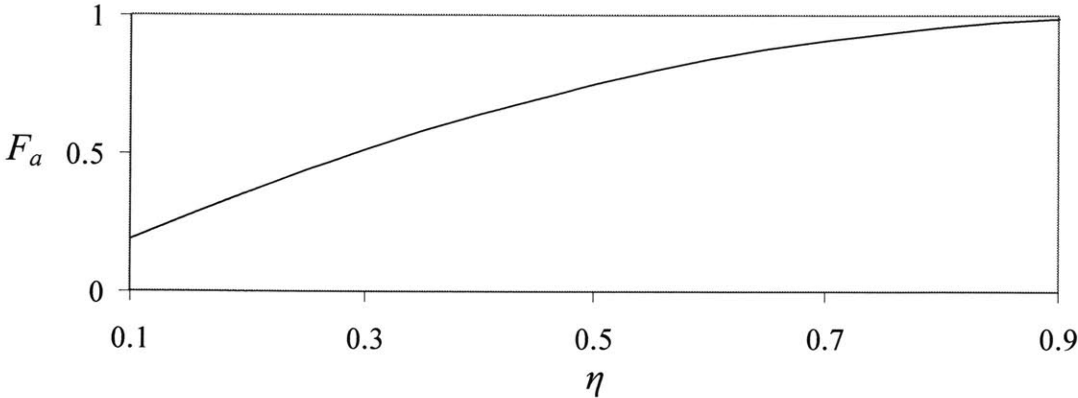

Figure 2.16. The effective area fraction, F_a, as a function of melt penetration ratio, y_p / h. y_p is the melt penetration depth and h is the depth of the notch defect.

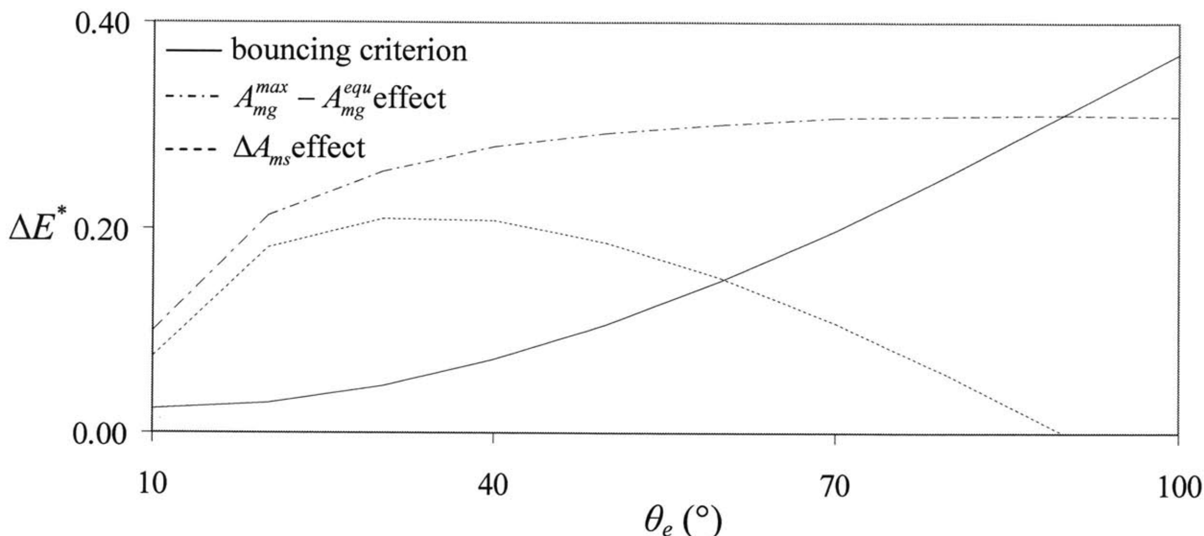

Figure 2.17. The effect of melt-surface wetting, represented by the equilibrium contact angle, θ_e, on the bouncing criterion. Droplet: Pb-37wt% Sn solder, D_{ini} = 300μm, u_{ini} = 4m/s, θ_{ad} = 110°.

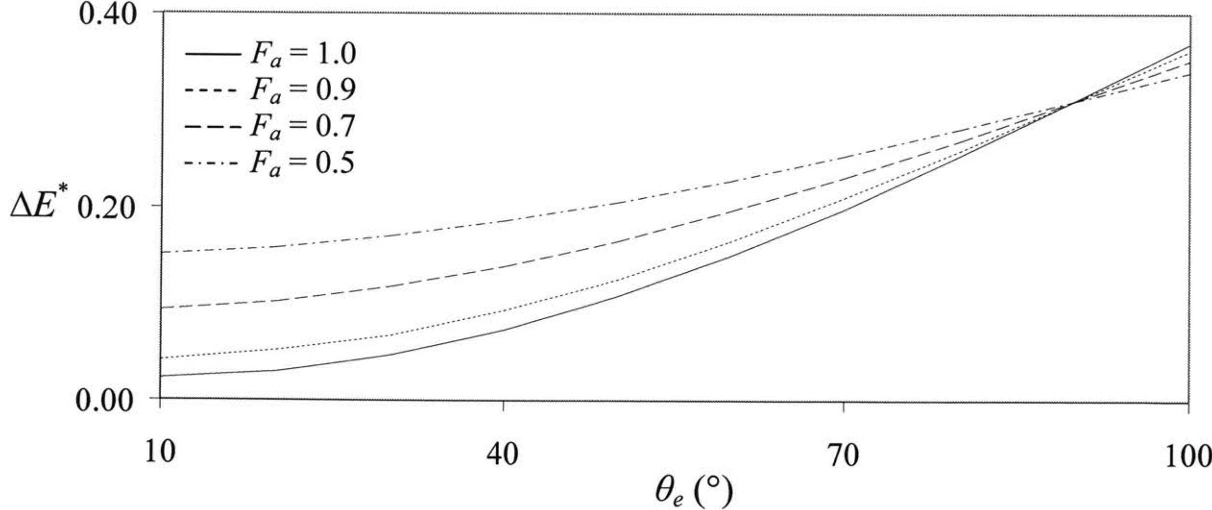

Figure 2.18. The effect of surface roughness, represented by the effective area fraction, F_a, on the bouncing criterion. Droplet: Pb-37wt% Sn solder, D_{ini} = 300μm, u_{ini} = 4 m/s, θ_{ad} = 110°.

CHAPTER 3. EXPERIMENTAL WORK

3.1 Introduction

The analyses presented in the previous chapter have provided the theoretical background on the mechanisms behind the effects of wetting and surface roughness on the droplet bouncing. The potential for droplet bouncing is predicted to increase with the deterioration of the wetting condition and increase in the substrate surface roughness. The aims of the experimental work are to verify these predictions by the study of results from the simulated solder bump formation on prepared substrate surfaces. Solder bumps were formed by depositing uniform-sized molten solder droplets on substrates prepared to approximate the surface conditions encountered in real-world applications. The occurrence of droplet bouncing was determined qualitatively by analyzing the morphologies of the solder bumps formed. To investigate the post-impact droplet spreading and recoiling in real time, the droplet deposition events were studied by high-speed imaging. The apparatuses and procedures used in the experimental studies and the observations made are presented in this chapter. Detailed analysis of the data collected and quantitative verifications of the analytical predictions are included in Chapter 4.

3.2 Droplet Generation

The molten solder droplets used in the experimental study were generated by the UDS process introduced in Chapter 1. The process produces a spray of uniformly sized droplets by breaking up a jet of molten metal by applying precisely controlled sinusoidal vibrations. The uniform droplet size allows easy prediction of the impact conditions of the droplets, since each droplet in the spray is considered to have the same kinetic and thermal energies. The ability to accurately determine the droplet impact conditions greatly improves the controllability and repeatability of the bump formation experiments. The UDS generator used in the experimental work, shown in Figure 3.1, consists of a stainless steel crucible with a bottom-mounted spray orifice, a heater and thermocouple, a vibration rod connected to a piezoelectric actuator, and a droplet charging plate. The stainless steel crucible is designed to hold approximately 180ml of melt. The metals inside

the crucible are melted by a 500W resistance band heater, and the melt temperature is controlled by a type-K thermocouple (Omega Engineering, KMTSS-020G-12) installed inside the crucible. The sinusoidal break-up vibrations are produced by a piezoelectric actuator constructed by stacking piezoelectric crystals (APC International, APC 850) between copper electrodes. The vibrations generated by the piezoelectric actuator are transmitted to the liquid metal jet through a 6.3mm diameter ceramic vibration rod immersed in the melt. The ceramic material is selected to insulate the piezoelectric crystals from the heat of the molten metals. The droplet charging plate, located approximately 4mm below the spray orifice, has an 8mm wide and 12mm tall channel in which the jet breaks up. By applying a static voltage to the charging plate, the capacitance between the plate and jet induces a charge to the tip of the metal jet. As a droplet breaks from the tip of the jet, it retains the charge it held the moment it broke free. The spray orifice is a laser-drilled sapphire nozzle mounted on the removable crucible bottom with a high-temperature ceramic adhesive. The size of the spray orifice controls the metal jet diameter, and hence the final droplet diameter.

For the experiments conducted in this study, spray orifices of 150μm in diameter were used to produce droplets with mean diameter of 285μm. Pure Sn, 99.99%, and Pb-37wt% Sn eutectic solder were selected as the droplet materials. The spray process generates approximately 4500 droplets per second for the given droplet size, with an estimated diameter variation of less than ±3%. Static voltage up to 1500V was applied to the charging plate to disperse the droplets and to prevent merging. The scattering pattern and the in-flight droplet velocity profile were predicted by the trajectory model developed by Passow [1992]. The analysis estimated the impact velocity of the droplets to range from 2.9 to 4m/s, depending on the charging voltage applied and the droplet flight distance. Based on the in-flight droplet cooling model developed by Chen [1996], the initial melt temperature was controlled so that the droplets were fully liquid when impacting the substrate surfaces. The typical droplet generation parameters are shown in Table 3.1.

3.3 Substrate Preparation

To simulate the typical surface conditions encountered in solder bumping applications, the structures of typical solder bumping targets are analyzed to determine the essential parameters

that need to be replicated in the bumping experiments. The schematic of a typical flip chip interconnection is shown in Figure 3.2. As shown in the figure, the solder bump is connected to the contact pads in the Si wafer and the PCB board through layers of deposited metals known as under bump metallization (UBM). The UBM usually consists of an adhesion layer if the contact pad is not solder-wetting, a barrier layer, and a wetting enhancing top layer. The adhesion layer is typically made of plated Cu that is wet well by solders if it is not heavily oxidized. The barrier layer has two material requirements. First, since the barrier layer will be exposed to the solder bump materials after the top wetting layer is consumed during the reflowing operation, the barrier layer material has to be solder-wetting. Second, the barrier layer needs to prevent interconnection failure through spalling. Spalling is the detachment of intermetallic compound (IMC) grains from the UBM/solder interface after total UBM consumption by excessive IMC growth. Ni-P alloy is adequately wet by solders and has a much slower IMC growth rate than Cu. In addition, it can be applied to the UBM through an inexpensive, electroless and mask-free process. Therefore, electroless Ni-P has increasingly become the material of choice for the barrier layer of the UBM. The wetting enhancing layer is usually a thin layer of noble metal or solder material that protects the UBM from oxidation while providing a favorable wetting surface for soldering. The UBM wetting layers are typically consumed quickly by the solder bump materials during the reflow operation. Au and Sn-alloy are the traditional materials used for the wetting layers. However, Pd or Rh wetting layers are also employed in the military or other more specialized applications. Modeled after these UBM structures, the substrates used in the experimental work were also prepared in the similar layered fashion.

To study the effects of droplet-surface wetting on bouncing, 50mm by 75mm Cu plates, 3mm in thickness, were polished using 0.3μm aluminum oxide (Al_2O_3) slurry in an automated polishing machine. The Cu plate was mounted to a holder and pressed against a polish platter rotating at 60RPM. The polishing pressure is set at a constant 35kPa for the 10-minutes polishing duration. The resulting surfaces were measured to have Ra values less than 0.02μm. Ra is defined as the arithmetic average of the deviations from the mean height of the surface. The smooth surfaces eliminated surface roughness as a variable in the wetting experiments. Different materials were then plated on these polished plates sequentially. A 15μm-thick barrier layer of electroless Ni-P was applied first, followed by a 0.5μm-thick wetting layer. Since the ultimate goal of this study was to establish a general rule on how surface wetting affects bouncing, wetting conditions range

from wetting to non-wetting are simulated. To simulate the wetting conditions encountered in the actual bumping applications, typical top-plating materials used in electronic packaging were selected: Au, Pd, Rh, and Sn. The semi-wetting condition was simulated by either the un-plated, electroless Ni-P surface or the bare, polished Cu surface. The non-wetting condition was simulated by bare, 3mm-thick Al plate polished in the manner described earlier. The surface wetting characteristics were quantified by measuring the contact angles of the sessile drops of molten Sn or Pd-37wt% Sn solder on these prepared substrates. The drops used for the contact angle measurements were formed by spraying droplets on to the prepared surfaces at room temperature to form splats. The quenched splats were then reflowed into sessile drops inside the inert gas-filled spray chamber. The profile images of the reflowed drops on surfaces were taken using an imaging system consisting of a CCD camera (Panasonic, Model WV-BP-310), a PC equipped with a frame grabber card (Data Translation, DT-3155), and a coaxial illumination light source (Volpi, ILP™ CIS 25W). The schematic of the contact angle measurement setup is shown in Figure 3.3. The contact angles at both edges of the sessile drop were measured. Typically, about 10-15 drops were measured for each drop-substrate combination. The final values of the static contact angles were the averages from these individual measurements. The wetting substrate preparations and the measured static contact angles are summarized in Table 3.2. The contact angle for Sn drop on Sn-plated substrate is considerably larger than expected for homologous deposition. Since freshly plated Sn oxidizes readily in air, the resulting oxide layer is most likely responsible for the poor wetting condition.

To study the effects of surface roughness on bouncing, uniformly distributed, random defects were created on the surfaces of the bumping substrates by sandblasting. This type of defect structure is considered a good approximation of the surface characteristics observed on the typical solder bumping substrates. The roughness levels produced by sandblasting are controlled by the mean particle size of the blasting abrasives used. For the substrates used in the roughness-effect experiments, abrasives of 27μm and 180μm particle sizes were selected to roughen the substrates. Sandblasting using the fine abrasives was conducted in a tabletop micro-sandblaster (S.S. White Technologies, Airbrasive 6500 system). 50mm by 75mm Cu plates, 3mm in thickness, were loaded into the work chamber and positioned by hands through the chamber access armholes. Dry, 27μm Al_2O_3 abrasives (S.S. White Technologies, Airbrasive powder #1) were loaded into the powder reservoir and propelled by compressed N_2 through a handpiece

fitted with a carbide nozzle into a spray. The carbide nozzle generated a line abrasion pattern roughly 10mm wide at the 40mm working distance. The handpiece was manipulated to direct the abrasive spray toward the Cu plate. Multiple passes were made in different directions to ensure that the Cu surface was uniformly abraded. Sandblasting using the coarser abrasives was performed in an industrial sandblasting chamber (Skat Blast, Dry Blast System). Standard 80 grit Al_2O_3 abrasives with equivalent particle size of 180μm were loaded and propelled through the spray nozzle by compressed air. The nozzle generated an abrasion pattern roughly the size of the Cu plate processed. Again, several passes were made to ensure that the Cu surface was evenly abraded. A third set of Cu plates was polished using 0.3μm Al_2O_3 slurry in an automated polishing machine. Identical polishing parameters used to polish the wetting test substrates were adopted. The resulting smooth surfaces represent the lower limit of the surface roughness gradient created for the roughness effect experiments.

The sandblasted and the polished Cu plates were cleaned ultrasonically in a methanol bath for 30 minutes and wiped dry with low-lint tissues. Optical microscopic inspection of the sandblasted surfaces revealed that Al_2O_3 particles up to 5μm in size were embedded in the soft copper surfaces. Application of a 15μm-thick layer of electroless Ni-P successfully covered the exposed Al_2O_3 particles. However, the Ni-P barrier layer unexpectedly smoothed the roughened surfaces by filling in the defects created by sandblasting. Since protecting the base Cu from the long term solder erosion was not a priority for the proposed experiments, the Ni-P barrier layer is replaced by a 10μm-thick acid Cu plating. Post-plating inspection showed that the embedded Al_2O_3 particles were covered while the surface defect structures were preserved. Both the sandblasted and polished substrates were then plated with a 0.5μm-thick layer of Au to create evenly wetting surfaces. The surfaces roughness levels of the prepared substrates were quantified using a stylus profilometer (Tencor P-10 Surface Profiler). The resulting surfaces were measured to have an average roughness, Ra, ranging from 0.02μm to 2.2μm. The roughness level covered the range typically encountered in solder bumping applications, from less than 0.06μm Ra for wafer UBM to around 0.5μm Ra for BGA pads. The summary of the roughness substrate surface properties is shown in Table 3.3.

3.4 Solder Bump Morphology Study

Since droplet bouncing leads to either complete or partial detachment of the deposited droplets from the target surfaces, its occurrence may be determined by analyzing the shapes and sizes of the solder bumps collected from the deposition experiments. In the cases when complete droplet detachments are prevalent, the low population densities of the solder bumps collected may be used as indicators for the occurrences of bouncing.

3.4.1 Experimental apparatus and procedures

The solder bumps analyzed in the morphology study were collected inside the spray chamber of a standard UDS apparatus. The spray chamber consists of a sealed glass column roughly 300mm in diameter fitted with vacuum port and several accessory feedthroughs. The schematic and photographs of the experimental setup are shown in Figure 3.4. The prepared substrates were cut into coupons, roughly 25mm long and 5mm wide. The coupons were ultrasonically cleaned in a methanol bath for 15 minutes and wiped dry with low-lint tissues. The cleaned coupons were mounted onto a testing jig installed inside the spray chamber. The coupon holder on the testing jig was designed to accommodate multiple coupons simultaneously for bump collections. The vertical position of the coupon holder was adjustable according to the desired droplet flight distance. For the bump morphology study, a fixed position of 200mm below the spray orifice was selected. The temperature of the test coupons was controlled by two 20W cartridge heaters embedded in the coupon holder. A bolt-on type-K thermocouple (Omega Engineering, Model WTK-6-S-12) and a heater controller (Watlow Electric, Series 96) provided closed-loop temperature control. The features of the testing jig are shown in Figure 3.5.

The experimental procedures developed for this study are described below. First, approximately 700g of 99.99% pure Sn pellets are loaded into the UDS generator crucible. The generator assembly is then installed onto the UDS apparatus and the air inside the spray chamber is evacuated using a rotary vacuum pump. When the vacuum level reaches 100 mTorr, the chamber is filled to the atmospheric pressure with 95% nitrogen-5% hydrogen gas mixture. A minimum of three repeats of this vacuum-refill sequence are performed before the test chamber is pressurized to 35kPa gauge pressure. To minimize oxidation during melting, the chamber oxygen content is sampled using an oxygen analyzer (Illinois Instruments, Model 2550). The

heating of the crucible and its contents will commence only when the oxygen level is measured to be below 50 ppm. When the metal pellets are fully molten and the melt temperature stabilizes at the preset point, the crucible is pressurized with inert gas to eject the melt through the spray orifice. The liquid metal jet is broken into droplets by the sinusoidal vibrations imposed through the piezoelectric actuator on the UDS generator. A video imaging system consists of a CCD video camera (Pulnix, TM-7X) and a CRT display is used to monitor the jet break-up process. The generated droplets are illuminated by placing a stroboscope (Pioneer Electric and Research, DS-303) behind the droplet spray. The stroboscope is synchronized to flash at the jet perturbation frequency. When the jet break-up becomes uniform, its break-up frequency will match the flashing of the stroboscope and the droplets will appear to be frozen in space. Image of a stationary train of uniform-sized droplets on the CRT display, as shown in Figure 3.6, indicates that bump collections may proceed.

After a stable droplet spray is established, the spray mass flow rate is measured by timed droplet collection using a stainless steel cup mounted on the testing jig. The mass flow rate obtained is used later to determine the droplet impact velocity. Static voltage up to 1500V is then applied to the charging ring to induce charges onto the droplets, and hence dispersing the droplet spray. Prior to the collection of solder bumps, the test coupons are heated to approximate an isothermal deposition condition. Since the melting temperature of pure Sn is 232°C, the coupon surface temperatures are kept at 200°C to prevent re-melting and to preserve the bump morphologies. The solidification rate of the droplet deposited at this surface temperature is estimated by the model developed by Kim [1999] to ensure that bouncing will not be arrested by splat quenching. When the temperatures of the test coupons are stabilized at the set point, the coupons are rotated pass the droplet spray quickly to allow a small number of the sprayed droplets to deposit and form solder bumps on these coupons. The bumps are allowed to solidify fully in the inert gas-filled spray chamber before they are retrieved and analyzed.

3.4.2 Observations

The solder bumps collected on surfaces with different wetting properties are shown in Figure 3.7(a)-(g). The bump material is 99.99% pure Sn and the surface temperatures during bump formation are kept at 200°C. Figure 3.7(a) shows that the number of bumps collected on the

polished Al surface is significantly less than the numbers collected on the semi-wetting and wetting surfaces under equivalent deposition conditions. This observation indicates that complete droplet rebounds may have been prevalent during bump collections on the non-wetting Al surface.

The bumps collected on the polished Cu, Ni-P, and Sn-plated surfaces, shown in Figures 3.7(b)-3.7(d), consist mostly of mixed populations of well-formed bumps and remnants of bounced droplets. The diameters of the well-formed bumps typically range from 570μm to 620μm, while the remnants are usually less than 300μm in size and are irregular in shape. Clear evidence of bouncing is shown in the sub-frame of Figure 3.7(c), where circular residues left behind by bounced droplets are visible on the Ni-P surface. Energy dispersive spectrometry (EDS) performed using an X-ray spectrometer (JEOL USA Inc., JXA-733) has confirmed that these residues contain a significant amount of Sn compared with the surrounding surface, as shown in Figure 3.8. These observations suggest that a general transition from droplet sticking to bouncing behavior may have occurred on these surfaces. The predominant deposition behavior on these surface may be a mix of complete bouncing, sticking, and partial bouncing where only a portion of a deposited droplet is separated and rebounded off the target surface. These surfaces are shown to be marginally wetting to Sn, according to Table 3.2.

The majority of the bumps collected on Rh-plated, Pd-plated, and Au-plated substrates have symmetrical, spherical-cap shapes and are comparable in their diameters and population, as shown in Figures 3.7(e)-3.7(g). These characteristics indicate that bouncing is most likely absent during bump collections on these surfaces. Sn is shown to exhibit good to excellent wetting behavior on these surfaces, according to Table 3.2.

Small, spherical bumps roughly 150 to 200μm in diameters, as indicated in Figure 3.7(e)-3.7(g), are also observed in contrast to the well-formed bumps typically collected on the wetting surfaces. Similar bumps are also found alongside the bumps and remnants collected on the semi-wetting surfaces, as shown in the sub-frames of Figure 3.7(b)-3.7(d). These smaller bumps are neither of irregular shape nor surrounded by the tell-tale circular residues that are characteristic to the remnants of bounced droplets. Instead, these bumps are almost perfectly spherical and are only weakly adhered to the surfaces. There are two possible sources of the smaller droplets

needed to form these smaller bumps. First, the smaller droplets may be the secondary droplets produced through partial bouncing. When bouncing leads only to partial detachment of a deposited droplet, the detached portion will quickly restore back to a small droplet while moving away from the surface. If the trajectory of the detached droplet leads it back toward either the original or the adjacent substrate surface, it can re-deposit and form the smaller bump observed. However, the nearly spherical shapes of these smaller bumps suggest that they may have been mostly solidified prior to impacting the surface. Considering that the main droplets are completely liquid at impact and the surface temperatures are maintained near the droplet melting temperature during deposition, it is reasonable to assume that the detached secondary droplets are, at least, mostly liquid. Therefore, it is unlikely that there will be sufficient time for these secondary droplets to solidify in the chamber atmosphere before re-deposition. The elimination for the first option suggests that these smaller bumps are most likely the deposition of satellites produced alongside the uniform droplets generated through the UDS process. The formation of satellites in UDS process were first observed and documented by Passow [1992]. As a droplet breaks off from the tip of the perturbed liquid metal jet, the neck-off region may not separate cleanly and a second, smaller droplet is sometimes produced, as seen in Figure 3.9. The occurrence of this phenomenon was found to be associated with the random variations in the frequency and amplitude of the jet perturbation vibrations, as well as changes in the jet velocity. The satellites are usually less than one third in diameter compared with the primary droplets generated, thus will mostly solidify before they impact the substrate.

Figure 3.10 shows the Sn bumps collected on coupons with decreasing surface roughness. The surface temperature has been kept at 200°C during collection. Figure 3.10(a) shows that virtually no bump was collected on the 180μm Al_2O_3 sandblasted surface, indicating that droplet bouncing and the subsequent complete detachments of the deposited droplets were prevalent. The bumps collected on the 27μm Al_2O_3 sandblasted surface consist of mostly well-formed bumps with spherical-cap shape and a few remnants and residues left behind by bounced droplets, as indicated in Figure 3.10(b). Elemental analysis confirmed that significant amounts of Sn exist in these residues, as shown in Figure 3.11. Figure 3.10(c) shows that the bumps collected on polished surface have symmetrical, spherical-cap shapes and population density comparable to the densities observed on the Au-plated, Rh-plated and Pd-plated surfaces. These observations suggest that droplet bouncing might not have occurred on the polished surfaces.

Irregular bumps roughly 2-3 times larger than the typical bumps collected are observed on both the 27μm Al_2O_3 sandblasted and polished surfaces, as indicated in Figure 3.10(b) and 3.10(c), respectively. The non-circular bases of these larger bumps suggest that they might be created through the merging of the adjacent bumps before they were solidified.

In spite of the aforementioned irregularities, the observations from the bump morphology study generally confirm the trend predicted by analysis. Specifically, the dominant droplet deposition behavior transits from bouncing to sticking as the droplet-surface wetting improves. In addition, increases in the surface roughness level appear to increase the potential for droplet bouncing. However, its effect on the droplet deposition behavior at low roughness level is observed to be marginal.

3.5 High-speed Imaging Study

The observations from the bump morphology study confirmed the trends predicted by the analytical work. The results suggest that the potential for droplet bouncing decreases either as the droplet-surface wetting improves or as the surface roughness reduces. However, for the following reasons, the morphology study alone does not supply sufficient information to quantitatively verify the analytical work presented in Chapter 2.

First, the results from the bump morphology experiments provide no information on the transient behavior of a deposited droplet. According to the analytical work presented in Chapter 2, the potential for droplet bouncing is described as a function of the maximum spreading diameter, D_{max}. D_{max} is a dynamic parameter measurable only in a short time between the initial spreading and recoiling phases of a deposited droplet. The base diameter of a solidified solder bump may be used as an order-of-magnitude approximation of D_{max}. However, unless the solidification time during the deposition of the solder droplet can be accurately predicted and controlled so that it matches the droplet spreading time, the validity of this type of approximation is questionable.

Second, the sub-melting surface temperatures maintained during solder bump formation, while necessary to preserve the bump morphologies, may have unspecified effects on the droplet deposition behavior. The substrate temperature is selected to ensure that complete bouncing is not arrested through quenching. Deposits made on Al and 180μm Al_2O_3 sandblasted surfaces

confirm that complete bouncing appears to be unaffected by the sub-melting surface temperatures, probably because of the increased thermal resistance of the roughened surfaces. However, majority of the bumps collected on the other surfaces exhibit rippled morphologies. Particularly well-preserved examples of these rippled solder bumps can be found on Pd-plated surface, as shown in Figure 3.7(g). The surface ripples on a solidified sessile drop are features of simultaneous solidification during the oscillation phase of a deposited droplet [Waldvogel and Poulikakos, 1997]. While a completely bounced droplet may be unaffected due to the relatively short period of time it spends attached to the surface, a small amount of cooling may be sufficient to arrest a partially bounced droplet.

In order to address these issues, it becomes necessary to observe and measure the droplet deposition behavior in real time. Studying a short duration event, such as the impact and spreading of a microdroplet, in real time inevitably requires high-speed imaging techniques. Using high-speed imaging techniques to study droplet deposition behavior have been explored for more than a century. Worthington [1876] pioneered the use of the single-shot flash-photographic technique to analyze the droplet deposition behavior. The process involves using precisely timed high-intensity flashes to expose photographs of droplets at different instants of their impact and spreading progressions. If the droplet impact parameters and the surface properties are both repeatable, the entire droplet deposition event can be reconstructed by piecing these images together as one continuous sequence. The flash-photographic technique produces excellent quality images at recording speed limited only by the duration of the flash and the resolution of the timing offset. However, the implementation of the flash-photographic technique requires precise detections of the impinging droplets in order to properly trigger the exposure flashes. For very small droplets traveling at high velocities, such as the ones generated from the UDS process, this requirement presents a formidable experimental challenge.

Alternatively, the images of a single droplet at different stages of deposition on a surface can be obtained by recording the event continuously using a high-speed video system. The advantage of this approach is that the accurate information about the timing and the location of droplet impact is not required, provided that the recording duration and the imaging field of view are both sufficiently large. The high-speed video systems are available commercially in either film or digital format. The typical film-based systems have better resolution and are currently

capable of delivering higher frame rates than the digital systems. However, the recording duration of a film-base system tends to be rather limited due to the amount of film the video equipment can reasonably handle per recording session. On the other hand, the latest digital high-speed video systems are capable of outputting the captured image data into mass storage devices in real time. By employing storage devices with sufficient capacities, large recording durations can be achieved even at high frame rates. In addition, the high sensitivities of the imaging chips used in the newer digital systems allow successful image acquisition even in poor lighting situations. Therefore, a digital high-speed video system was adopted to conduct the high-speed imaging study of the droplet deposition behavior.

3.5.1 Experimental apparatus and procedures

The deposition experiments for the high-speed imaging study were conducted in a UDS apparatus similar to the one employed for the bump morphology study. A 165mm diameter spray chamber was used due to the short working distance of the objective lens used with the high-speed video camera. The working distance is defined as the distance between the front vertex of a lens and the imaged object. The overall height of the spray chamber was increased by 270mm due to the addition of a top-mounted stainless steel observation chamber. The observation chamber was installed to shield the CCD camera and stroboscope used for monitoring the jet break-up from the bright illumination required for high-speed imaging. Due to this increase in the chamber height, the droplet flight distance prior to impact was increased to 350mm. Due to the longer droplet flight distance, melt temperature was increased to compensate for the extra cooling effect. However, the increased oxidation potential at elevated melt temperature caused the jet break-up using pure Sn to become unstable. Therefore, Pb-37wt% Sn eutectic solder at 260°C was substituted as droplet material. The prepared wetting and roughness test substrates were cut into 5mm-square test coupons. Since the lens setup on the high-speed video camera produced a image with shallow depth of field, defined as the distance between the nearest and farthest objects in a image that appear in acceptably sharp focus, the test coupon was prepared so the droplets deposited only on a thin strip of the prepared surface positioned on the focal point of the lens used. The coupon preparation and the schematic of the imaging optical setup are shown in Figure 3.12. The coupons were cleaned ultrasonically in a methanol bath for 15 minutes and wiped dry with low-lint tissue. A single cleaned coupon was mounted onto a

testing jig installed in the spray chamber. A single 20W cartridge heater was incorporated into the coupon holder to control the temperature of the test coupon. A miniature K-type thermocouple (Omega Engineering, Model KMTSS-062U-6) and a heater controller (Omega Engineering, CN9000A) were used to provide closed-loop temperature control. The details of the testing jig are shown in Figure 3.13.

A digital high-speed video system (Photron, Fastcam ultima SE) was used to record the droplet deposition event. The system employs an N-MOS image sensor with equivalent ASA film speed of 3000 and is capable of recording up to 40,500 frames per second. The built-in system memory allows recording of event up to 3.2 seconds at the maximum frame rate. A variable zoomed microscopic lens (Meijilabax, UNIMAC) with a 2X teleconverter (Cosmicar/Pentax, C80001) installed was used with the video camera. A magnification ratio of approximately 15 microns per image pixel was achieved with this optical setup. Due to the high reflectivity of the molten metal droplets, uniform illumination by direct lighting proved to be extremely difficult. However, a well-contrasted shadow image was obtained by backlighting the impinging droplets and the test coupon with a 300W halogen lamp (Vision Research, NorthStar). A second lamp (Lowell-Light, Omni 500W) was positioned in front of the test coupon to add highlights to the impinging droplets during deposition. The highlights structured the images so three-dimensional information could be extracted from the two-dimensional images. The schematic and image of the high-speed imaging setup are shown in Figure 3.14.

Before recording the droplet depositions, the uniform solder droplet spray was generated as described in the previous section. A waste cup was used to block the droplet spray while the test coupon was heated to its preset temperature. Since preserving the bump morphologies was no longer a concern, the coupon was heated to the melting temperature of the droplet material, i.e. 183°C for Sn37%wtPb eutectic solder, to ensure an isothermal deposition condition. The video camera was adjusted to focus on the test coupon surface and set to record in a continuous loop. The recorded images were played back in real time on the LCD screen of a laptop computer (Gateway, Solo 9550) connected to the camera system. The waste cup was then removed to allow droplets to impinge onto the test coupon. When bumps were seen forming on the coupon surface, a trigger signal was sent to the camera system via a manual remote control. The trigger signal commanded the camera system to save the captured image sequences to its internal

memory before terminating the recording session. The saved image sequences were retrieved later for analysis.

3.5.2 Observations

The high-speed image sequences of solder droplets depositing on surfaces with different wetting properties are shown in Figure 3.15(a)-(c). Bouncing sequences of a Pb-37wt% Sn solder droplet deposited on a Sn-plated surface are shown in Figure 3.16(a). The deposited droplet deforms and spreads radially immediately after impact. The resulting splat is shown spreading to its maximum diameter within approximately 150μs after impact. The splat at this stage resembles a flat disk. After a momentary stop, the splat begins to retract back toward the point of impact. A rapidly rising peak is visible at the center of the retracting splat at 300μs after impact. The splat morphs into a tear-drop shaped column as the splat base continues to shrink. At approximately 550μs after impact, the column disengages completely from the surface and starts moving upward. At 950μs after impact, the upward moving column can be seen transforming into a spherical shape. Similar bouncing sequences were also recorded for solder droplets deposited on polished Al and Cu surfaces.

Partial bouncing behavior was recorded for solder droplets deposited on Rh-plated surface. The sequences are shown in Figure 3.15(b). The initial spreading phase is shown to be similar to the bouncing case, and the splat reaches its maximum spreading diameter by 150μs after impact. A less aggressive retraction phase is observed following the initial spreading. A center peak with lower elevation is visible at about 350μs after impact. The growth of the center peak becomes minimal at 550μs after impact. However, the upward flow of the splat melt appears to continue as a secondary droplet starts to form at the tip of the peak at 650μs after impact. This secondary droplet separates from the rest of the splat and moves upward at 850μs after impact. The remaining portion of the deposited splat retracts back toward the surface and oscillates until an equilibrium bump is formed after 1.6ms.

Sticking behavior was observed when solder droplets were deposited on good wetting surfaces. Sequences of a solder bump forming on the Pd-plated surface are shown in Figure 3.15(c). The maximum spreading diameter is again reached within 150μs after impact. A subtle retraction phase with minimal splat base shrinkage is observed following the initial spreading. On the

other hand, the splat oscillation begins almost as soon as the initial spreading phase ends. The base diameter of the deposited splat remains nearly constant while the main splat body oscillates for an extended period of time. The oscillation becomes minimal after 1.2ms post-impact and an equilibrium bump is formed after 1.6ms.

Images of solder droplets depositing on surfaces with different roughness levels are shown in Figure 3.16. Figure 3.16(a) shows that a solder droplet deposited on polished surface exhibits similar sticking behavior as observed in Figure 3.15(c). The deposited splat reaches its maximum spreading diameter at around 160μs after impact. A retraction phase consists of minor splat base shrinkage and an extended splat oscillation period is observed following the initial spreading phase. A center peak is observed at around 330μs after impact and reaches its maximum height at approximately 500μs. An equilibrium solder bump is formed after 1.6ms.

Figure 3.16(b) shows the sequences of a solder droplet depositing on the 27μm Al_2O_3 sandblasted surface. The increase in surface roughness appears to induce flow front instability during the initial spreading phase. This instability manifests into minor edge irregularities as the splat reaches its maximum spreading diameter at around 165μs after impact. However, the effect of the instability observed appears to be relatively minor. The edge irregularities are quickly damped out at the onset of the flow front retraction. The recoiling droplet incurs a slightly greater base shrinkage compared with the droplet deposited on the polished surface. Consequently, the center peak formed near the end of the droplet recoiling exhibits a greater girth which indicates that more melts are flowing upward, away from the target surface. The growth of the center peak ceases at around 550μs and an equilibrium bump shape is reached at around 1.6ms after impact.

Significant changes in the droplet deposition behavior were observed when a solder droplet was deposited on the 180μm Al_2O_3 sandblasted surface, as shown in Figure 3.16(c). The severity of the flow front instability in the initial spreading phase increases as the surface roughness increases, and large lobes at the splat edge are visible as the splat reaches its maximum diameter at 160μs after impact. After a slight hesitation at maximum spreading, an aggressive retraction phase with significant splat base shrinkage starts at around 330μs after impact. Instead of developing a distinctive center peak as observed in Figure 3.15(a), the splat consolidates and

rises upward into a column starting at 495μs after impact. In this particular case, the upward motion of the splat melt does not lead into either complete detachment or the formation of a secondary droplet. Instead, the growth of the column ceases at 660μs after impact. The column then collapses back toward the surface and an extended period of splat oscillations follows. An equilibrium bump with smaller base and a more hemi-spherical shape is formed after 1.6ms.

In summary, the results from the high-speed imaging experiments complement the observations from the bump morphology study. The tendency for a deposited droplet to bounce appears to correlate positively with the deterioration of the surface wetting property. Increases in the surface roughness level are also associated with more aggressive droplet recoiling behavior and sights of bulk upward fluid motion that typically precede droplet bouncing. In addition, partial bouncing was observed on good wetting surfaces, such as Rh-plated Cu, suggesting that bouncing may be a concern even on standard wetting surfaces used in typical electronic applications.

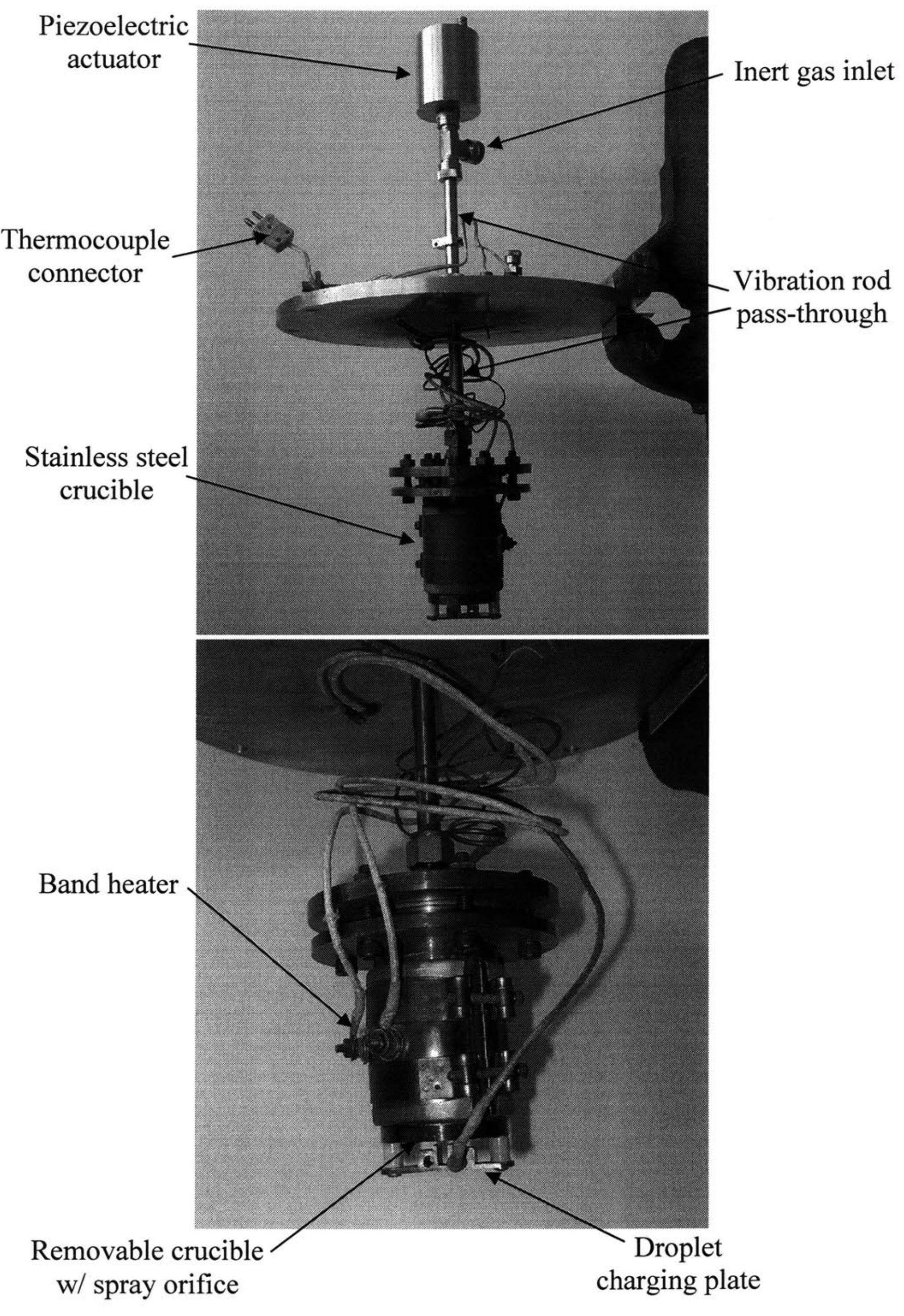

Figure 3.1. Uniform Droplet Spray generator.

Table 3.1. The droplet generation parameters for the experimental study.

Droplet materials:	Pure tin (Sn)	Solder (63%Sn37%Pb)
Density (kg/m^3):	7000	8420
Surface tension (N/m):	0.544	0.49
Viscosity (Pa·s):	0.0018	0.0013
Melting point (°C):	232	183
Initial melt temp. (°C):	280	260
Spraying orifice diameter (μm):	150	150
Average droplet diameter (μm):	285	285
Droplet generation frequency (Hz):	4500	4500
Ejection pressure (kPa):	103	103
Chamber pressure (kPa):	34	34
Chamber gas:	95%N_2-5%H_2	95%N_2-5%H_2
Droplet flight distance (m):	0.2	0.35
Droplet charge (V)	800-1500	500-700
Est. impact velocity (m/s):	3.0	3.8

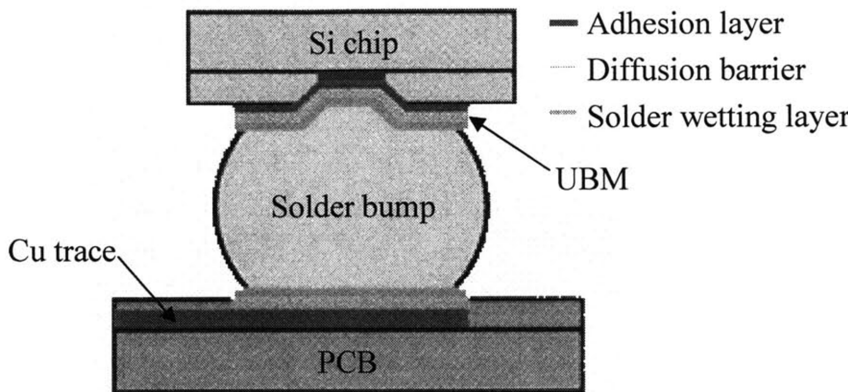

Figure 3.2. Schematic of a typical solder bump interconnect.

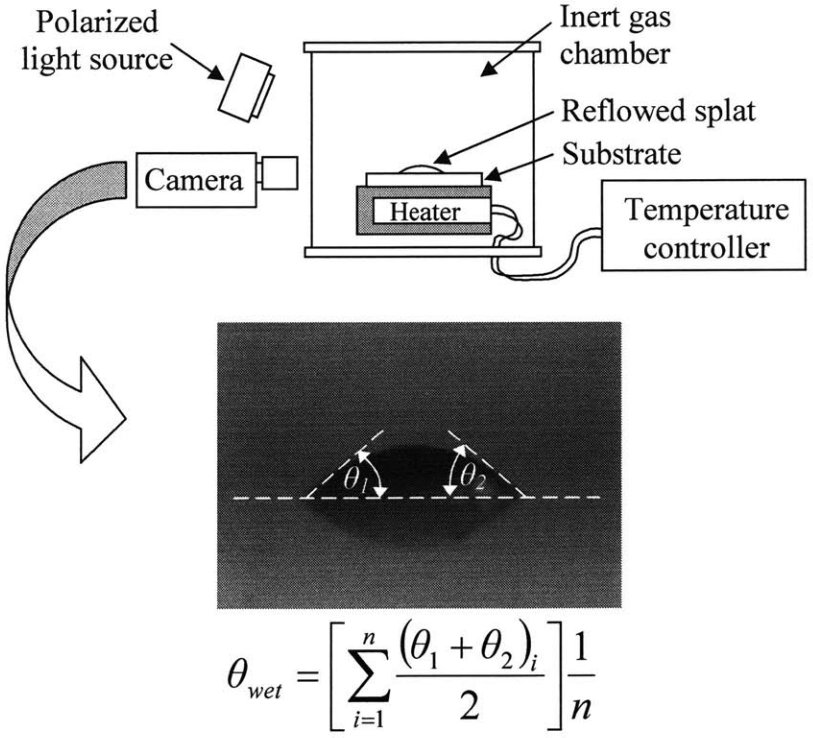

$$\theta_{wet} = \left[\sum_{i=1}^{n} \frac{(\theta_1 + \theta_2)_i}{2} \right] \frac{1}{n}$$

Figure 3.3. Quantification procedures for the wetting property of the prepared substrate. Note: the number of drop measured, n, is typically 10-15.

Table 3.2. Summary of the substrate preparations and the resulting wetting properties.

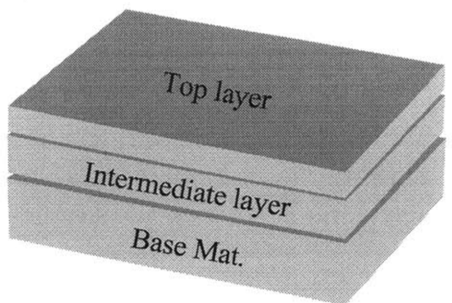

Base material	Base material prep.	Intermediate layer	Top layer	θ_{Sn} (°)[2]	θ_{solder} (°)[4]
Aluminum	Polished[1]	N/A	N/A	90[3]	90[3]
Copper	Polished[1]	N/A	N/A	42	65
Copper	Polished[1]	Electroless Ni	N/A	40	75
Copper	Polished[1]	Electroless Ni	Sn	54	72
Copper	Polished[1]	Electroless Ni	Rh	35	60
Copper	Polished[1]	Electroless Ni	Au	28	30
Copper	Polished[1]	Electroless Ni	Pd	23	25

[1] Polished using 0.3μm Al_2O_3 slurry
[2] Measured with reflowed Sn droplet
[3] Estimated value
[4] Measured using high-speed images of droplet depositions

Table 3.3. Summary of the substrate preparations and the resulting roughness properties.

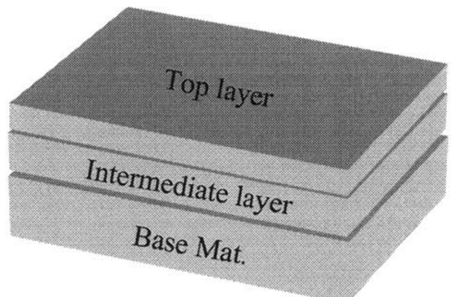

Base material	Base material prep.	Intermediate layer	Top layer	Ra (μm)
Copper	Polished[1]	N/A	Au	0.02
Copper	Sandblasted[2]	Cu-plating	Au	0.5
Copper	Sandblasted[3]	Cu-plating	Au	2.2

[1] Polished using 0.3μm Al_2O_3 slurry
[2] By 27μm Al_2O_3 particles
[3] By 180μm Al_2O_3 particles

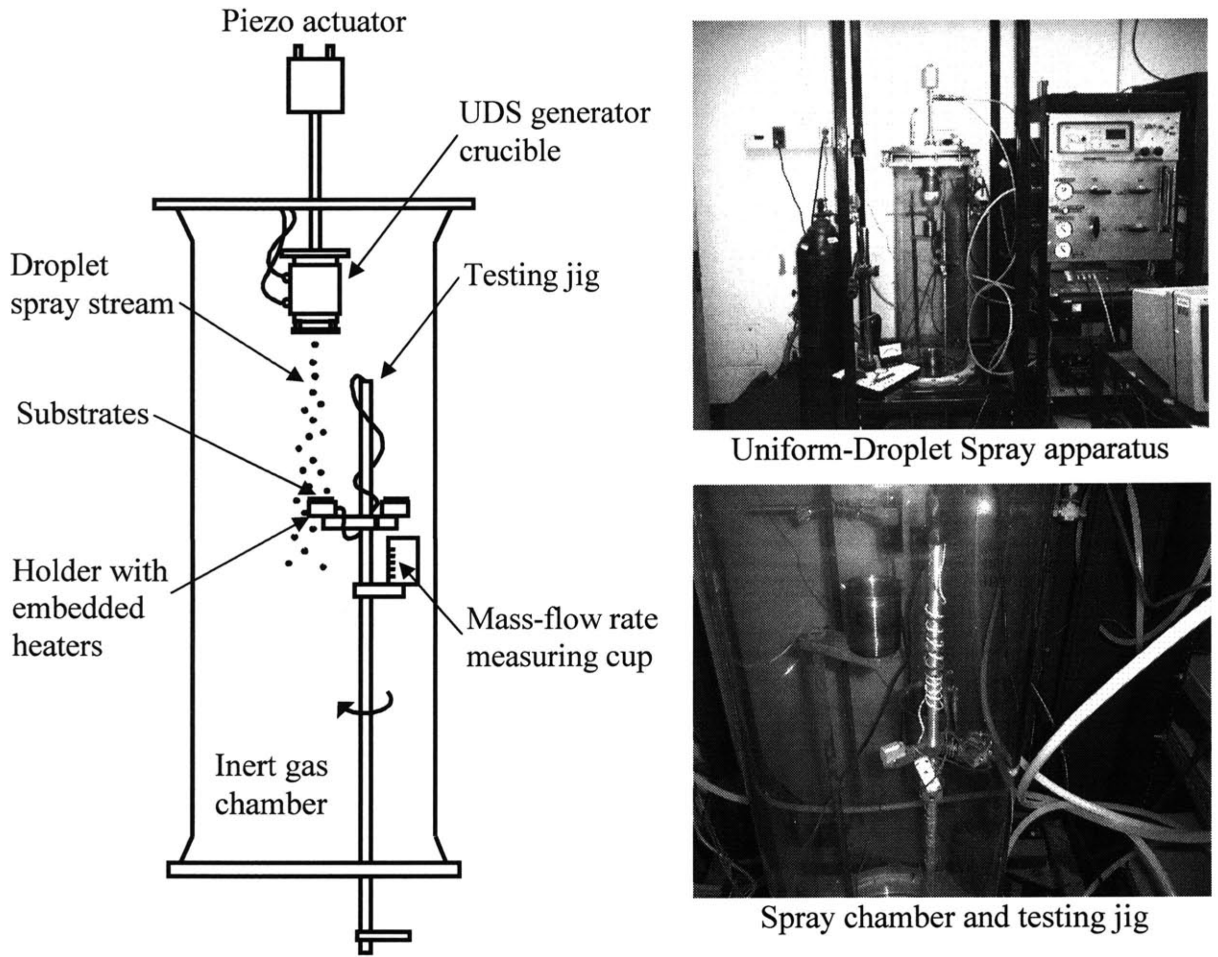

Uniform-Droplet Spray apparatus

Spray chamber and testing jig

Figure 3.4. Schematic and images of the apparatus for the droplet deposition experiments.

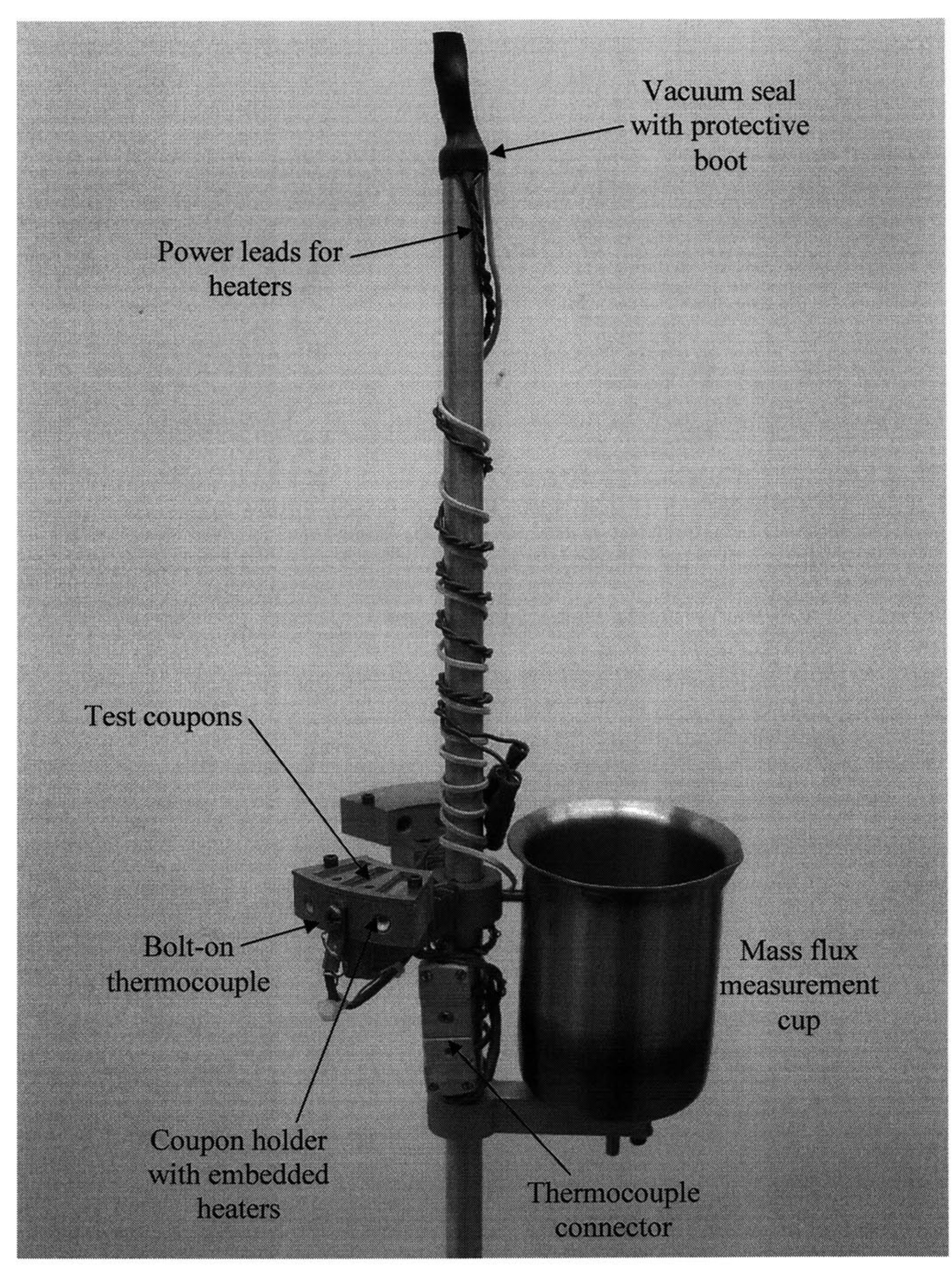

Figure 3.5. Details of the testing jig for the bump morphology study.

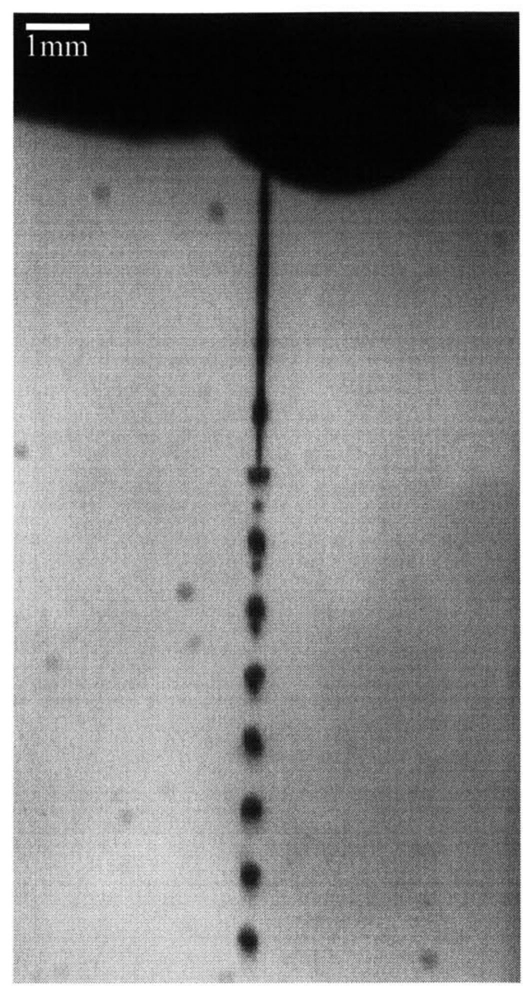

Figure 3.6. Break-up of the uniform –sized pure Sn droplets.

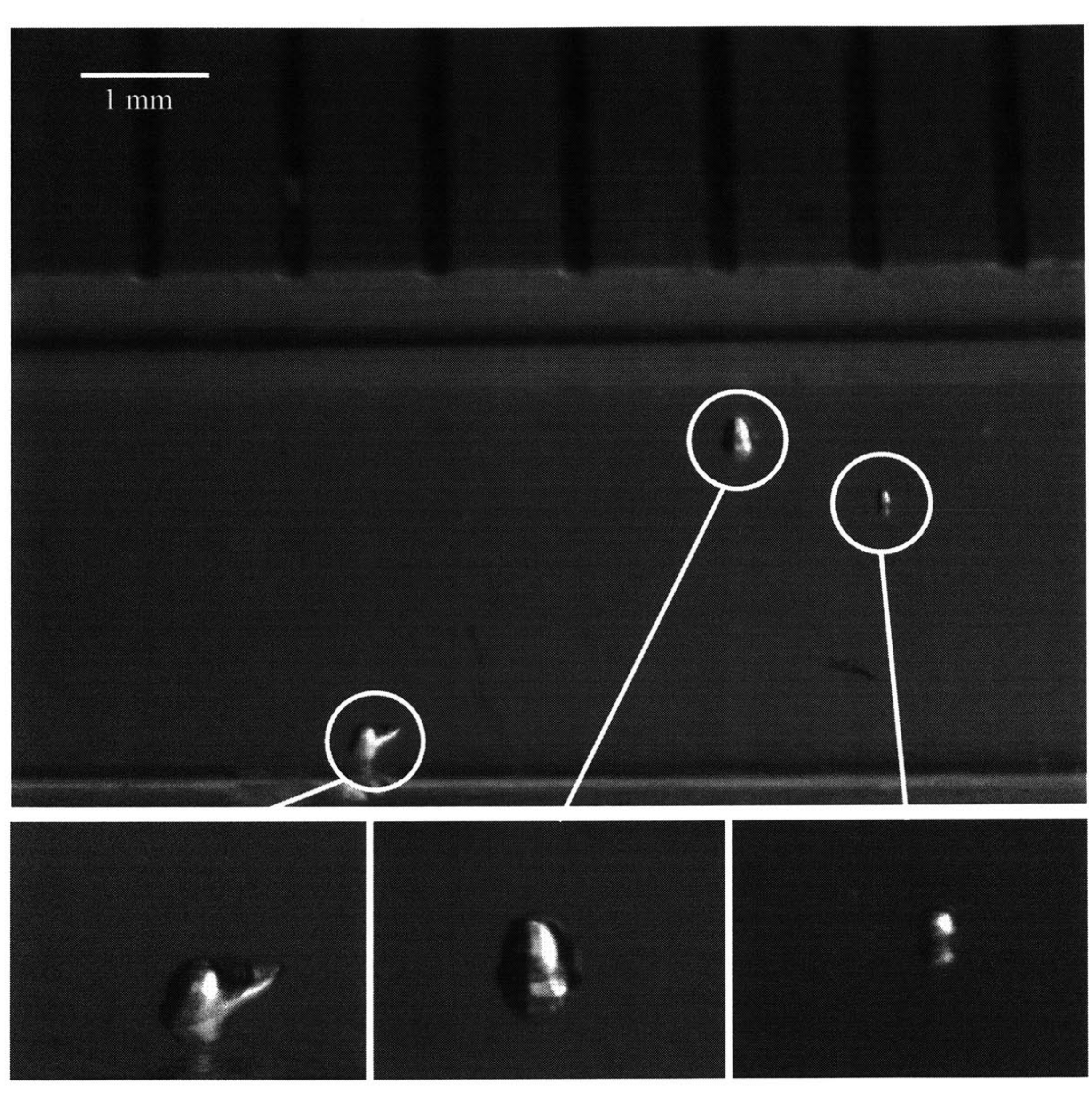

Figure 3.7(a). Morphologies of Sn bumps formed on polished Al surface.

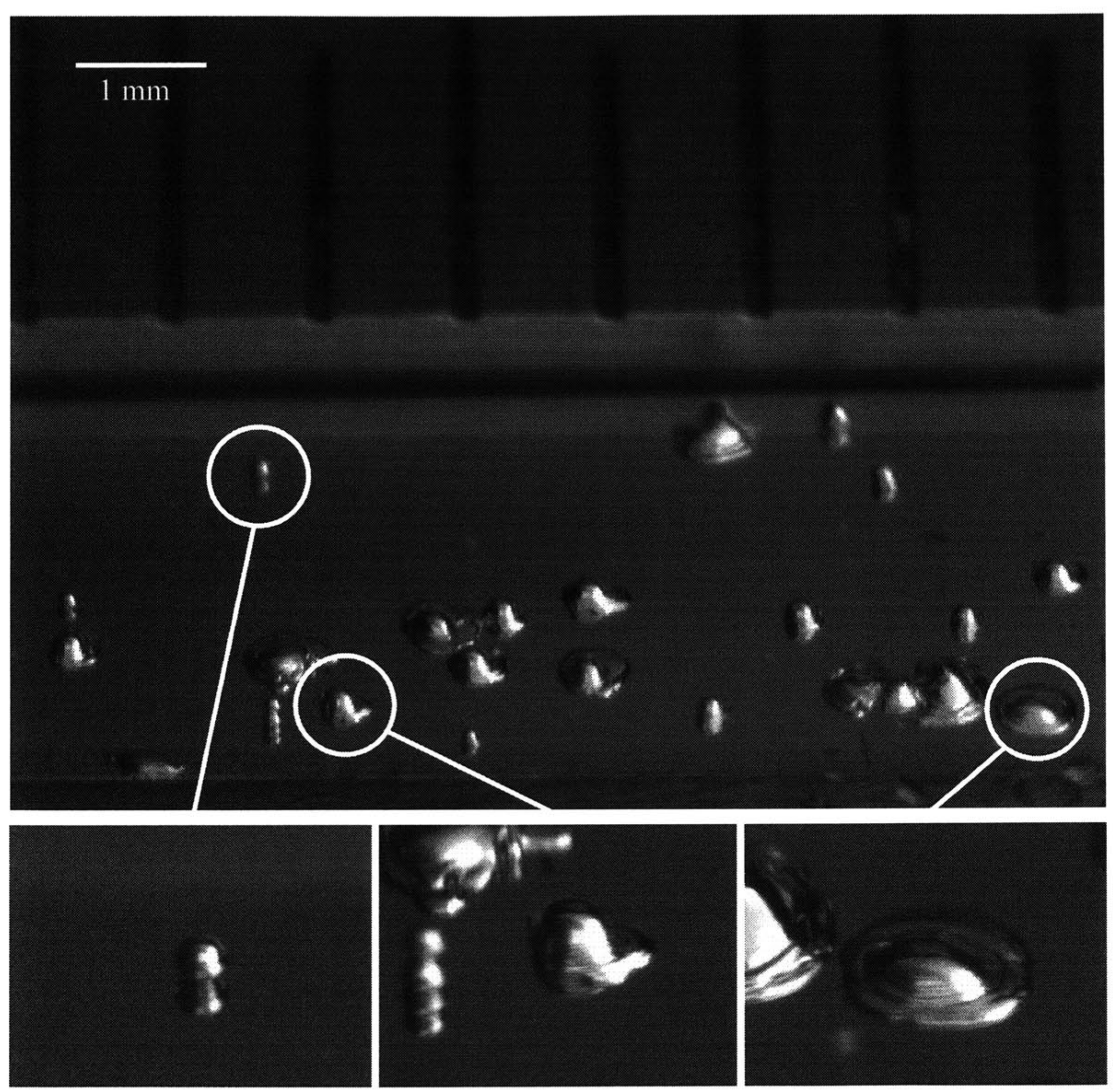

Figure 3.7(b). Morphologies of Sn bumps formed on polished Cu surface.

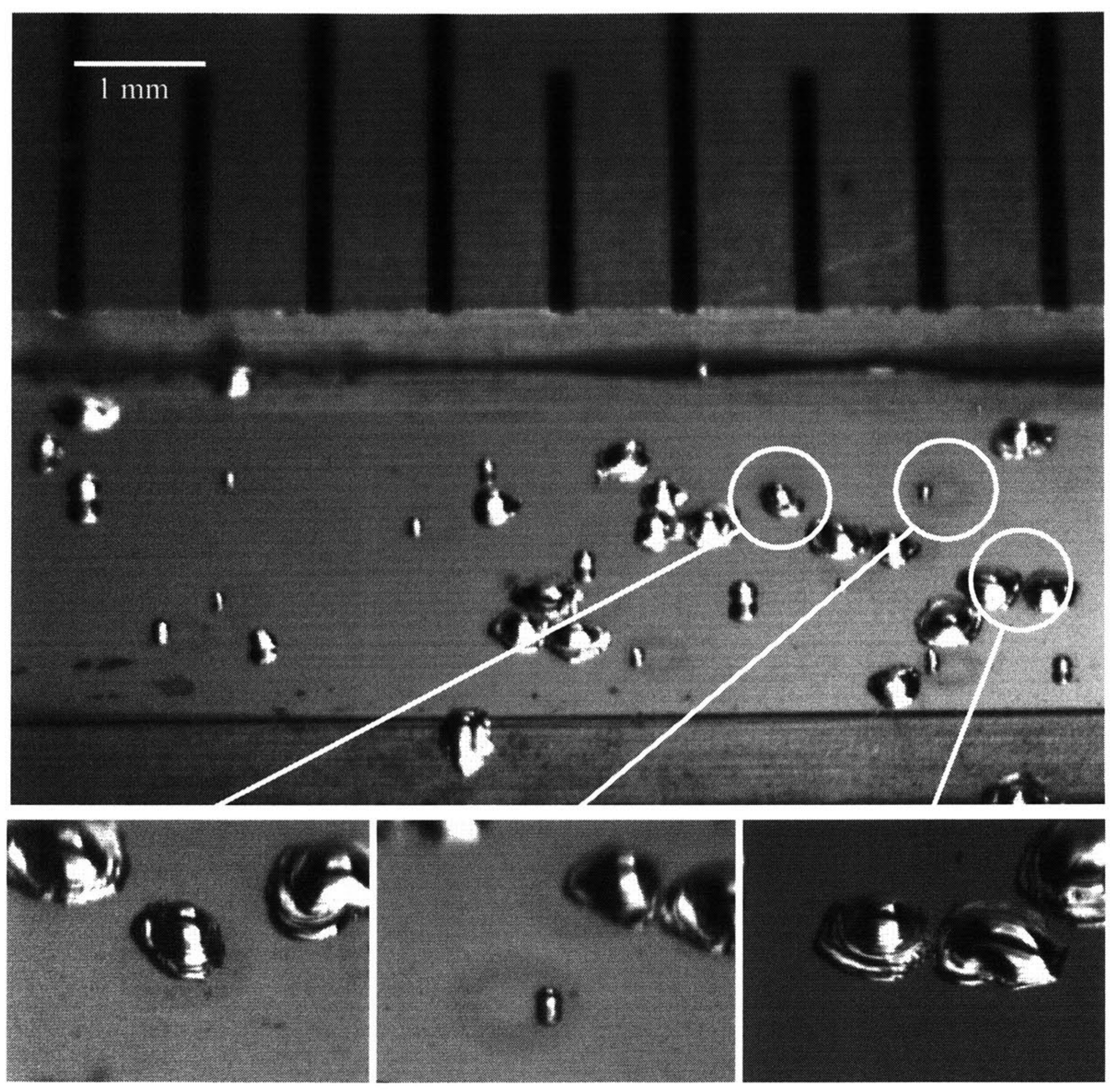

Figure 3.7(c). Morphologies of Sn bumps formed on Ni-P-plated surface.

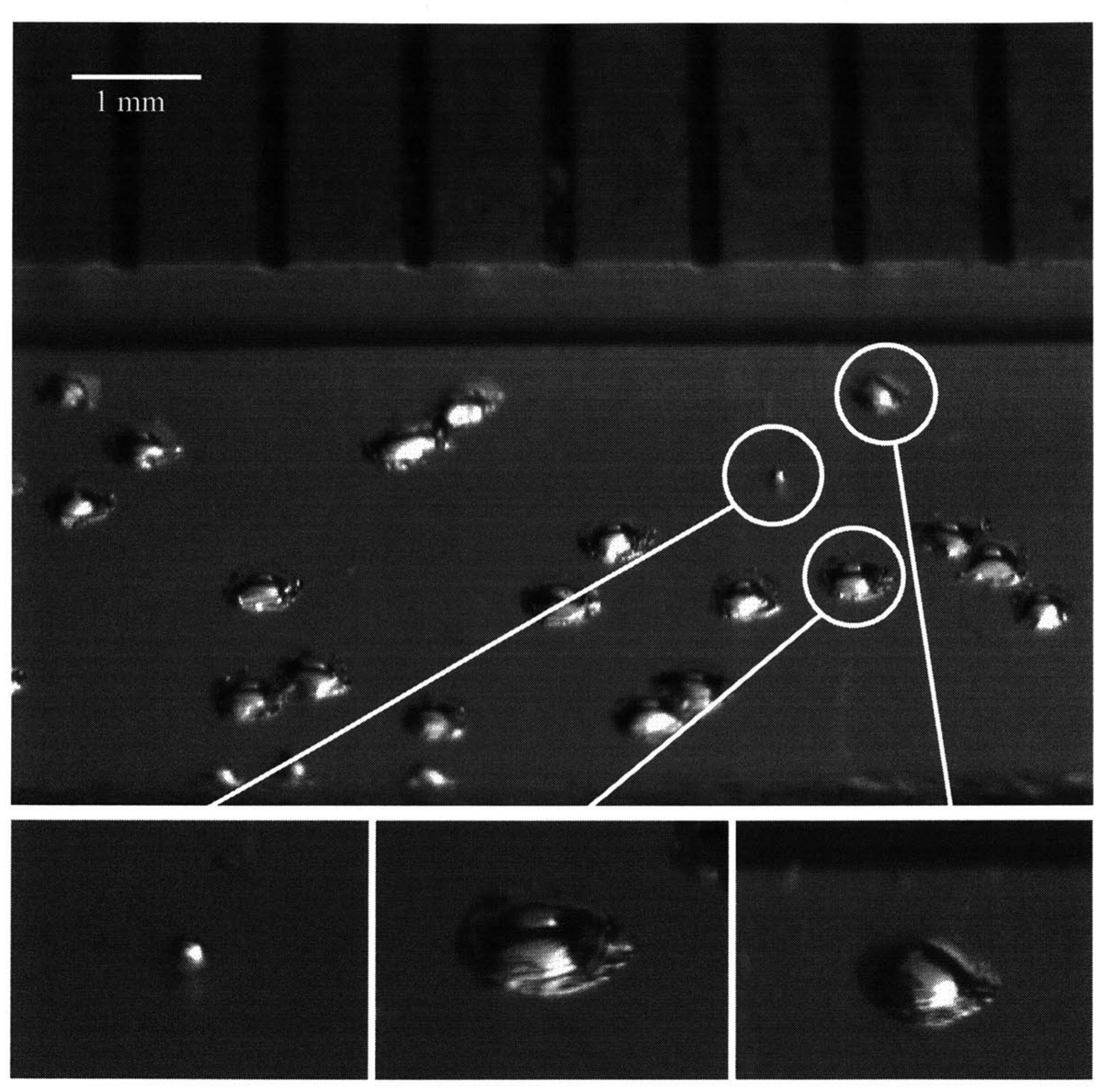

Figure 3.7(d). Morphologies of Sn bumps formed on Sn-plated surface.

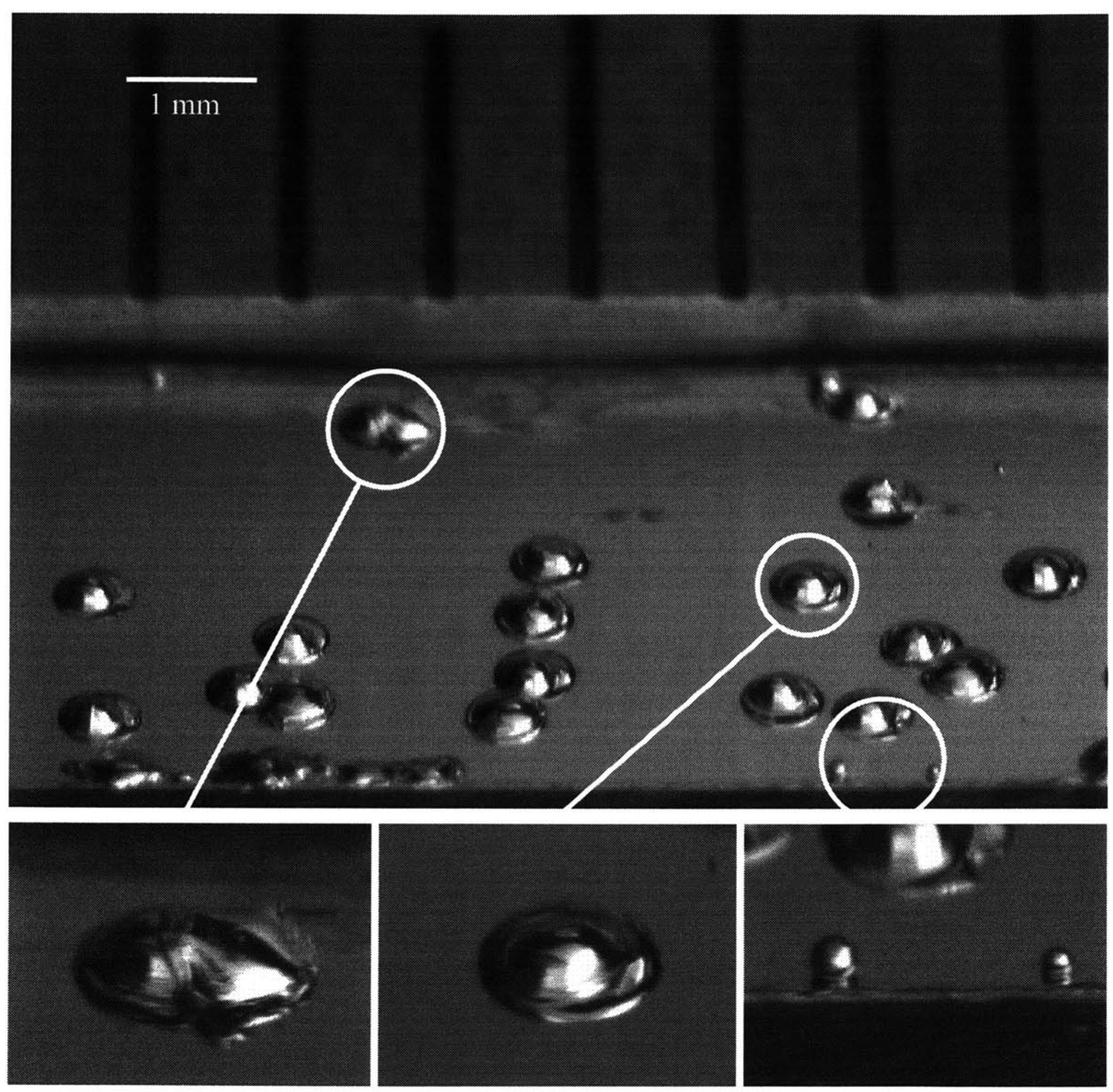

Figure 3.7(e). Morphologies of Sn bumps formed on Rh-plated surface.

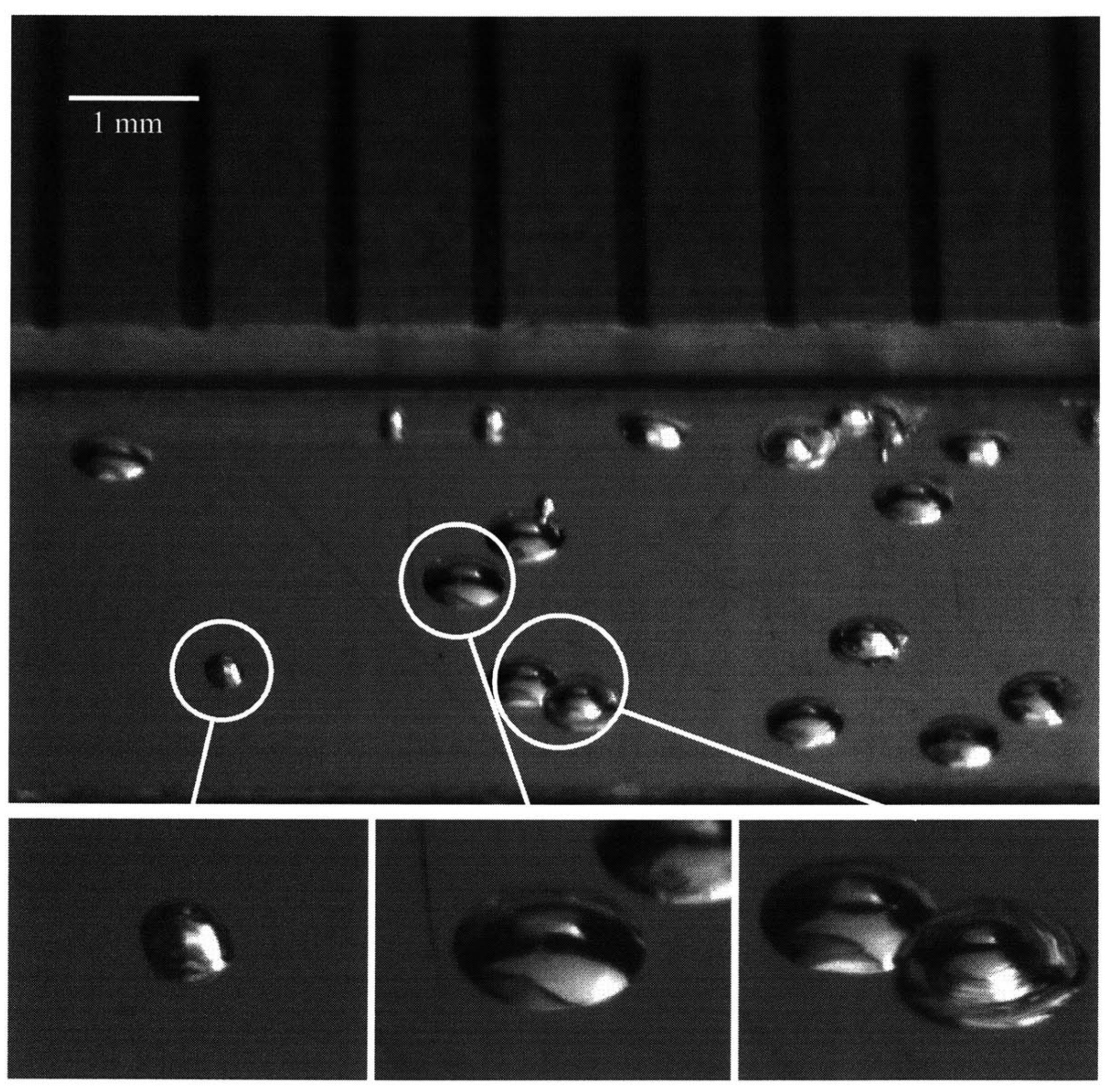

Figure 3.7(f). Morphologies of Sn bumps formed on Au-plated surface.

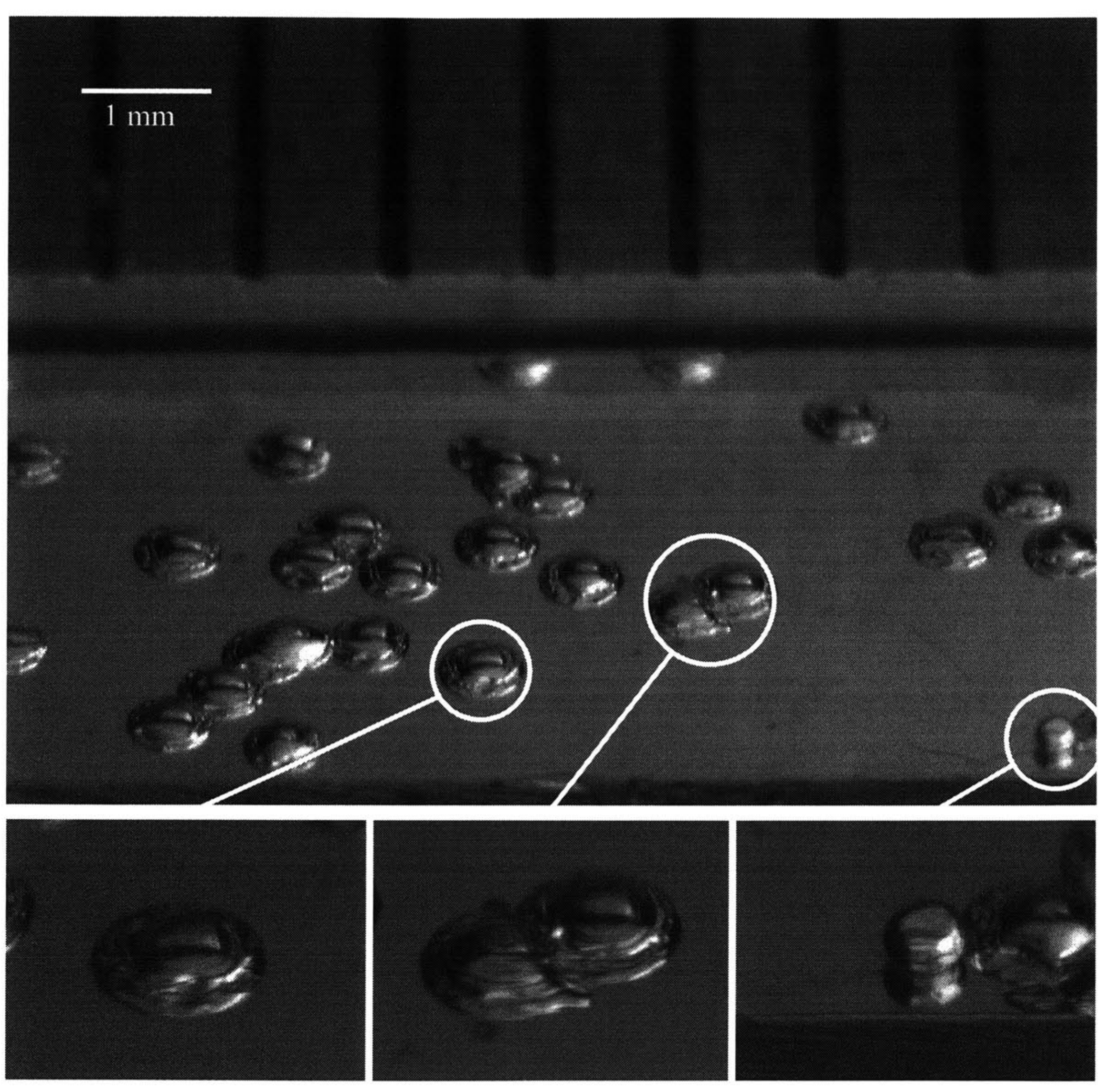

Figure 3.7(g). Morphologies of Sn bumps formed on Pd-plated surface.

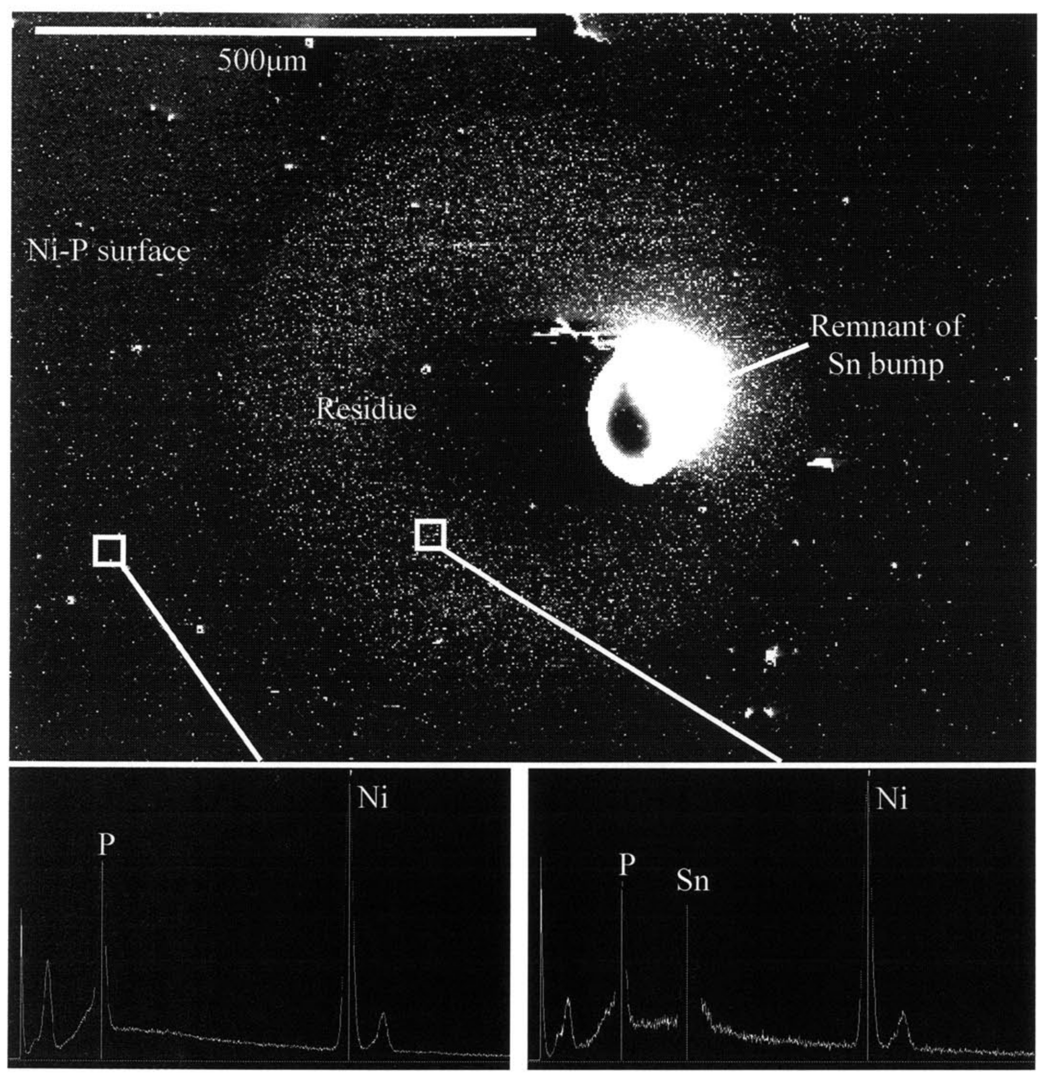

Figure 3.8. Remnant and residue of a Sn bump on Ni-P surface. EDS (energy dispersive spectrometry) traces show significant quantity of Sn in the residue region comparing to the surrounding area.

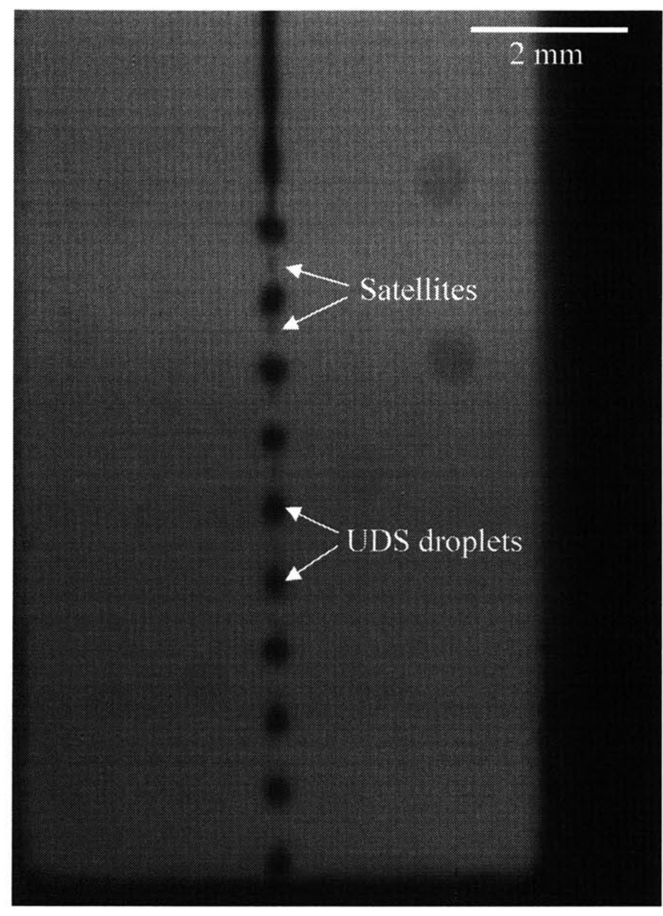

Figure 3.9. Formation of satellites in a UDS spray. Normal droplet size: 280μm. Satellite size: ~100μm.

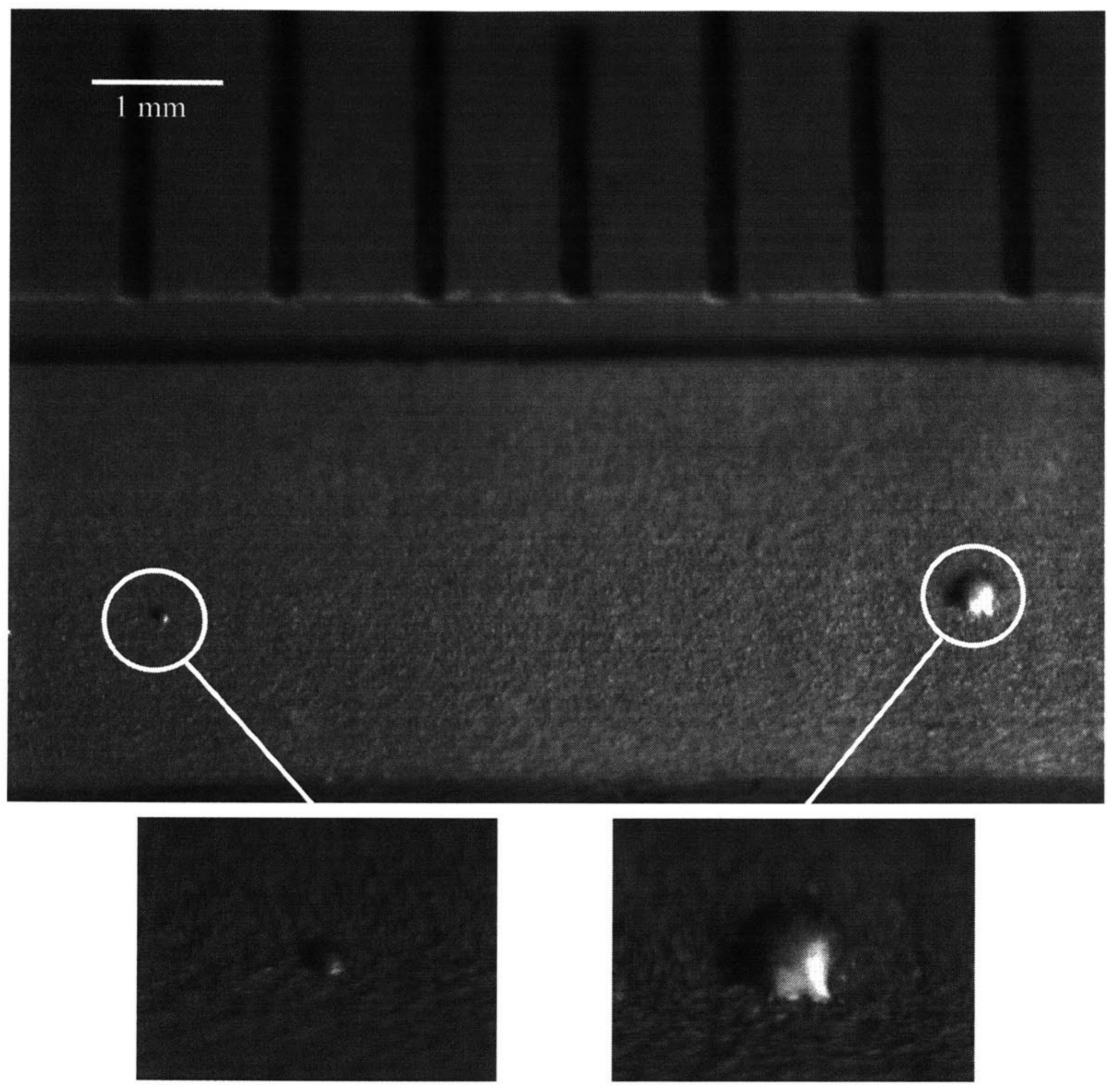

Figure 3.10(a). Morphologies of Sn bumps formed on Au-plated, 180μm Al_2O_3 sandblasted surface.

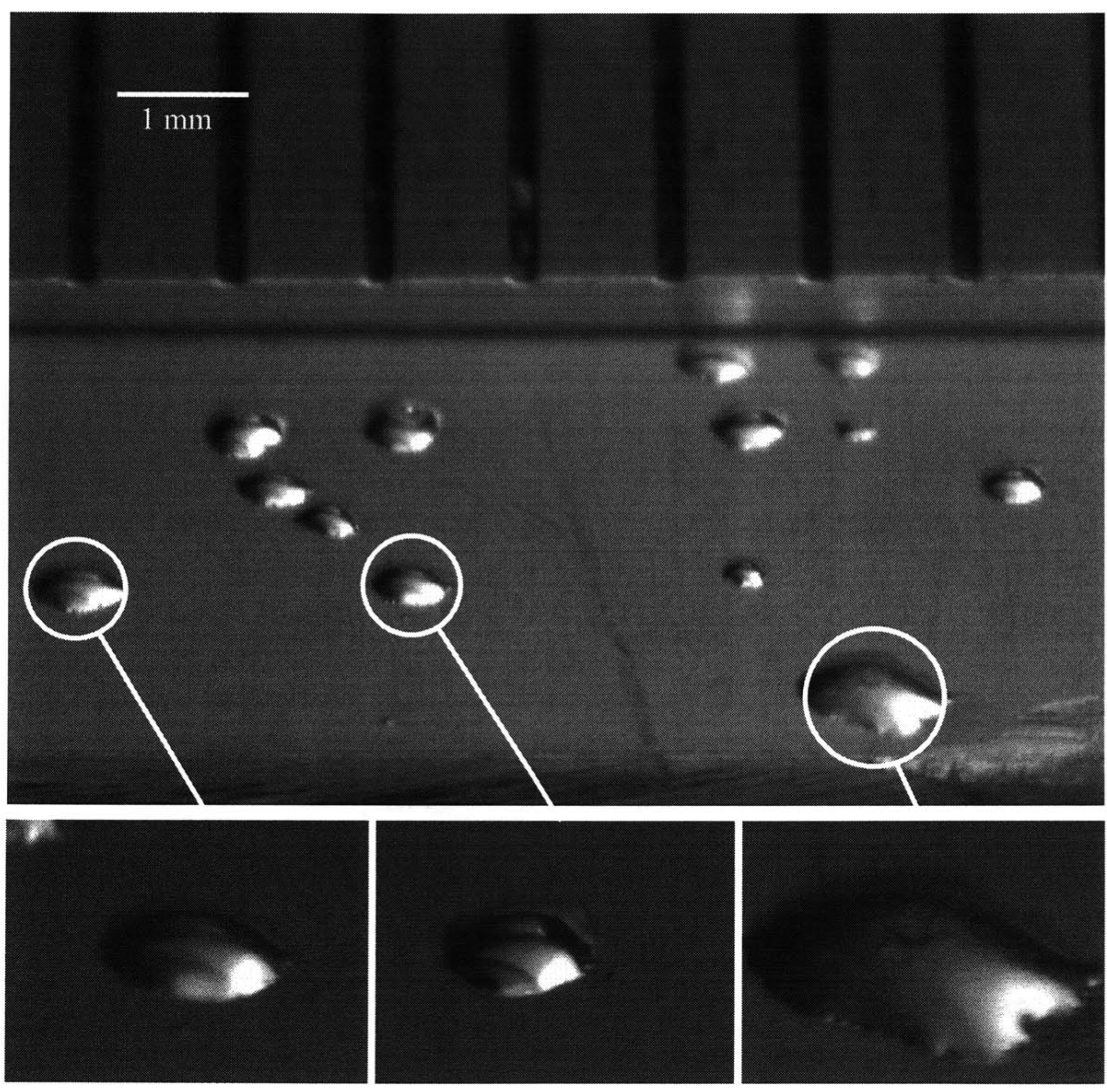

Figure 3.10(b). Morphologies of Sn bumps formed on Au-plated, 27μm Al_2O_3 sandblasted surface.

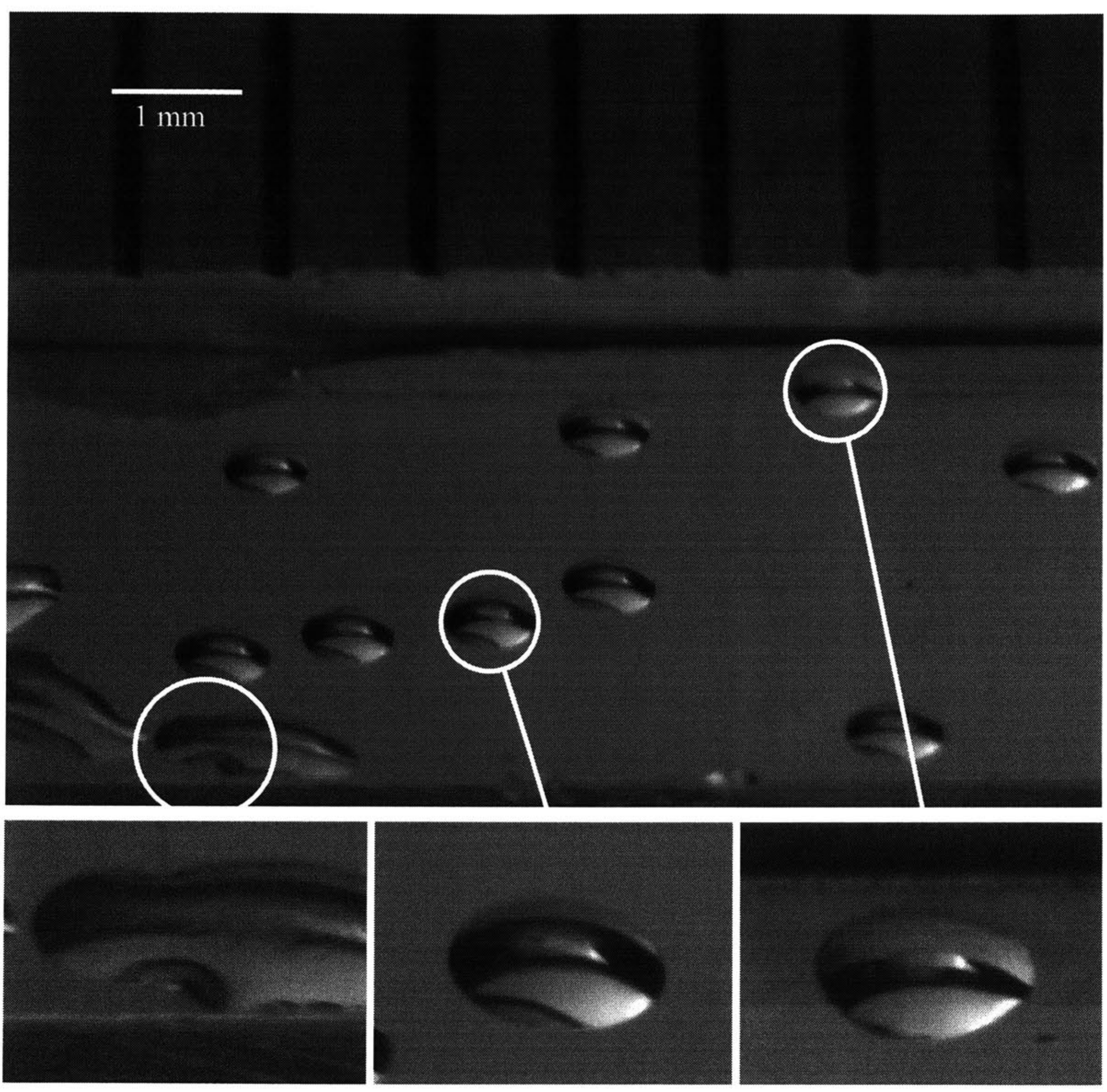

Figure 3.10(c). Morphologies of Sn bumps formed on Au-plated, 0.3μm Al_2O_3 slurry polished surface.

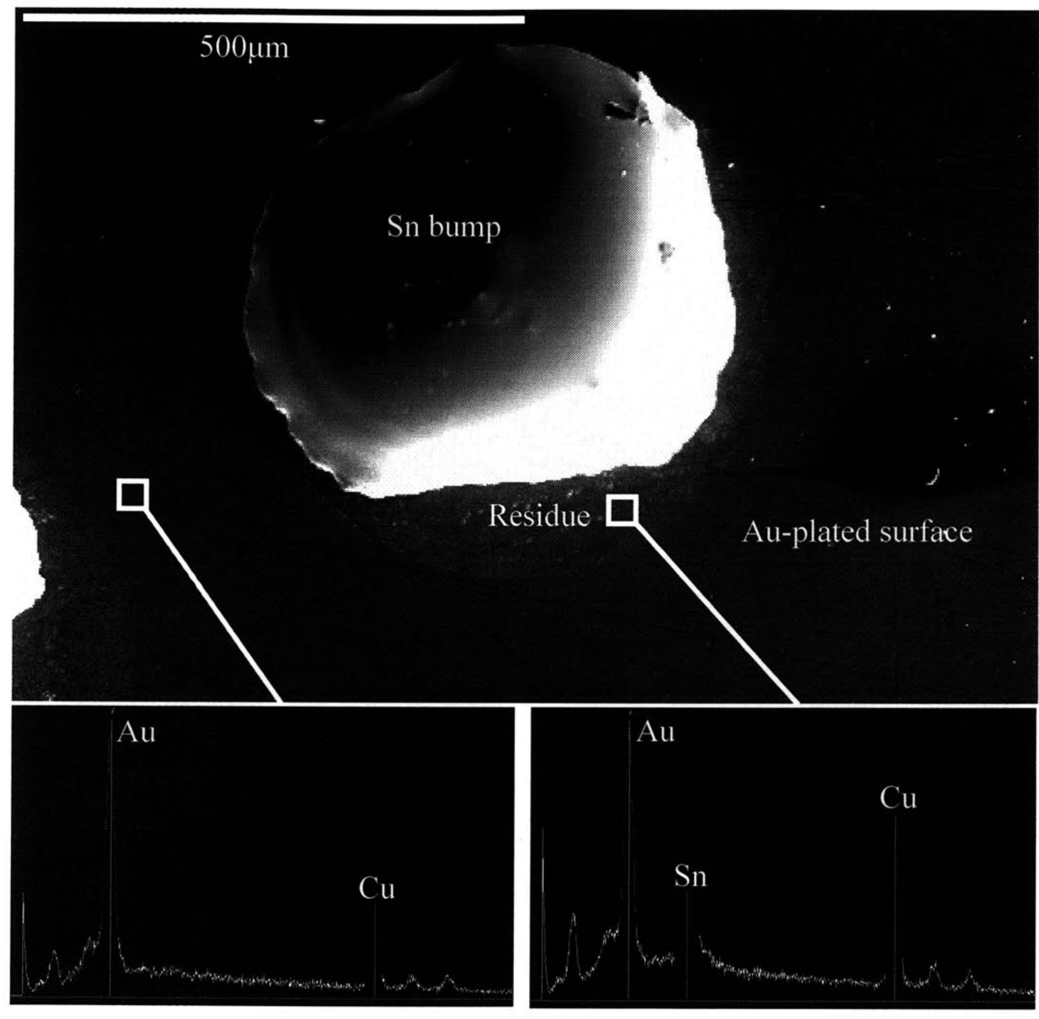

Figure 3.11. Residue next to a Sn bump on Au-plated, 27μm Al_2O_3 sandblasted surface. EDS (energy dispersive spectrometry) traces show significant quantity of Sn in the residue region comparing to the surrounding area.

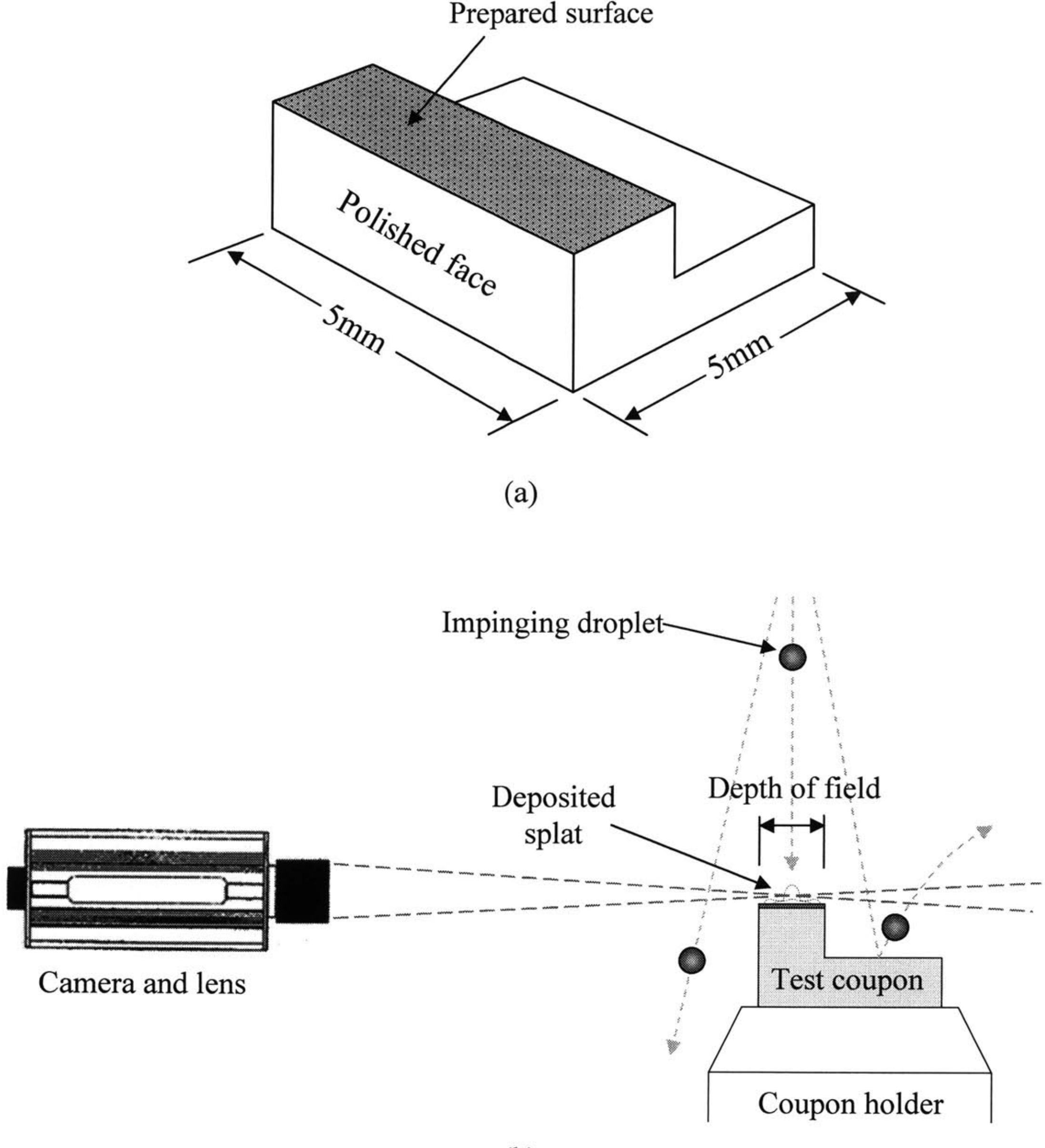

Figure 3.12. Schematics of (a) the test coupon and (b) the optical set-up of the high-speed imaging experiments.

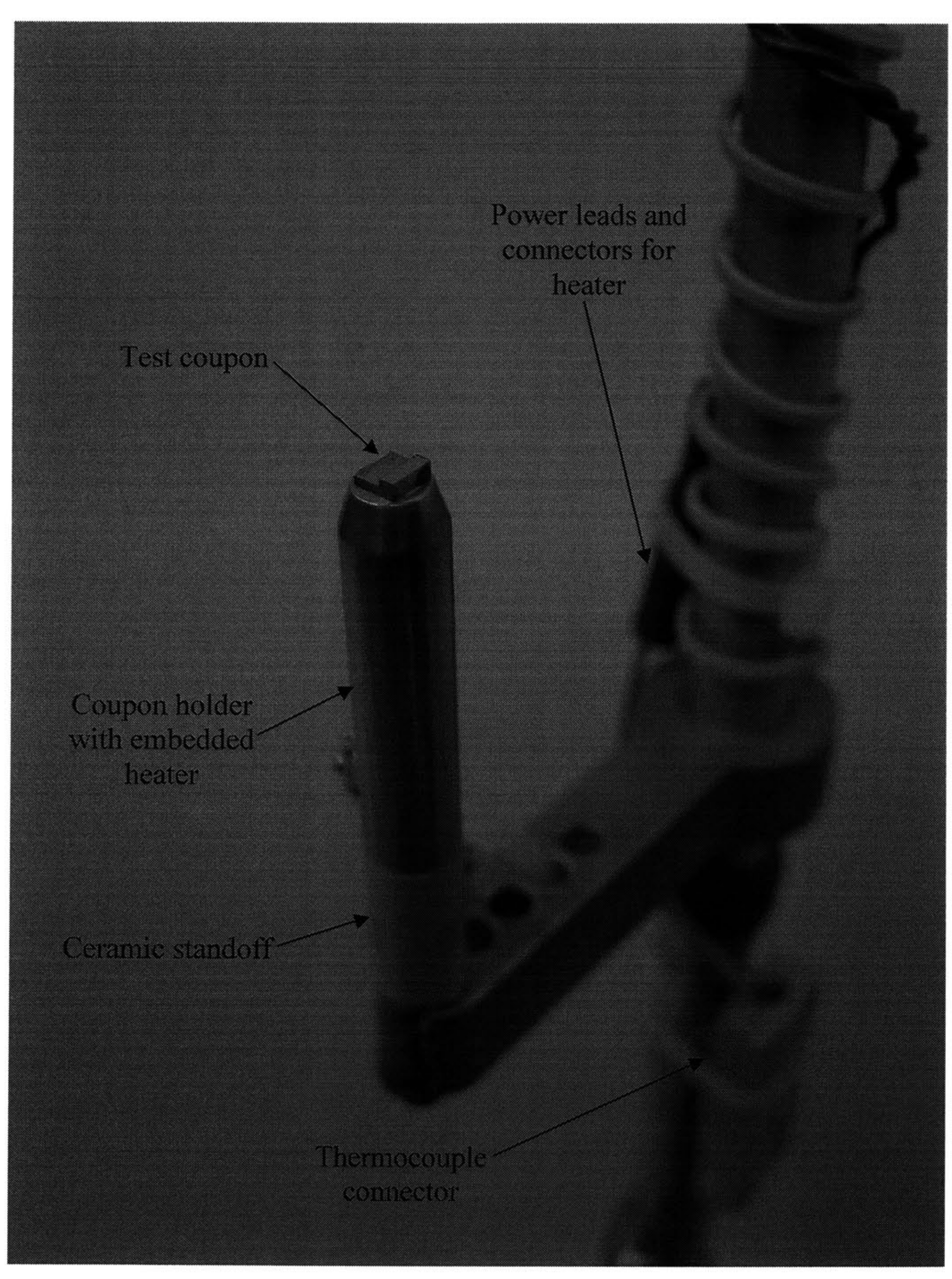

Figure 3.13. Details of the testing jig for the high-speed imaging experiments.

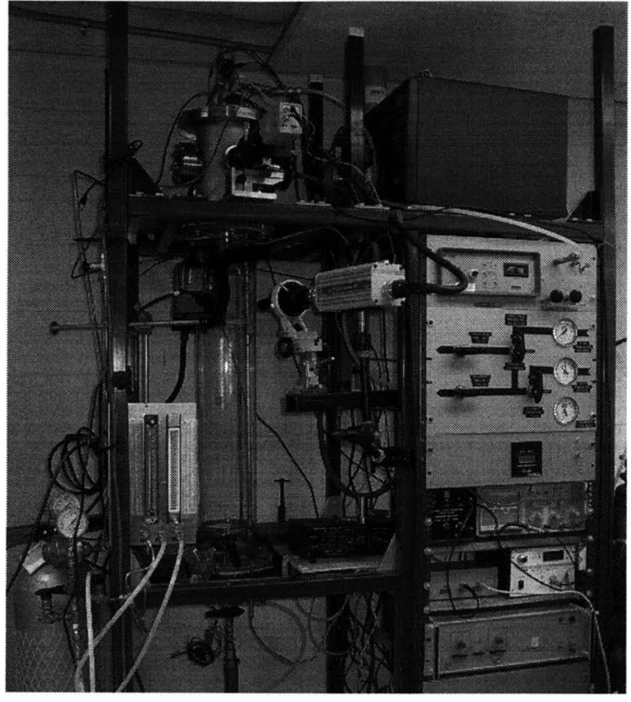

High-speed imaging set-up

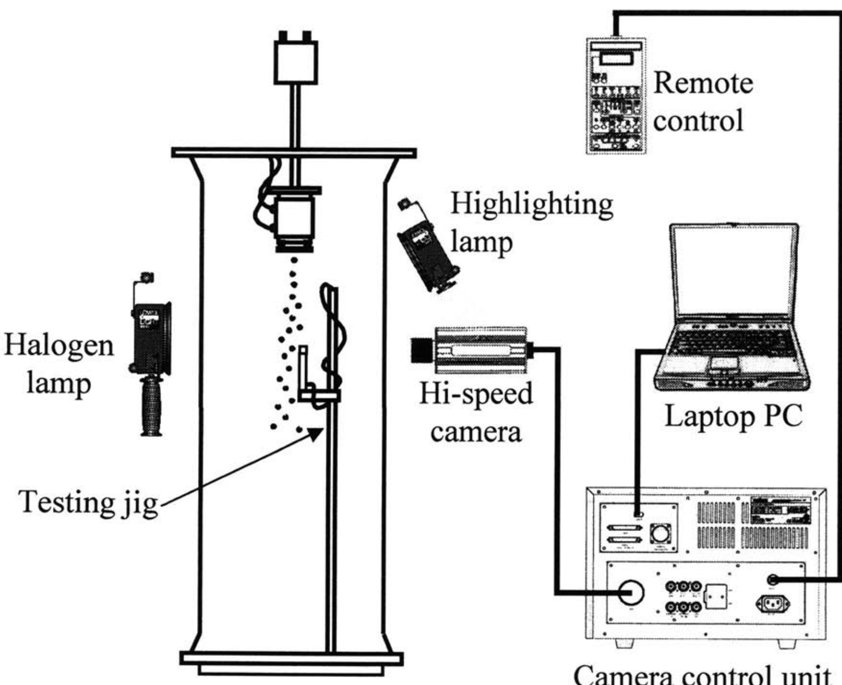

Figure 3.14. Schematic and image of the apparatus for the high-speed imaging study.

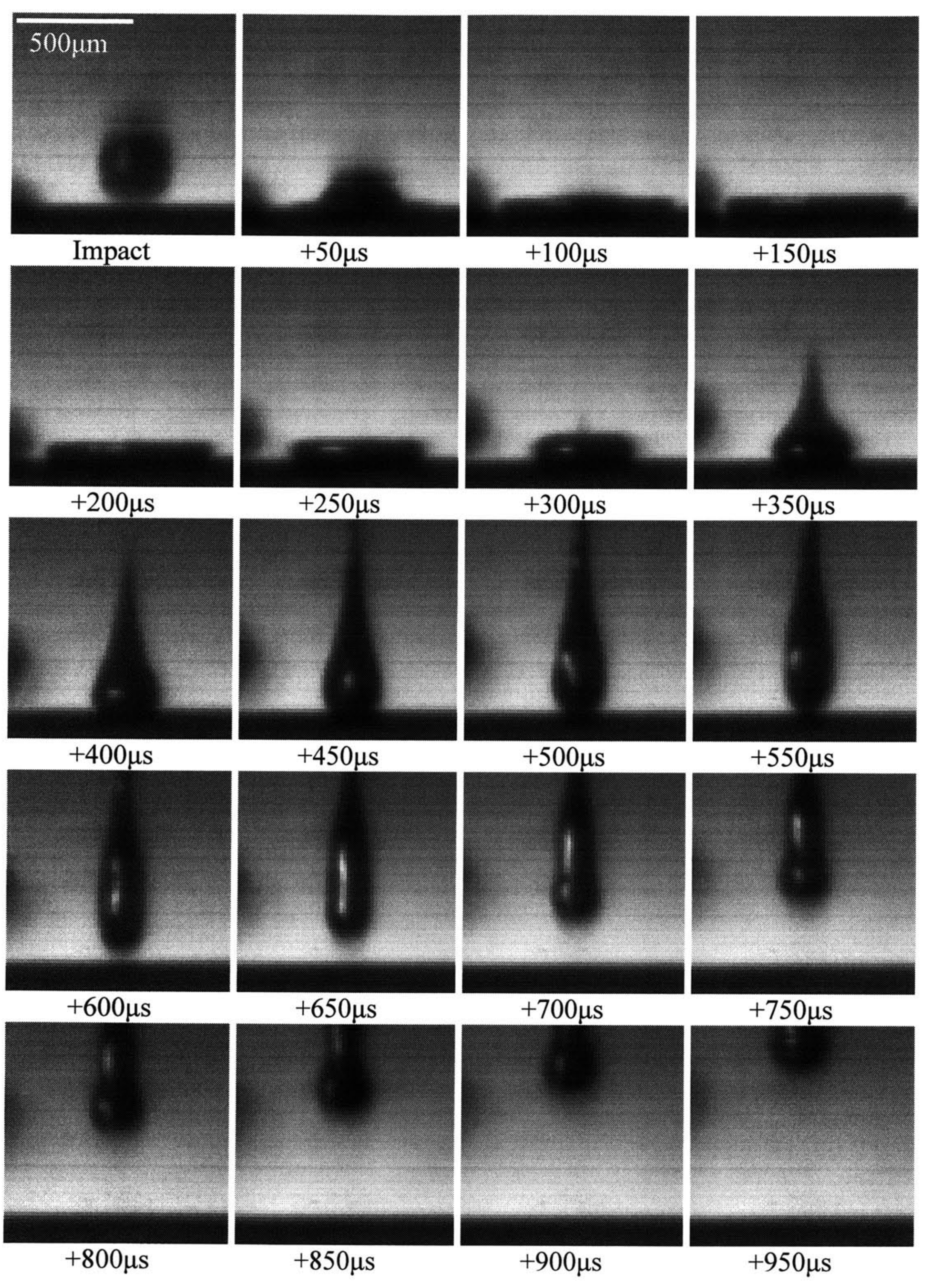

Figure 3.15(a). Droplet exhibits bouncing behavior on Sn (oxide)-plated surface. Droplet: Pb-37wt% Sn solder, D_{ini} = 283μm, u_{ini} = 3.8m/s.

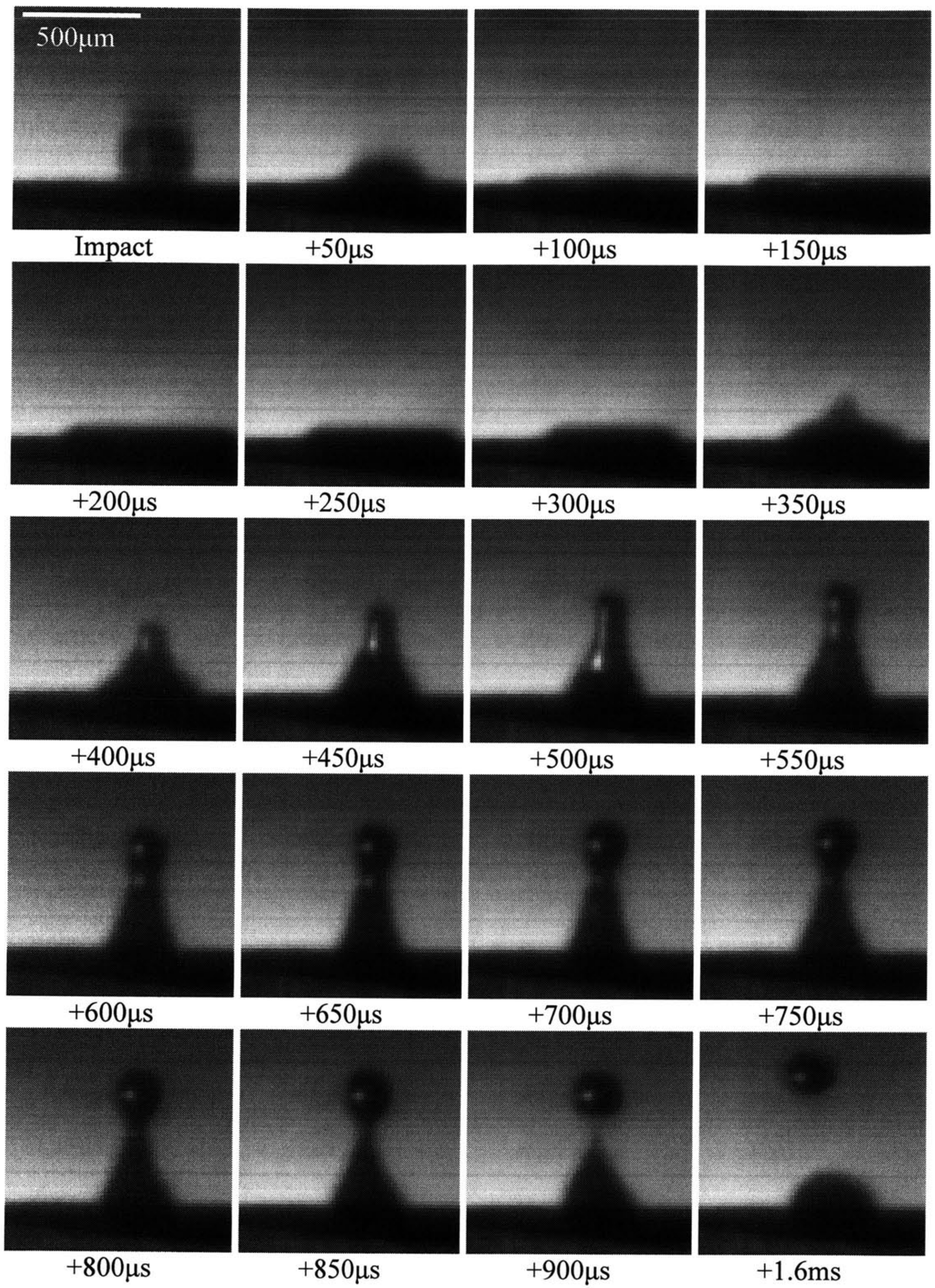

Figure 3.15(b). Droplet exhibits partial bouncing behavior on Rh-plated surface. Droplet: Pb-37wt% Sn solder, D_{ini} = 287μm, u_{ini} = 3.9m/s.

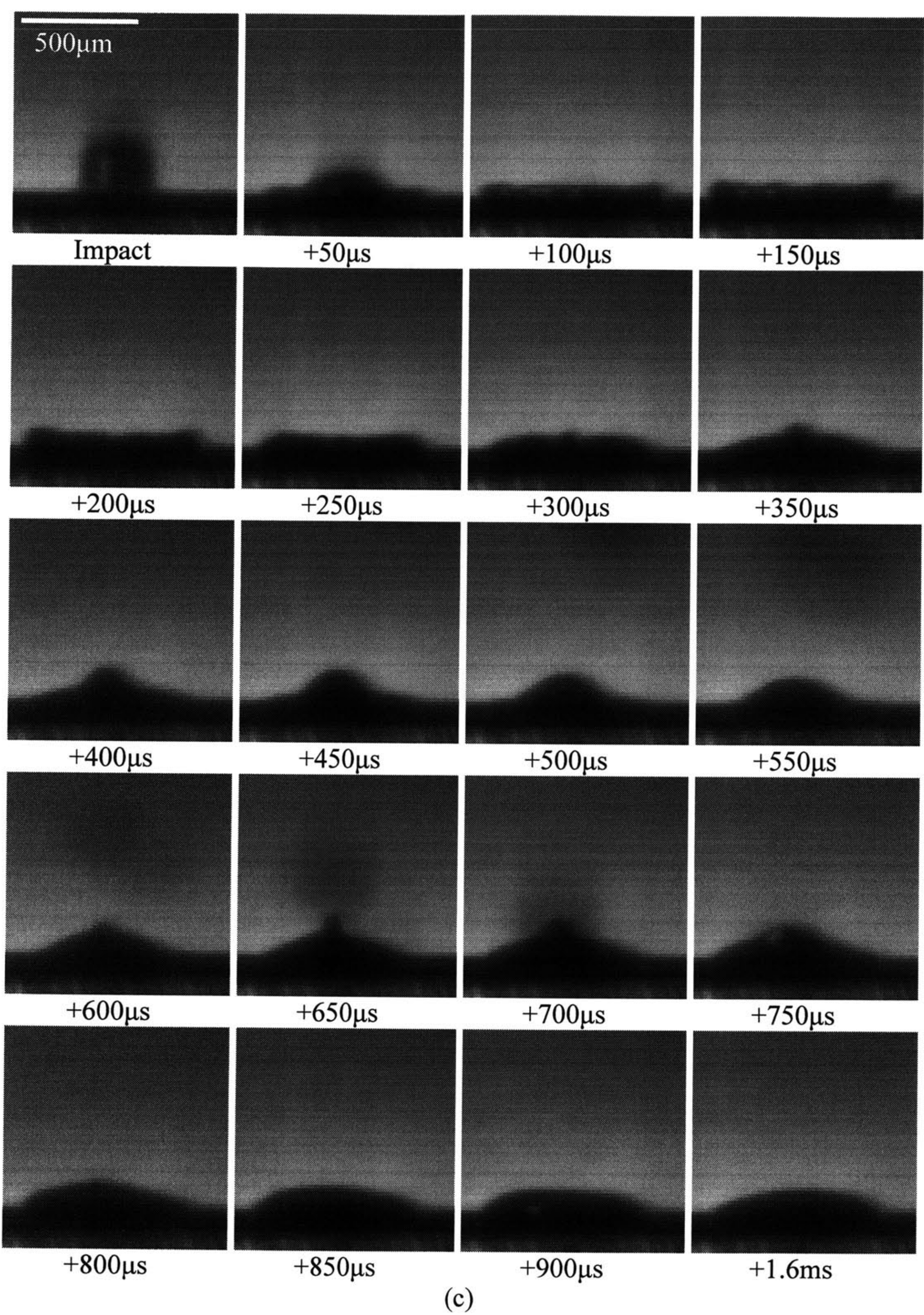

Figure 3.15(c). Droplet exhibits sticking behavior on Pd-plated surface. Droplet: Pb-37wt% Sn solder, D_{ini} = 287μm, u_{ini} = 3.6m/s.

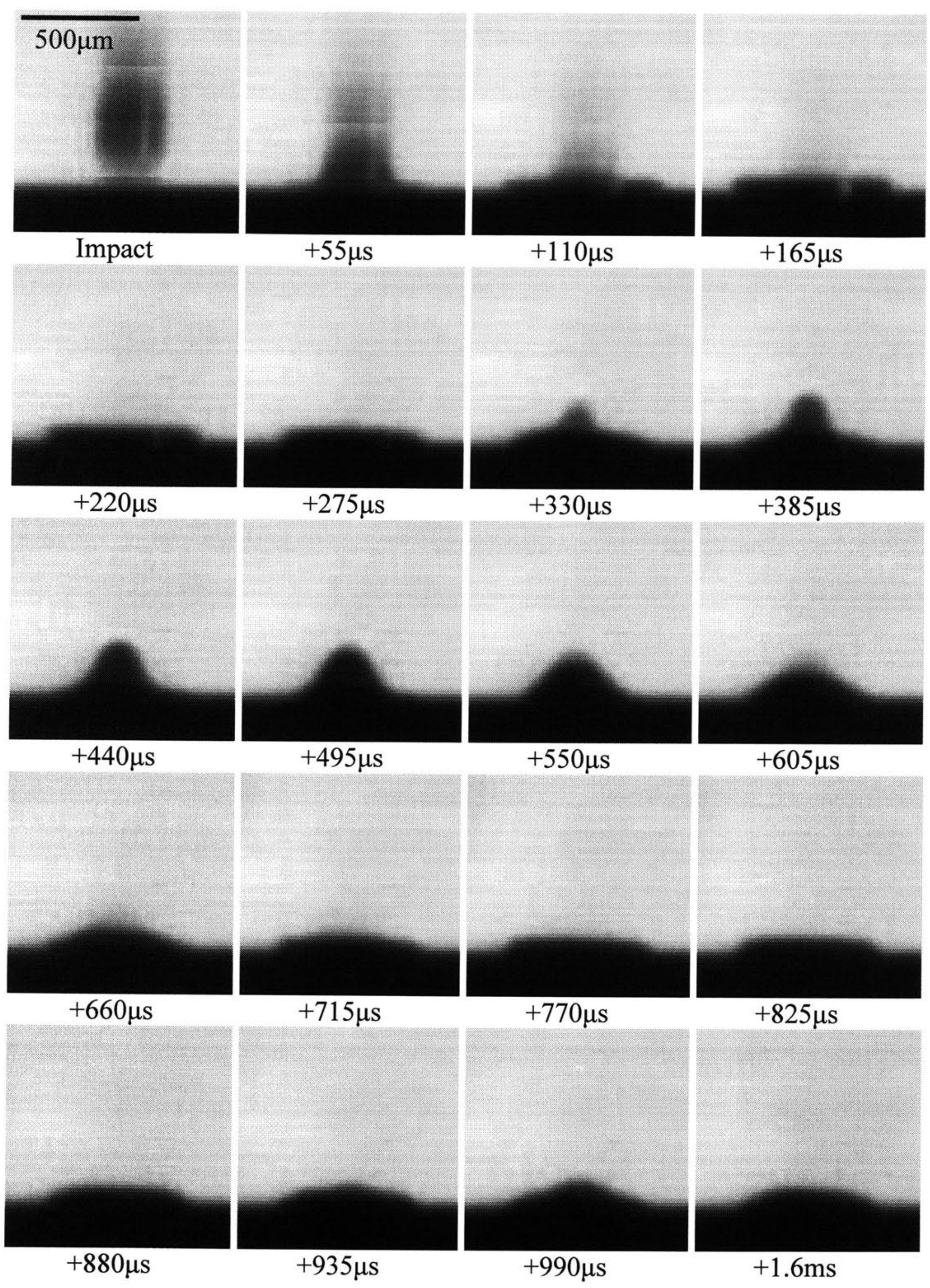

Figure 3.16(a). Droplet exhibits sticking behavior on Au-plated, 0.3μm Al_2O_3 slurry polished surface. Droplet: Pb-37wt% Sn solder, D_{ini} = 275μm, u_{ini} = 4m/s.

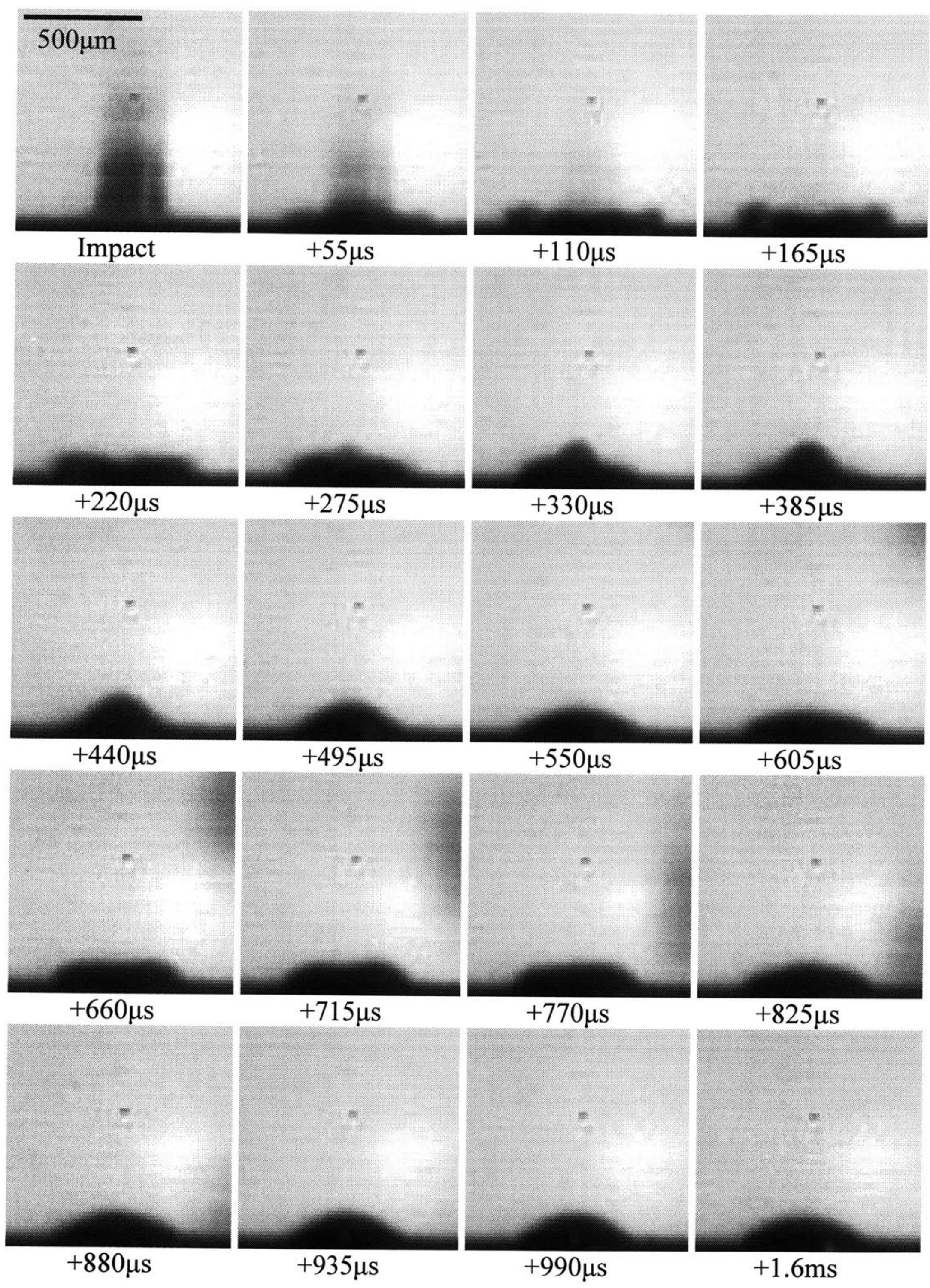

Figure 3.16(b). Droplet exhibits sticking behavior on Au-plated, 27μm Al_2O_3 sandblasted surface. Droplet: Pb-37wt% Sn solder, D_{ini} = 273μm, u_{ini} = 3.9m/s.

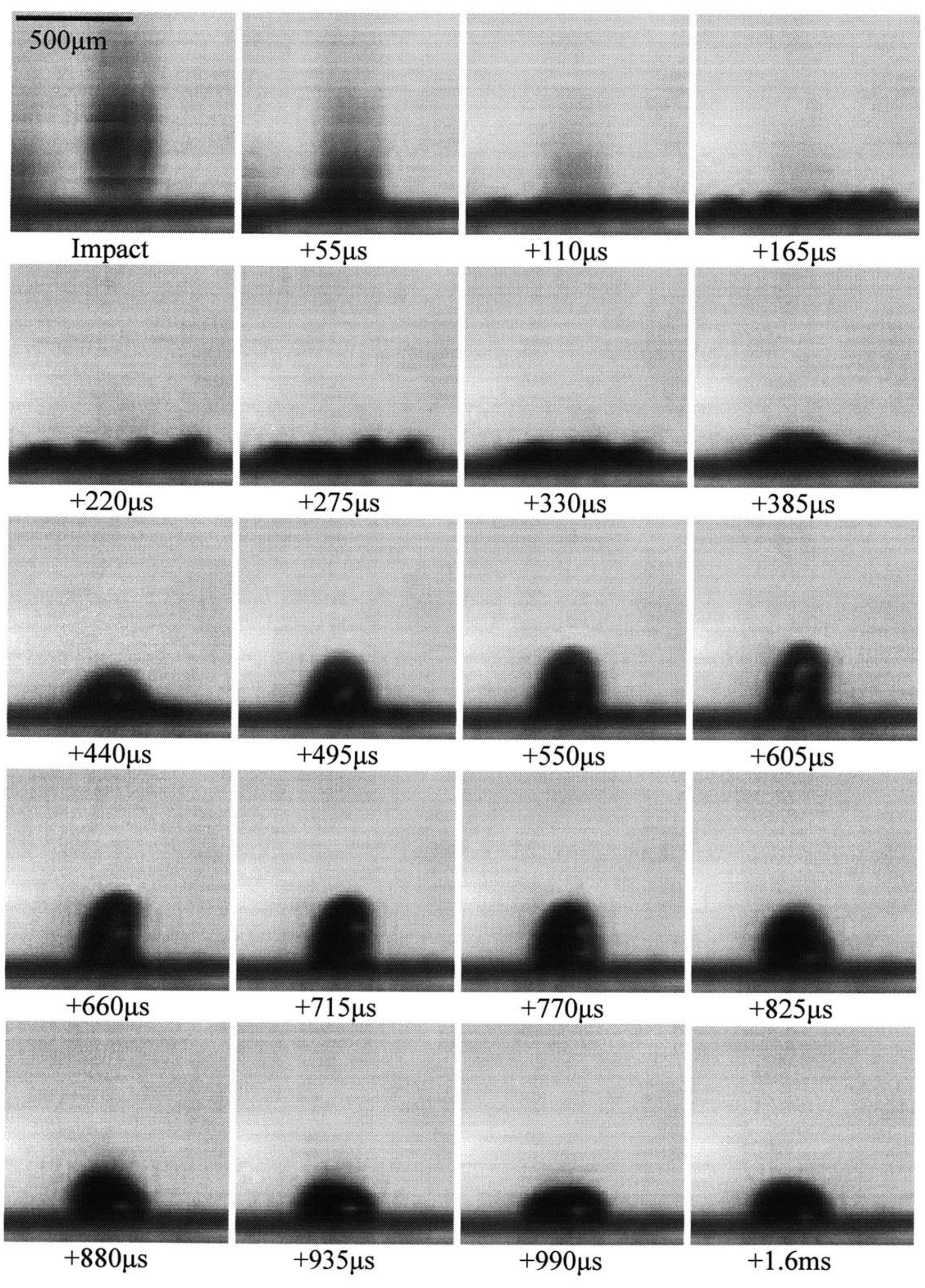

Figure 3.16(c). Droplet exhibits necking behavior on Au-plated, 180μm Al_2O_3 sandblasted surface. Droplet: Pb-37wt% Sn solder, D_{ini} = 280μm, u_{ini} = 4m/s.

CHAPTER 4. MODEL VALIDATION AND DISCUSSION

4.1 Introduction

According to the analytical models described in Chapter 2, the potential for the deposited droplets to bounce is expected to increase as either the melt-surface wetting deteriorates or the target surface roughness increases. The effects of these surface properties on the droplet bouncing behavior have also been qualitatively confirmed by the experimental observations made in Chapter 3. In the present chapter, the experimental results are analyzed quantitatively to verify the concepts and assumptions made in the analytical work.

The basic concepts described in Chapter 2 are reviewed as follows. The effect of the droplet-surface wetting on bouncing has been developed by investigating the energy states of a deforming droplet during its post-impact, spreading and recoiling processes on a solid surface. The oscillating motions of a droplet are dictated by two principles: minimization of the surface free energy and conservation of energy.

A liquid droplet on a rigid, unchangeable solid will tend to assume a configuration that minimizes its surface free energy, if it is not subjected to unbalanced external influences [Gibbs, 1906; Harkins, 1952]. A droplet deposited gently on a solid surface will spread until its interfaces with the surrounding atmosphere and the solid underneath reach a state such that its total free energy is minimized. The spreading ceases when this state, also known as the equilibrium state, is reached. On the other hand, when a droplet is deposited and spread in the inviscid, impact-driven regime [Schiaffino and Sonin, 1997], as in the case of direct droplet deposition bumping, the impact pressure forces the deposited droplet to spread to a non-equilibrium configuration with surface free energy greater than its equilibrium counterpart. The tendency to minimize the surface free energy then dictates the deformed droplet to recoil after the initial spreading and return to its equilibrium, minimal energy configuration.

Based on the principle of conservation of energy, droplet recoiling may be viewed as a conversion of the energy differences, between a droplet at maximum spreading and in equilibrium, to kinetic fluid motions. Since the droplet is momentarily at rest at maximum spreading and sessile in equilibrium, its energy at either state may be estimated solely by its surface energy. Therefore, the difference between droplet surface energies at these two states may be regarded as the potential that drives the recoiling motions. Since droplet bouncing is assumed to be a result of severe droplet recoiling, the magnitude of this differential surface energy may be used to evaluate the tendency for a deposited droplet to bounce. Consequently, the normalized differential surface energy is proposed as a bouncing criterion. Furthermore, given that the surface energy of a deposited droplet is a function of the specific droplet-surface wetting condition, droplets deposited under different wetting conditions are expected to exhibit variations in their tendencies to rebound. Specifically, deterioration of the droplet-surface wetting is suggested to induce droplet bouncing.

The effect of surface roughness on bouncing is represented by its impact on the transient wetting during droplet deposition. The dynamic interface between a post-impact, deforming droplet and a rough surface is likely to be populated by gas pockets trapped within the surface defects. The resultant interfacial voids prevent the deposited droplet from wetting the surface completely. The consequent incomplete wetting alters the net melt-solid interfacial energy, and hence affects the potential for droplet bouncing. The roughness-induced incomplete wetting is quantified by the effective contact area fraction, the ratio between the actual melt-surface contact area and the total area of a rough surface. The effective area fraction is shown to be proportional to the extent of the penetration of the deposited melt into the surface defects.

Characterizing an actual defect on a rough surface as a conical notch, the melt penetration may be determined analytically by balancing the impact pressure and capillary forces that drive the penetration against the resistance from the compression of the trapped gas. The roughness-induced incomplete wetting may then be quantified by using the resultant area fraction to calculate the adjusted contact angle. The analyses presented in Chapter 2 show that melt penetration, and hence the extent of the incomplete wetting, is a strong function of the characteristic defect geometry. Based on the assumption that greater surface roughness is characterized by a decrease of the defect wall angle, the analysis concludes that increases in the

surface roughness may promote incomplete wetting, and hence increase the potential for droplet bouncing.

These modeling concepts will be examined first in the present chapter. The geometrical evolution of droplets deposited on different substrate surfaces will be extrapolated from the high-speed images obtained from the experimental study. The associated surface energy states will be determined based on the specific droplet-surface wetting conditions. Positive correlations between deteriorations of the wetting conditions to increases in the maximum differential surface energies will act as a validation of the wetting effect concept. The concept behind the surface roughness effect is verified by first characterizing the roughened test surfaces using an optical profilometer. By examining the 3-D profiles of the surfaces with different roughness levels, the assumed correlation between the defect geometry and surface roughness level is verified. The interactions between the deposited droplets and the roughened test surfaces are simulated by representing the actual surfaces using the proposed surface model and approximating the extents of melt penetration and the associated effective area fraction based on the deposition conditions. The effect of surface roughness on the overall droplet-surface wetting condition is quantified by calculating the adjusted contact angles. The analytically determined angles are then compared with the measured values obtained from images of sessile solder drops on the roughened surfaces. Agreements between the analytical estimates and the empirical measurements verify the surface modeling and the effect of surface roughness on wetting condition during droplet deposition.

After the concepts and assumptions associated with the effects of wetting and surface roughness on bouncing are verified, the potentials of bouncing for droplets deposited in the experimental study are quantified by calculating the bouncing criterion based on the specific deposition conditions. The calculated values are plotted and compared against the model predictions. A threshold of transition will be established and irregularities in the observed droplet deposition behavior will be discussed.

4.2 Concept Validation: Differential Surface Energy as Bouncing Potential

The data from the high-speed imaging experiments are analyzed in this section. Custom video analysis software is used to extract the diameter evolution of the deposited droplets using 1-D line tracking strategy. The aggressive droplet base retraction preceding bouncing is confirmed quantitatively. Therefore, the assumption that droplet bouncing is an extreme form of recoiling after the initial spreading is verified. Droplet surface area evolutions are extrapolated from the diameter data by approximating the deposited droplets as cylinders with constant volumes. Finally, the occurrence of bouncing is quantitatively associated with the maximum differential surface energy differences of the deposited droplets. Since the maximum differential energies are shown to be functions of the specific melt-surface wetting conditions, the effect of wetting on droplet bouncing is hence verified.

4.2.1 Image processing and droplet diameter evolution

The high-speed imaging experiments generate profile image sequences showing droplets impacting and oscillating on prepared test surfaces. The backlighting technique adapted produces shadow images that, in spite of the structuring highlights projected by a second light source, provide essentially 2-D information on the droplet morphologies only. Nevertheless, the diameter evolution of a deforming droplet may be extrapolated by measuring the width of the droplet profile dynamically and assuming that the droplet shape is essentially axisymmetric. However, dynamic profile measurement requires processing a large number of images per recording session and accurately identifying the profile edges which represent the surface boundaries of the deforming droplets.

The high-speed camera system used in the experimental study generates 64 by 64 pixels, gray-scale images at 40,500 frames per second for up to 3 seconds per typical recording session. On average, up to 5 useable sequences of droplet deposition may be captured. Each captured sequence consists of between 50 to 400 image frames, depending on the droplet deposition behavior exhibited. The large quantity of the data collected represents a formidable image processing task. In addition, the limited image resolutions result in the blurring of the acquired images up to ± 3 pixels in magnitude, as shown in Figure 4.1. The blurring introduces considerable measurement uncertainty. A typical droplet at maximum spreading is measured to

be 55 pixels in width on average. The aforementioned edge blurring introduces a measurement uncertainty approximately 10 percent in magnitude. The error will be magnified if the images are measured manually, since only objective standards for edge detection may apply. The quantity of the image data and the inherent measurement uncertainty hence rule out sorting and measuring the images manually as a viable option.

Alternatively, the acquired images may be analyzed using commercially available software specifically designed to process high-speed image data. Large quantity of image data may be handled and processed efficiently with modest computational resources. While the blurring cannot be resolved directly by sorting and measuring the image data computationally, a consistent edge definition may be adopted to minimize the measurement variations. Practically, a specific gray-scale level can be pre-defined to represent an edge transition, indicating a possible droplet surface boundary, when analyzing the gray-scale images. While the true locations of the surface boundaries may still be ambiguous, an objective standard for edge detection can yield repeatable measurements.

Typical image processing software uses a strategy called feature tracking to extract the dynamics of objects in high-speed images. By tracking consistent and identifiable features on the objects in motion, dynamic parameters such as velocities and accelerations may be generated automatically. Example of feature tracking applied to an extending knife blade is shown in Figure 4.2. The dynamic information generated by feature tracking is highly desirable for the present analysis since determining the diameter evolution of the deposited droplets is a primary goal. However, the dynamically distorted surface of a post-impact, deforming droplet prevents the adaptation of this strategy, since no consistent and traceable feature is available, as shown in Figure 4.2. To address this issue, an alternative tracking strategy is employed. A beta version of the commercial video analysis software, MiDAS, (Xcitex, MA), was acquired. The functionality of the beta version used was enhanced to include a 1-D line tracking capability that is uniquely suitable for analyzing the dynamics of deformable objects. The tracking and measuring procedures, shown graphically in Figure 4.3, are described as follows. A sequence of JPEG-formatted high-speed images is loaded into the software. The 1-D line tracking function is activated and a measuring line is drawn across the expected impact zone just above the target surface on the image frame displayed. As the sequence is played forward, the images of the

impacting and deforming droplets will intercept dynamically with this measuring line. The software is programmed to identify the gray-scale level transitions, first from light-to-dark pixel then from dark-to-light pixel, as droplet surface boundaries and track their motions automatically. The sensitivity of the edge detection may be tuned by altering the measuring line thickness and the preset threshold intensity used to identify the gray-scale transitions. Increasing the measuring line thickness averages the transition locations over a vertical range, and hence yields measurements that are less sensitive to the droplet surface curvatures. However, the high-speed images acquired lack the vertical pixel resolution to take advantage of this strategy. Therefore, the measuring line thickness is fixed at one pixel in height for all image processed in the present analysis. The threshold intensity represents the gray-scale level that is programmed to associate with an edge transition. The high-speed images acquired are gray-scale images recorded in 255 levels, where 0 and 255 represent pure white and pure black levels, respectively. Typically, threshold intensity set between 120 and 140 produced the best edge detection results for the images processed in this study. The screen display of high-speed images processed using MiDAS is shown in Figure 4.4.

The locations and the types of edge transitions detected in the image frames are exported into a data text file for each sequence analyzed. The droplet surface boundaries are represented by the horizontal pixel positions alone the measuring line recorded when the local gray-scale levels reach the pre-set threshold intensity. The types of the transitions are identified by a binary number, where 0 and 1 indicate the light-to-dark and dark-to-light transitions, respectively. Ideally, only one type of transition each, indicating either left or right edge of a deforming droplet, is detected per image frame. However, the interceptions of the droplet image highlights with the measuring line may also produce edge-like transitions and can be mistakenly interpreted as surface boundaries, as shown in Figure 4.5. To ensure that the actual droplet boundaries were detected reliably, the software was programmed to identify up to 10 edge transitions per each image frame. The erroneous transitions produced by highlights are then filtered out using a custom Java™ routine. The filtering routine first truncates the outputted data file so only entries containing edge transition information remain. Next, the types of edge transitions recorded per image frame are sorted into subgroups. The transitions with the minimum horizontal position in the light-to-dark subgroup and the maximum horizontal position in the dark-to-light subgroup are identified as the actual surface boundaries of a deformed droplet. The minimum and maximum

transitions are then isolated from their respective subgroups and the erroneous transition data is discarded. The instantaneous droplet diameter in each image frame is then determined by calculating the horizontal distance between the retained transition pair. Finally, the diameter evolution of droplet deposition is generated by plotting the diameters measured from the images over the recorded period.

The diameter evolution for droplets exhibiting sticking, partial bouncing, and complete bouncing behaviors are shown in Figure 4.6. The plots are generated by analyzing high-speed images of Pb-37wt% Sn solder droplets depositing on the Pd-plated, Au-plated, Rh-plated, Sn-plated, and bare Cu and Al substrates. These surfaces represent targets with deteriorating droplet-surface wetting conditions. The static contact angles of Pb-37wt% Sn solder on these surfaces are listed in Table 3.2. The average initial diameters, D_{ini}, of the droplets are approximately 285μm and the average impact velocity, determined from the high-speed images, is approximately 3.8m/s. As shown in the figure, all deposited droplets behaved similarly during the initial spreading phases. The maximum spreading diameters were typically reached within 0.17ms after impact, with a maximum spreading ratio, ζ_{max}, of approximately 2.7 on average. The standard deviation of ζ_{max} among depositions on different surfaces is around 10%, which is similar in magnitude with the measurement uncertainty of the image processing procedures described earlier. The uniform values of the measured ζ_{max} verify the assumption that the maximum spreading factor is a function of the impact conditions and is independent of the specific droplet-surface wetting condition.

The deposited droplets are shown to hesitate momentarily at their maximum spreading states, for a period ranging from 20 to 70μs, before the recoiling phase is initiated. However, the recoiling dynamics of the deposited droplets differ significantly among droplets exhibiting different deposition behavior.

The droplets deposited on the Pd-plated and Au-plated surfaces exhibit sticking behavior. The base shrinkage, β, of the deposited droplet can be calculated as

$$\beta = \frac{\left(D_{max}^2 - D_{min}^2\right)}{D_{max}^2} \times 100\% \qquad (4.1)$$

where D_{max} and D_{min} are the diameters at the beginning and end of the recoiling phase, respectively. According to the diameter evolution, base shrinkages of 48% and 57% are incurred by droplets deposited on the Pd-plated and Au-plated surfaces, respectively. The flow front retraction rate, υ_r, is calculated as

$$\upsilon_r = \frac{(D_{max} - D_{min})}{2t_r} \qquad (4.2)$$

where t_r is the recoiling period. The recoiling period is shown to be 0.35ms on average for droplet deposited on either the Pd-plated or Au-plated surface. Consequently, the flow front retraction rates are determined to be 0.3m/s and 0.39m/s on the Pd-plated and Au-plated surfaces, respectively. The initial recoiling phases of the deposited droplets are shown to be followed by a series of oscillations. Interpolated from the plotted curves, the sticking droplets eventually reach equilibrium diameters of 600μm and 650μm on Pd-plated and Au-plated surfaces, respectively.

A secondary droplet is produced as a result of the partial rebound of the droplet deposited on the Ph-plated surface. The base diameters recorded after the separation of the secondary droplet are hence marked as double triangles in the figure. The base of the deposited droplet incurs a 87% shrinkage before the separation of the secondary droplet. The recoiling period is approximately 0.45ms, hence corresponds to a flow front retraction rate of 0.5m/s. The diameter of the secondary droplet is measured to be around 200μm, and hence accounts for roughly 35% of the original droplet volume. The remaining portion of the deposited droplet, after a series of oscillations, reaches a steady state base diameter of approximately 340μm.

The droplets deposited on the Sn-plated, Cu, and Al surfaces exhibit complete bouncing behavior. The droplets deposited on the Sn-plated and Cu surfaces retract and disengage completely from the target surfaces within 0.5ms after the onset of recoiling. According to the last diameters measured prior to droplet rebounds, the flow front retraction rates are estimated to be approximately 0.8m/s and 0.7m/s, respectively. The droplet deposited on the Al surface rebounds from the surface within 0.4ms with an estimated υ_r of 0.9m/s.

The calculated base area dynamics of the deposited droplets hence correlate an increase in the droplet base shrinkage with a greater tendency for the droplets to bounce. In addition, the flow front retraction rate during the recoiling phase increases as the droplet deposition behavior transits from sticking to partial and complete bouncing. These observations confirm the assumption that the droplet bouncing is the consequence of an aggressive form of droplet recoiling following the initial, post-impact spreading.

4.2.2 Droplet surface area evolution

Ideally, the surface area of a deforming droplet may be extrapolated from its profile image by assuming the droplet shape to be axisymmetrical. However, tracking the profile of a deforming droplet dynamically is beyond the capability of MiDAS. Therefore, a generalized droplet shape is adopted to establish the droplet geometry from the diameter data. The deforming droplet during its spreading-recoiling phases is approximated by a contact volume cylinder with variable base diameter. Examining the high-speed images of the deposited droplets confirm that it is an acceptable shape approximation from initial spreading to the early stage of the recoiling phase. The geometry of the cylindrical shape model is shown in Figure 4.7. Assuming the molten solder as incompressible fluid, the geometry of the cylindrical model can be determined dynamically based on the mass conservation principle as

$$D_d^2 h_d = \frac{2}{3} D_{ini}^3 \tag{4.3}$$

where D_d and h_d, respectively, are the instantaneous base diameter and height of the deforming cylinder. The total surface area, A_c, of the cylinder is hence given as

$$A_c = \frac{\pi}{2} D_d^2 + \pi D_d h_d \tag{4.4}$$

As shown in Equation 4.3, h_d can be uniquely determined if D_{ini} and D_d are known. Therefore, by representing h_d as a function of D_{ini} and D_d in Equation 4.4, the surface area of a deforming cylinder can be written as,

$$A_c = \frac{\pi}{6}\left(3D_d^2 + 4\frac{D_{ini}^3}{D_d}\right) \quad (4.5)$$

Therefore, the surface area dynamics of a deforming droplet may be estimated using Equation 4.5 if the droplet base diameter evolution is known.

The surface area evolution, as shown in Figure 4.8, is estimated based on the diameter data presented in the previous section. The surface area dynamics during the initial spreading phases are shown to be comparable among droplets exhibiting sticking, partial bouncing, and complete bouncing behaviors. The deposited droplets are shown to reach an average maximum surface area, A_{max}, of 0.95mm^2 within 0.17ms after impact.

Recoiling generally occurs within 0.7μs after the maximum spreading diameter is reached. The surface area dynamics of the deposited droplets during recoil exhibit variations consistent with the observed differences among their diameter evolutions.

The surface areas of the sticking droplets, deposited on the Pd-plated and Au-plated surfaces, are shown to reduce to 0.55mm^2 and 0.5mm^2 at the end of the recoiling phase, respectively. The associated area reduction rate, υ_A, is determined as

$$\upsilon_A = \frac{(A_{max} - A_{min})}{t_r} \quad (4.6)$$

where A_{min} is the minimum surface area of a deformed droplet. Corresponding to an average recoiling period of 0.35ms, υ_A for droplets deposited on the Pd-plated and Au-plated surface are determined to be 1170mm^2/s and 1470mm^2/s, respectively.

The surface area of the partially bounced droplets, deposited on the Rh-plated surface, reached a minimum of 0.3mm^2 just prior to the separation of the secondary droplet, with an associated area reduction rate of 1490mm^2/s. After the separation of the secondary droplet, Equation 4.5 is modified to include the surface area of the separated sub-droplet as

$$A_c = \frac{\pi}{6}\left(3D_{dm}^2 + 4\frac{D_{ini}^3}{D_{dm}}\right) + \pi D_s^2 \tag{4.7}$$

where D_{dm} and D_s are the measured base diameter and secondary droplet diameter, respectively. Consequently, the calculated droplet surface areas after the separation of the secondary droplet, indicated by double triangles in the figure, incur a net upward shift in their values.

The surface areas of the completely bounced droplets, deposited on the Sn-plated and Cu surfaces, are shown to reach a minimum of 0.29mm^2 at 0.3ms after the initiations of their recoiling phases. The area reduction rates are consequently calculated to be 2420mm^2/s and 2640mm^2/s, respectively. The droplet rebound from the Al surface is shown to reach a similar minimum surface area at 0.22ms after the onset of its recoiling phases, with an estimated area reduction rate of 2610mm^2/s. The calculated surface areas of the completely bounced droplets on Sn-plated, Cu and Al surfaces increase steeply after reaching their minimum values. According to Equation 4.3, the surface area of the cylindrical approximation will approach infinity as D_d is reduced toward zero. In addition, examining the high-speed images reveals that the cylindrical approximation of the droplet shape is no longer valid in the vicinity of droplet rebound. Therefore, the exponential area growths calculated are considered erroneous and the data are truncated accordingly.

In summary, differences in the surface area dynamics during the recoiling phases of the deposited droplets are observed. As the tendency for the deposited droplets to bounce becomes greater, the rate and the amount of the surface area reduction increase accordingly. The higher area reduction rates associated with the bounced droplets are consistent with the assumption of bouncing as an aggressive form of recoiling, as verified in the previous section. Since the recoiling of a deposited droplet is assumed to be driven by tendency of a deformed droplet to restore its equilibrium shape, a larger surface area reduction implies a greater deviation from its equilibrium surface configuration. Since the surface energy difference is scaled with the extent of the deviation from equilibrium, the greater deviations associated with the bounced droplets suggest greater differences between their surface energies at maximum spreading and

equilibrium states. The differential surface area dynamics of the deposited droplets will be examined in the next section to verify this suggestion.

4.2.3 Differential surface energy dynamics

Once the dynamic surface area of a deforming droplet is determined, its associated surface energy can be determined as

$$SE_d = \left(\frac{\pi}{4} D_d^2 + \frac{2\pi}{3} \frac{D_{ini}^3}{D_d} \right) \gamma_{mg} + \frac{\pi}{4} D_d^2 (\gamma_{ms} - \gamma_{sg}) \tag{4.8}$$

where γ_{mg}, γ_{sg}, and γ_{ms} are melt-gas, solid-gas, and melt-solid surface tensions, respectively. Representing the term $\gamma_{sg} - \gamma_{ms}$ as a function of γ_{mg} using the Young-Dupre equation, Equation 4.8 can be rewritten as

$$SE_d = \left[\frac{\pi}{4} D_d^2 (1 - \cos\theta_e) + \frac{2\pi}{3} \frac{D_{ini}^3}{D_d} \right] \gamma_{mg} \tag{4.9}$$

where θ_e is the static contact angle. Equation 4.9 indicates that the dynamic surface energy of a deposited droplet may be evaluated if the instantaneous measured base diameter, D_d, is known.

The differential surface energy, proposed in Chapter 2 as the specific potential for droplet bouncing, can hence be determined dynamically as

$$\Delta SE_d = SE_d - SE_{equ} \tag{4.10}$$

where SE_{equ} is the surface energy at equilibrium. SE_{equ}, as described in Chapter 2, is a unique function of θ_e. Substituting Equation 2.26 and Equation 4.9 into Equation 4.10, the dynamic differential surface energy, ΔSE_d, can be determined as

$$\Delta SE_d = \frac{\pi}{4}\left\{\left(D_d^2(1-\cos\theta_e)+\frac{8}{3}\frac{D_{ini}^3}{D_d}\right)-D_{ini}^2\left[\frac{4\sin\theta_e}{\tan^2(\theta_e/2)(2+\cos\theta_e)}\right]^{\frac{2}{3}}\left[\frac{2(1-\cos\theta_e)}{\sin^2\theta_e}-\cos\theta_e\right]\right\}\gamma_{mg} \quad (4.11)$$

Equation 4.11 represents ΔSE_d as a function of D_d for a given set of deposition conditions. The evolution of ΔSE_d, extracted from the measured diameter data, is shown in Figure 4.9. Since the primary interest of the present study focuses on the deposition dynamics within the first spreading-recoiling cycle, the plot is scaled to focus on the surface energy evolutions within this period.

According to Figure 4.9, the differential surface energy for the deposited droplet peaks when the droplet reaches its maximum spreading diameter, approximately 0.15ms after impact. It may be noted that at $D_d = D_{max}$, Equation 4.9 becomes Equation 2.12b, which defines the maximum droplet surface energy just before recoiling. Consequently, ΔSE_d calculated at maximum spreading is equivalent to the specific potential for droplet bouncing, as defined in Equation 2.31. At their maximum spreading states, ΔSE_d for the sticking droplets, deposited on the Pd-plated and Au-plated surfaces, are 0.028mJ and 0.029mJ, respectively. In contrast, the maximum value of ΔSE_d for the partially bounced droplet, deposited on the Rh-plated surface, is about 0.07mJ. ΔSE_d for the completely bounced droplets, deposited on the Sn-plated, Cu and Al surfaces, are shown to reach 0.11mJ, 0.10mJ, and 0.13mJ at maximum spreading, respectively. The data hence shows quantitatively that increases in the tendency for the deposited droplets to bounce are correlated to increases in their specific differential surface energies. Since the differential surface energies are functions of the specific surface wetting conditions encountered during their deposition, the effect of wetting on the potential for bouncing is hence verified.

4.3 Concept Validation: Roughness Effect on Droplet-Surface Wetting

This section describes the procedures adopted to quantitatively verify the surface roughness effect on droplet-surface wetting during droplet deposition. The test substrate surfaces are first characterized using an optical profilometer. The roughness parameters generated are then used to define the notched surface model proposed in Chapter 2. Representing the actual surfaces

with the surface model, the extents of melt penetration under the deposited droplets and the associated effective area fractions are estimated. The area fraction can be used to determine the adjusted contact angles which quantify the roughness-induced incomplete wetting. The calculated angles are compared with the values measured from the high-speed images. The agreements between the calculated and measured values verify the surface roughness effect concept.

4.3.1 Characterization of the test substrate surfaces

As described in Chapter 3, three types of test substrates were prepared to study the effect of surface roughness on droplet bouncing. The substrates began as bare Cu plates and were either polished using 0.3μm Al_2O_3 slurry or sandblasted with 27μm and 180 μm Al_2O_3 particles before the final Au plating. The surface treatments were designed to produce surface finishes typical of targets encountered in the direct droplet deposition bumping application. The finished surfaces can be categorized as smooth, semi-rough, and rough. A stylus profilometer was used to determine the average surface roughness, Ra, of the finished surfaces. The surface preparation procedures and the resultant roughness characteristics are summarized in Table 3.3.

The defect structures of surfaces roughened by sandblasting are random. Analytical description of the interaction between the molten solder and these surfaces is therefore difficult. To address this issue, a generalized surface model was developed to simulate the actual substrate surfaces. The model, as described in Chapter 2, consists of an ideally flat surface populated with conical notches. The geometries of these notches may be defined by roughness parameters determined empirically.

To obtain the roughness parameters needed to define the notched surface model, the roughened substrate surfaces were scanned using an optical profilometer (Zygo, NewView 5000), as shown in Figure 4.10. Based on the principle of white light interferometry, the characteristics of the test surface can be imaged and measured without contacting the surfaces [Wilson and Sheppard, 1984]. Illuminating white light is generated from the profilometer and divided within a two-beam Mirau interferometer at the microscope objective. One portion of the light is directed toward and reflected from the test surface, while the other portion is reflected from a reference surface within the objective. Both portions are then combined and directed back to a CCD

imaging array. If the path lengths the lights reflected from the test surface and the reference are equal, the interference of the two light wavefronts produces images of alternating light and dark bands called fringes. Therefore, by vertically attenuating the microscope objective according to the fringe properties, the topology of the scanned surface can be extrapolated. In practice, the test surface is scanned by moving the objective vertically using a piezoelectric transducer. As the surface is being scanned, the intensities of the individual CCD pixels are captured and recorded. The results produced are three dimensional. The vertical measurements of the surface features are performed interferometrically. Lateral measurements, in the plane of the surface, are performed by calculating the pixel size from the field of view of the objective in use [Zygo Corp., 2000].

Unlike the stylus-based profilometer, the measurements obtained by the optical profilometer are not limited by the geometry and size of the stylus used. The optical profilometry hence offers much improved scanning resolutions. For the NewView analyzer used, depths up to 100μm, with 0.1nm resolution and 0.4nm RMS repeatability, are measured independent of the objective magnification. In addition, the 3-D surface profiles generated by the NewView analyzer allow qualitative assessment of the characteristic defect structures of test surfaces with different surface roughness.

The scanned results of the polished and sandblasted surfaces are presented in Figure 4.11(a-c). The scanned area is approximately 360μm by 270μm. The oblique 3-D surface profiles confirm qualitatively that as the surface roughness increases, the predominant surface defects change from small indents with steep slopes, as shown in Figure 4.11(a) and 4.11(b) for the polished and 27μm Al_2O_3 sandblasted surfaces, respectively, to large notches with relatively shallow wall angles, as shown in Figure 4.11(c) for the 180μm Al_2O_3 sandblasted surface.

As described in Chapter 2, the geometry of the conical notch defining the surface model is specified by its depth, h, and radius, r_c. By analyzing the actual bump-solid interfaces, the 10-point height, Rz, and the average period of the surface waviness, x_p, were selected to represent h and $2r_c$, respectively. The value of x_p is approximated by the low filter wavelength applied to determine the surface waviness during surface profiling. Representing the notch depth and diameter with Rz and x_p respectively, the notch angle, Φ, can be calculated as,

$$\Phi = \tan^{-1}\left(\frac{2R_z}{x_p}\right) \tag{4.12}$$

The calculated notch angle and the roughness parameters determined empirically for the test surfaces used in the roughness effect study are presented in Table 4.1. The summary confirms quantitatively that the characteristic surface defects evolve from the small indentations with sharp angles to deep notches with shallow angles as the surface roughness increases.

4.3.2 Effective area fraction and adjusted contact angle

The effective area fraction, F_a, was introduced in Chapter 2 to represent the effect of surface roughness on wetting. The analysis has shown that the value of F_a is proportional to the extent of the melt penetration into the surface defects. Consequently, F_a may be evaluated analytically once a typical defect on a rough surface is modeled as a conical shaped notch. Melt penetration is described as a result of the force balance between the applied pressure, surface tension, and the back pressure from the compression of the gas trapped within the notch. Given the initial droplet impact conditions and the defect notch angle, Equation 2.48 can be solved to determine the melt penetration depth, y_p. The effective area fraction, F_a, can then be determined as a function of the penetration ratio, $\eta = y_p/h$, using Equation 2.49.

Once the value of F_a for a deposited droplet on a specific rough surface is determined, the roughness induced incomplete wetting may be quantified by the adjusted droplet-surface contact angle, θ_e^*. Given the static contact angle, θ_e, θ_e^* can be determined as a function of F_a defined by Equation 2.43. Equation 2.43 indicates that θ_e^* will increase, indicating a deterioration of the droplet-surface wetting, as the value of F_a decreases from unity.

Based on the notch geometries defined in Table 4.1, the penetration ratios, the effective area fractions, and the resultant adjusted contact angles for the test substrates are calculated and listed in Table 4.2. As shown in the table, the penetration ratio decreases as the surface roughness increases; from 96% for the polished surface to 59% and 24% for the 27μm and 180μm Al_2O_3 sandblasted surfaces, respectively. The associated effective area fractions also decrease from

0.98 for the polished surface, to 0.72 for the 27μm Al_2O_3 sandblasted surface, and finally to 0.39 for the 180μm Al_2O_3 sandblasted surface. Consequently, the adjusted equilibrium contact angles are calculated to be 32°, 55°, and 70° for the polished, 27μm and 180μm Al_2O_3 sandblasted surfaces, respectively. The analytically determined contact angles are compared to the measured results, obtained from the images of steady-state sessile drops of Pb-37wt% Sn solder on the roughened surfaces, are shown in the last column of Table 4.2. The comparisons show good agreement between the calculated and measured values with typical deviations less than ±5°.

In summary, the 3-D scanning of the test substrates confirms the assumed correlations between the defect characteristics and surface roughness. Specifically, the slopes of the characteristic surface defects will decrease as the surface roughness increases. Simulating the actual rough surfaces with the proposed surface model, the melt penetration and the associated effective surface area are determined. The melt penetration, described as a function of the defect notch angle, is shown to decrease as the surface roughness increases. Quantifying the effective area fraction as a function of melt penetration, the inverse correlation between F_a and the surface roughness level is verified. The adjusted contact angles are determined as functions of F_a to quantify the roughness induced incomplete wetting. The analytical estimates are found to agree well with the empirical measurements.

4.4 Bouncing Criterion Quantification

The analyses presented so far have verified that (1) the differential surface energy of a deposited droplet, a function of the specific droplet-surface wetting condition, may be adapted as the potential for droplet bouncing, and (2) the effect of surface roughness on bouncing may be represented by quantifying the roughness induced incomplete wetting. Therefore, the concept of adapting the normalized differential surface energy as a bouncing criterion to quantify the effects of wetting and surface roughness on bouncing is hence verified. Specifically, a deterioration of droplet-surface wetting condition and an increase in the target surface roughness should increase the bouncing potential, and hence the tendency for droplet bouncing. In the following sections, the bouncing criterions for the droplets deposited in the high-speed imaging study will be calculated and the effects of wetting and surface roughness on the bouncing criterion will be

verified. A threshold of transition will then be determined empirically where droplet recoiling is driven by sufficient potential to induce partial or complete bouncing.

4.4.1 Estimations of the maximum spreading diameter

As shown in Equation 2.51, the bouncing criterion is a function of the θ_e and ζ_{max}. While θ_e can be measured directly from the image of a sessile drop on surface, ζ_{max} is a transient parameter and hence needs to be measured dynamically. High-speed images may allow direct determination of ζ_{max}, but only for the limited number of droplet depositions that are successfully imaged. Alternatively, ζ_{max} may be approximated analytically, as shown in Equation 2.52, if the advancing dynamic contact angle θ_{ad} can be determined. The analysis presented in Chapter 2 has shown that the initial spreading of a droplet, deposited in the inviscid, impact-driven regime, is independent of the specific droplet-surface interactions. Therefore, the values of θ_{ad} are expected to be consistent among droplets deposited on different target surfaces used in the present experiments. Figure 4.12 shows a series of images of Pb-37wt% Sn solder droplets impacting and spreading on the Pd-plated, Rh-plated and Sn-plated surfaces. The initial spreading dynamics are confirmed to be insensitive to the target surfaces. In addition, the values of θ_{ad} are verified to be comparable among depositions on these surfaces and are estimated to be approximately 110° on average. Based on the estimated θ_{ad}, the maximum spreading factor for a 285μm, Pb-37wt% Sn solder droplet impacting a surface at 3.8m/s is approximately 3.2. The calculated value overestimates the average ζ_{max}, determined empirically, by about 15%. The overestimation is consistent with the errors reported by Pasandideh-Fard *et al.* [1996]. The discrepancies were most likely results of their rudimentary treatment of the viscous dissipation. Increasing the melt viscosity is shown to analytically improve the prediction of ζ_{max}, hence supports this explanation.

4.4.2 Bouncing criterion trends and threshold of transition

The bouncing potential for the droplets deposited in the high-speed imaging study are determined by empirically determining their maximum spreading factors from the high-speed images and substituting the results into Equation 2.51. The calculated bouncing criterion is

plotted against the model predictions, as shown in Figure 4.13. Two model predictions are generated; one is based on the analytically determined ζ_{max} while the other is calculated using the empirically obtained average ζ_{max}. It may be noted that the plotted data also include results from droplets deposited on the 27μm and 180μm Al_2O_3 sandblasted surfaces to represent the surface roughness effect.

The figure shows that the overestimations of the analytically determined ζ_{max} result in the over-prediction of the bouncing criteria for the given deposition conditions. However, the model predictions produced using the empirically obtained ζ_{max} show good agreement with the experimental data. The experimental data confirms that as the value of bouncing potential increases, the droplet deposition behavior transits from sticking to bouncing. In addition, as the droplet-surface wetting deteriorates, indicated by increases of the static contact angle, the bouncing potential increases and the tendency for a deposited droplet to bounce increases. Therefore, the data suggest that improving droplet-surface wetting may retard the occurrence of droplet bouncing.

The effect of surface roughness on the bouncing criterion is denoted by the data points representing droplets deposited on the 27μm and 180μm Al_2O_3 sandblasted surfaces. The bouncing potential for these droplets is calculated with empirically determined adjusted contact angles to quantify the roughness induced incomplete wetting. The results show that the bouncing criterion increases as the surface roughness increases. Therefore, minimizing surface roughness may aid in controlling droplet bouncing.

Close examination of the deposition results on the roughened surface, however, reveals phenomena that are not fully described by the current analysis. Specifically, droplets deposited on the 27μm and 180μm Al_2O_3 sandblasted surfaces are shown to encounter inconsistent wetting. In Figure 4.14, Pb-37wt% Sn solder droplets deposited on different regions of the same 27μm Al_2O_3 sandblasted surface are shown to exhibit variable deposition behaviors. These behavior variations appear to be correlated to the local wetting conditions. The good droplet-surface wetting condition is noted at the central region of the substrate surface, where a deposited droplet exhibits sticking behavior, as shown in Figure 4.14(a). However, the wetting condition becomes marginal at the left region of the same substrate, where a deposited droplet exhibits

aggressive recoiling and extensive necking, as shown in Figure 4.14(b). Necking is defined as a local constriction on the deforming droplet during aggressive recoiling. Partial bouncing represents a severe case of necking when the constriction pinches off the rising column and produces a secondary droplet. Therefore, extensive necking may be regarded as a precursor to partial bouncing and hence represents an increase in the potential for bouncing. It is believed that the roughened surfaces are more susceptible to contaminations which may be responsible for the local deteriorations of the droplet-surface wetting condition. Elemental analysis has not been able to quantitatively confirm the extent of contamination since the sources are unclear. Additional work may be needed to resolve this issue.

In addition to introducing inconsistent wetting, the roughened surfaces appear to have another, more fundamental, effect on the droplet deposition behavior. Figure 4.15 shows the depositions of Pb-37wt% Sn solder droplets on Sn-plated and 180μm Al_2O_3 sandblasted surfaces. Equivalent wetting conditions are expected as the static droplet-surface contact angles are shown to be comparable at 72° and 73° respectively. The values of the bouncing criteria, calculated based on the specific impact conditions, are 0.11 and 0.16 for depositions on the Sn-plated and 180μm Al_2O_3 sandblasted surfaces, respectively. The close approximation in values of the calculated bouncing criteria suggests similar deposition behaviors. However, significant differences are observed as described below.

Droplets deposited on both surfaces achieve equivalent spreading factors of approximately 2.6. The droplet deposited on the 180μm Al_2O_3 sandblasted surface, however, exhibits severe flow front instability that manifests into extensive edge irregularities visible at its maximum spreading stage. The irregularities become damped but still visible as the recoiling begins. Both droplets elongate vertically into columns at the end of their initial retraction phases. In contrast to the bouncing behavior exhibited on the Sn-plated surface, however, the retraction of the droplet base on the sandblasted surface slows to a stop toward the end of the recoiling phases. Consequently, the deposited droplet fails to detach and rebound from the sandblasted surface. The exhibited differences in the deposition behavior suggest that the droplet may be subjected to increased amount of dissipation through flow instability and friction at the melt-surface interface. Additional work is needed to investigate these hypotheses further.

In spite of the observed irregularities, a threshold for transition is established as a criterion value range separating the lower data points representing sticking and the higher data points indicating partial and complete bouncing. The threshold of transition is shown to range from 0.05 to 0.08. A droplet deposited within this range of bouncing criterion is hence expected to exhibit strong tendency for partial or complete bouncing. In practice, bumping process based on droplet deposition in this regime should be developed with some form of bouncing control strategy, most likely involving improvements of the target wetting conditions and modifications to the surface roughness characteristics. Further narrowing of this threshold range requires more empirical data produced in this regime and may be a potential area for future study. It may also be noted that the threshold range includes data points representing sticking droplets on the 180μm Al_2O_3 sandblasted surface. Since the roughness-induced mechanisms that retard bouncing for these droplets have not been investigated thoroughly, the apparent conflicts are noted but allowed when defining the transition threshold.

4.5 Summary

The analyses presented in this chapter examined the fundamental concepts behind the development of the bouncing criterion. Specifically, the tendency for a deposited droplet to bounce may be evaluated by using the differential surface energy as potential for bouncing. The differential energy concept was examined by analyzing the diameter, surface area, and surface energy evolutions of deposited droplets empirically. The concept was verified by positively correlating the occurrences of droplet bouncing with increases in the maximum differential surface energy. Since the surface energy of a deformed droplet is a function of the specific droplet-surface wetting condition, improving wetting was confirmed to decrease the bouncing potential. The effect of surface roughness on bouncing is described as a consequence of the roughness-induced incomplete wetting. By characterizing the test surfaces with notched surface model and determining the associated effective area fractions, the effect of roughness on wetting was quantified by determining the adjusted equilibrium contact angle. The analytically determined adjusted equilibrium contact angles were compared with the empirical measurements and were found to be in good agreement. The correlation between increase in surface roughness and deterioration of droplet-surface wetting was hence confirmed. The bouncing criterion for the

experimental results were determined and compared with analytical predictions. A threshold of transition was established to signify the transition from droplet sticking to bouncing behavior.

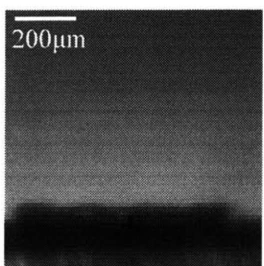

(a) Actual high-speed image*

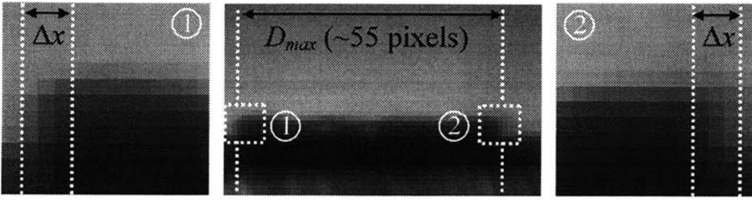

(b) Diameter measurement

Figure 4.1. Measurement uncertainty induced by the blurring of the high-speed image. (a) Pd-37wt% Sn droplet at maximum spreading on Pd-plated surface. (b) Measurement of D_{max}. Typically maximum diameter: ~55 pixels. Blurring at the droplet edge, shown as Δx, is shown to be around 3 pixels in magnitude.

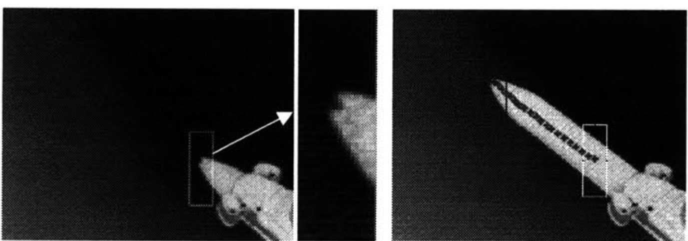

(a) Feature tracking of an extending knife blade (image courtesy of Xcitex, Inc.)

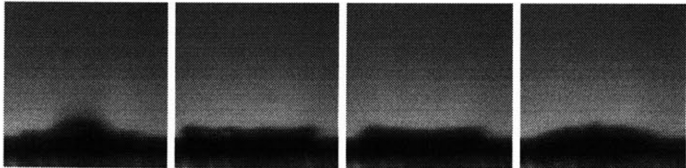

(b) Deforming droplet with no traceable feature

Figure 4.2. Feature tracking of an object in motion. (a) The velocity and acceleration of the extending knife blade are determined by tracking the motion of the blade tip. (b) Images of a deforming droplet near its maximum spreading diameter. The continuously distorted droplet surface offers no traceable feature.

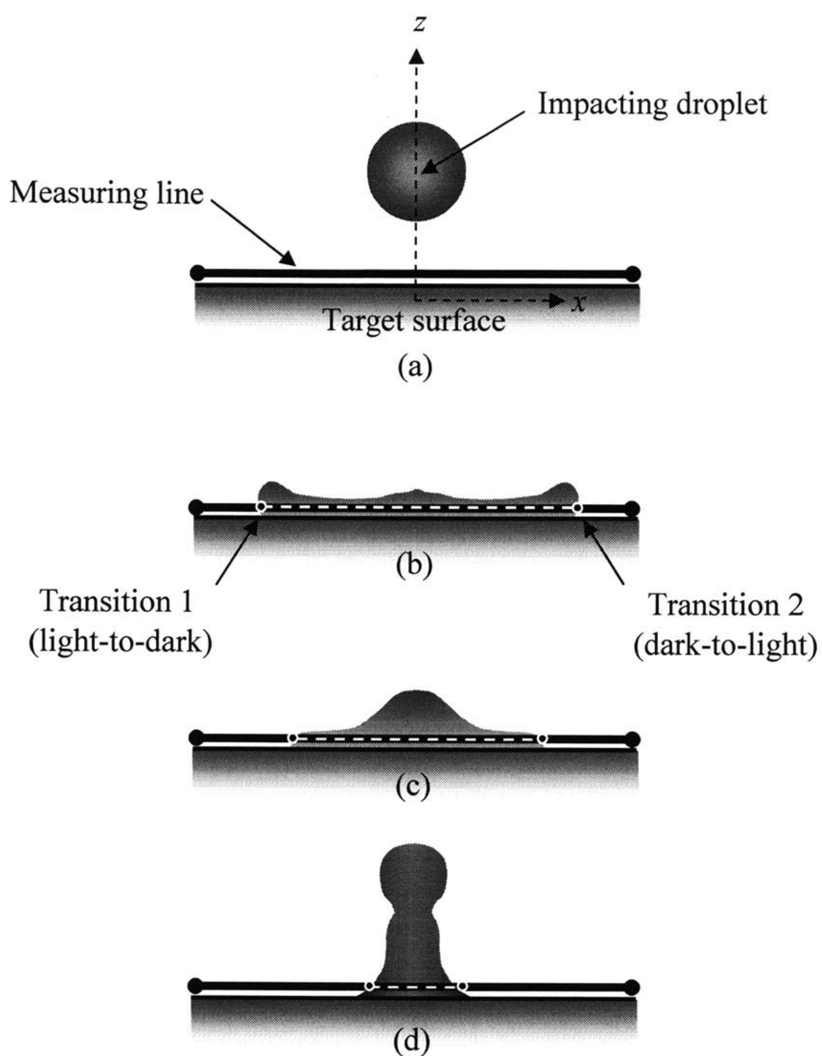

Figure 4.3. Schematics of image processing using the 1-D line tracking function. (a) A measuring line is drawn just above the target surface across the expected impact zone. (b) The edges of the deforming droplet intercept the measuring line and are detected according to the preset transition intensity. As the measuring line pixels are scanned from left to right, the positions and types of the transitions are recorded. (c)-(d) As the droplet continues to deform and oscillate on the surface, the positions of the detected transitions are updated continuously. The evolution of the droplet base diameter can be extracted by calculating the distance between the transitions dynamically.

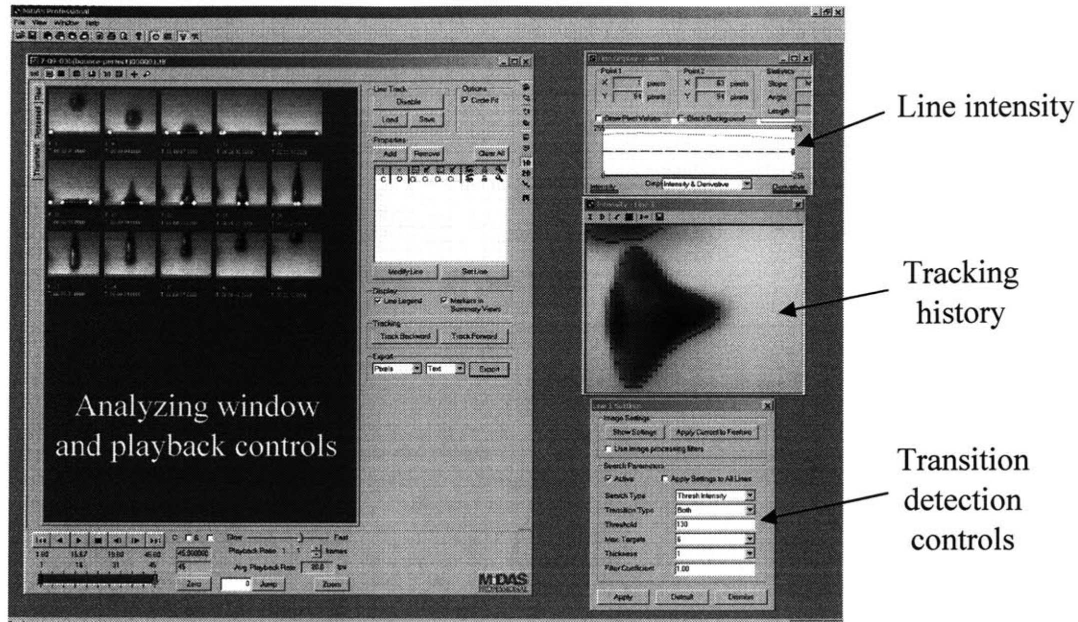

Figure 4.4. Processing high-speed images using the 1-D line tracking function in MiDAS.

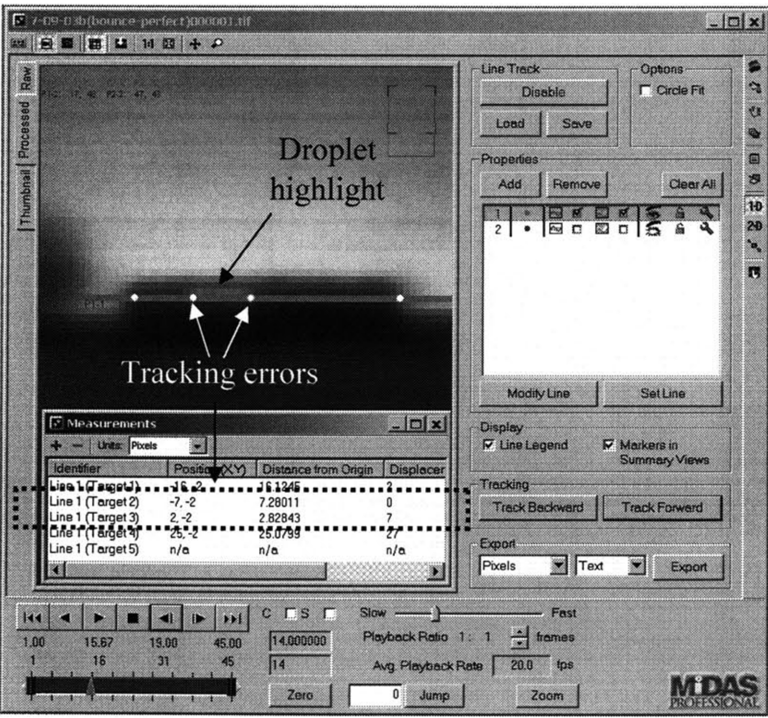

Figure 4.5. Tracking errors introduced by highlight intercepting with the measuring line.

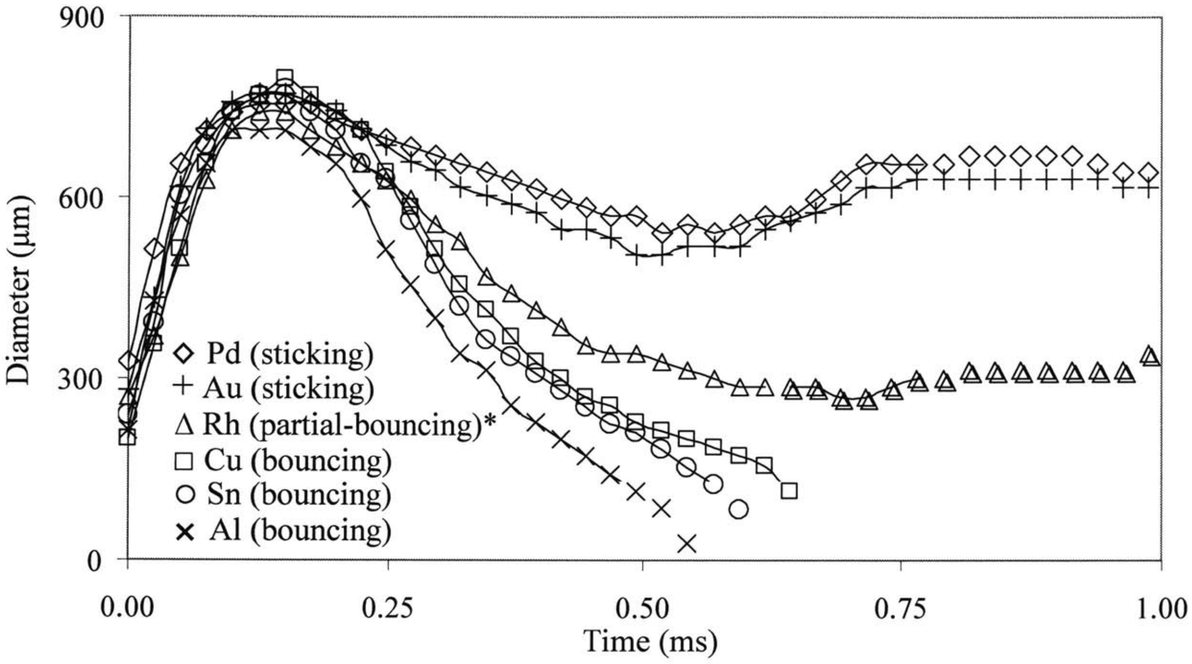

Figure 4.6. Evolution of the droplet base diameter on surfaces with different melt-surface wetting conditions. Droplet: Pb 63-wt% Sn solder; $D_{ini} \approx$ 285µm; $u_{ini} \approx$ 3.8m/s. The measured equilibrium contact angles, θ_e, are: 25°, 30°, 60°, 65°, 72°, and 90° for Pd-plated, Au-plated, Rh-plated, Cu, Sn-plated, and Al surfaces, respectively. *Double triangles indicate droplet diameters on Rh-plated surface after the separation of the secondary droplet.

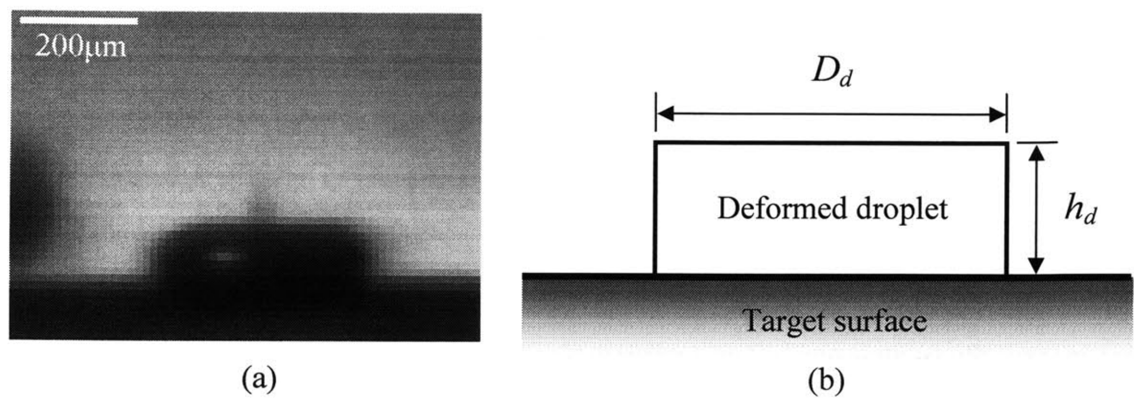

Figure 4.7. Cylindrical shape model for a deforming droplet. (a) A deposited droplet in the early stage of recoiling. (b) The geometry of the cylindrical droplet shape model.

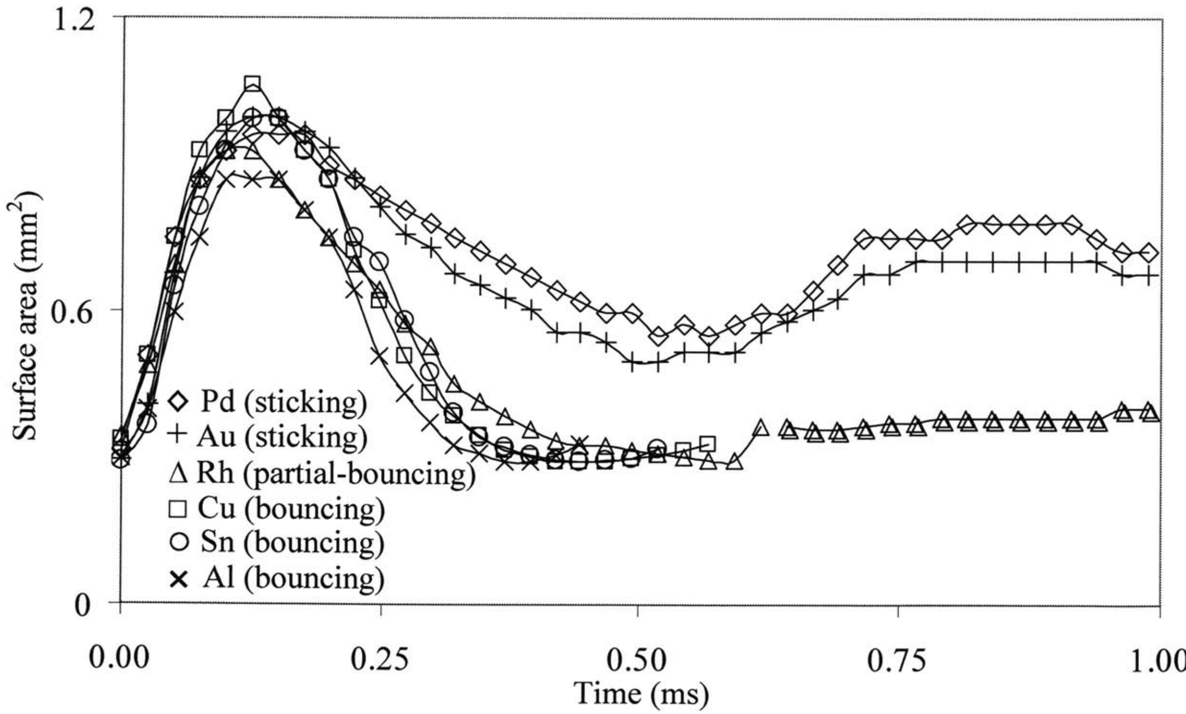

Figure 4.8. Evolution of the droplet surface area, extracted from the diameter data using the cylindrical shape model.

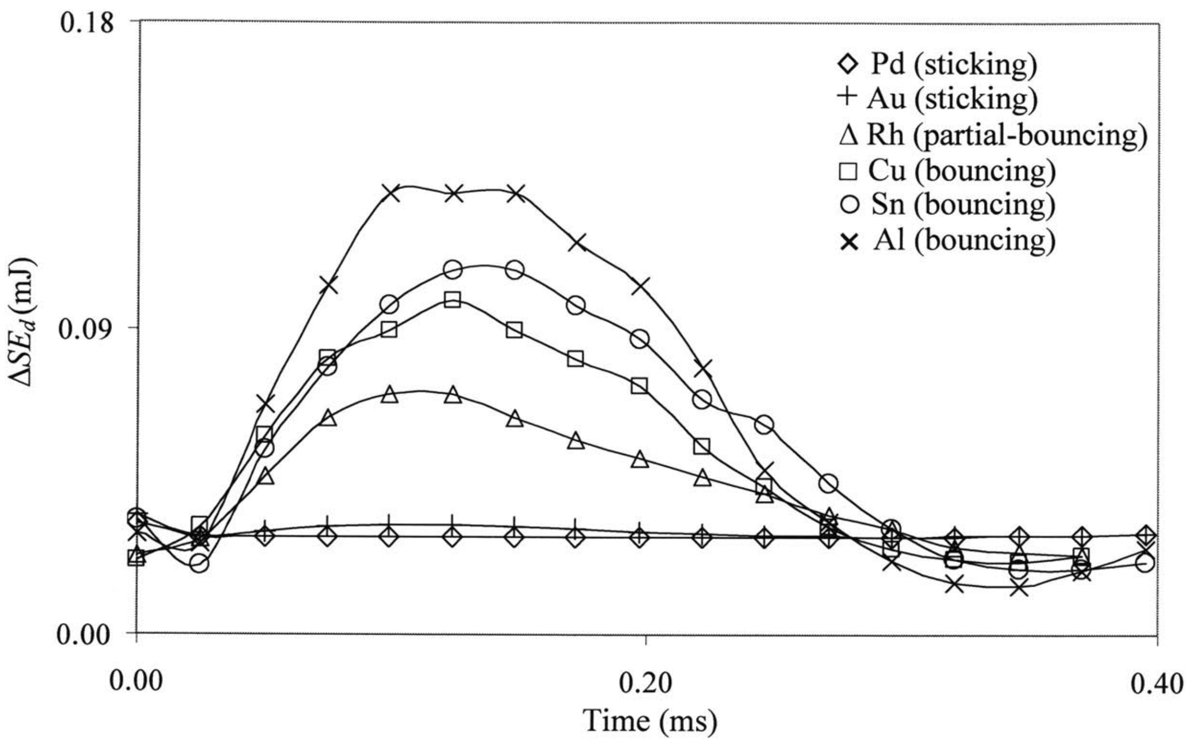

Figure 4.9. Evolution of the differential surface energy (ΔSE_d) of droplets deposited on surfaces with different melt-surface wetting conditions. Droplet: Pb 63-wt% Sn solder; $D_{ini} \approx 285\mu m$; $u_{ini} \approx 3.8 m/s$. The wetting conditions are represented by θ_e, which are measured as: 25°, 30°, 60°, 65°, 72°, and 90° for Pd-plated, Au-plated, Rh-plated, Cu, Sn-plated, and Al surfaces, respectively.

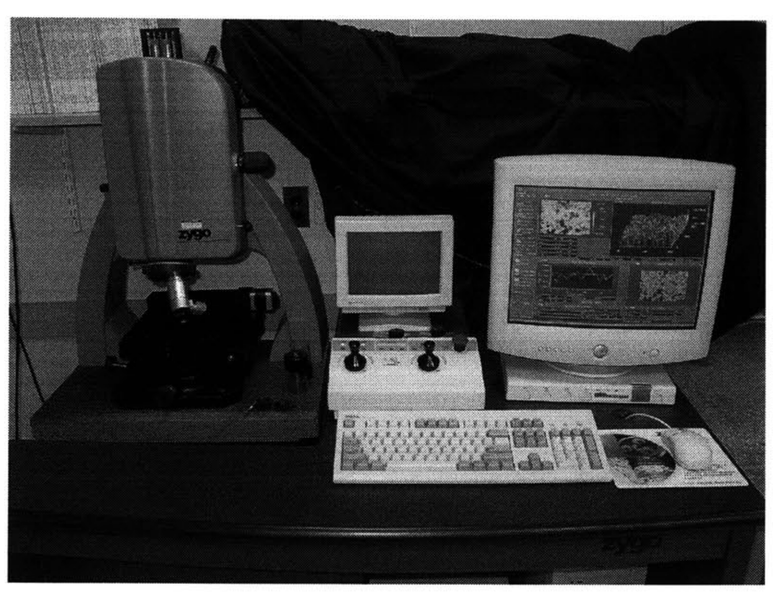

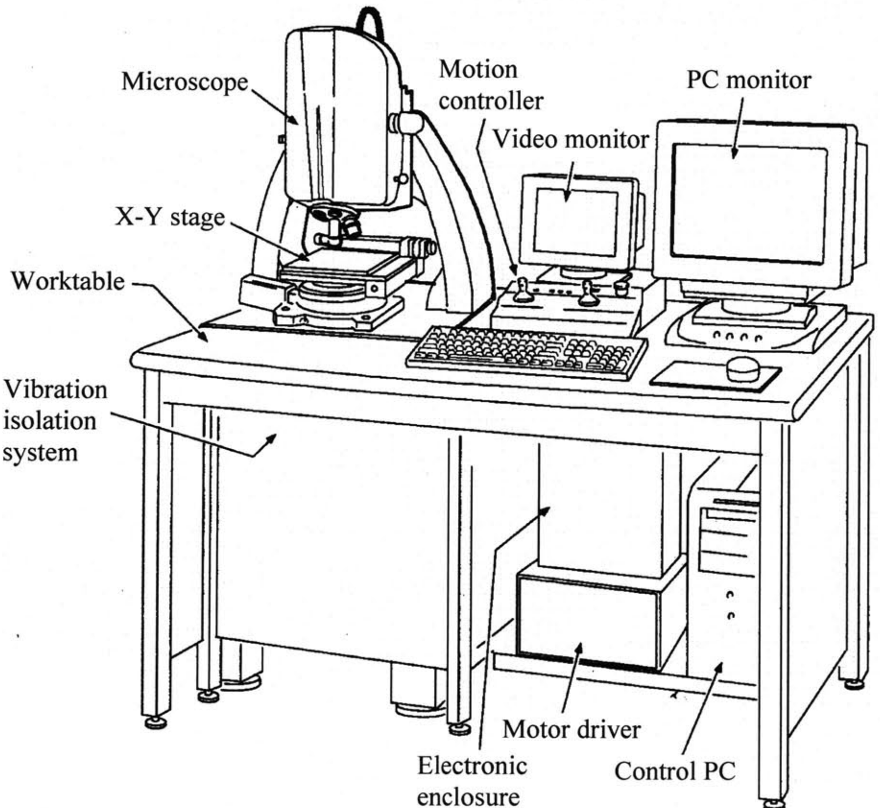

Figure 4.10. Zygo NewView 5000 optical profilometer system.

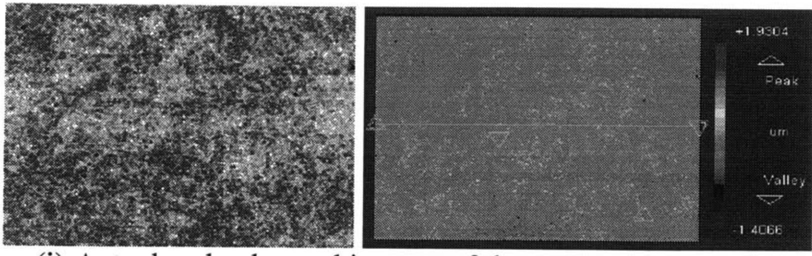

(i) Actual and enhanced images of the scanned topology

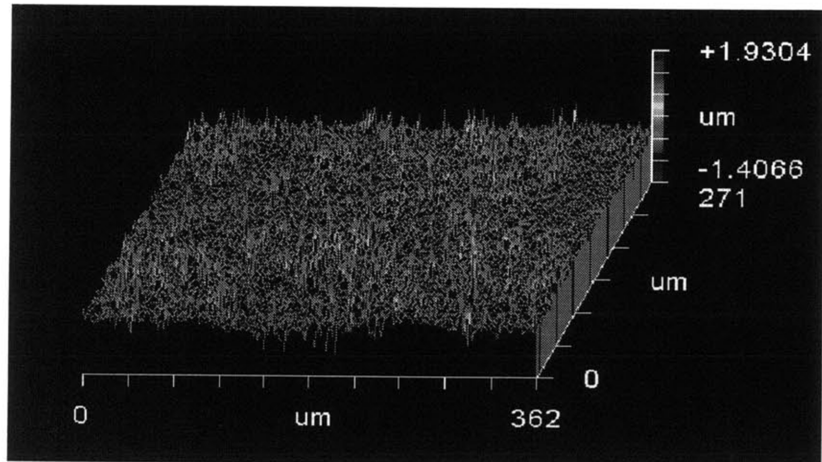

(ii) Oblique plot of the 3-D surface structure

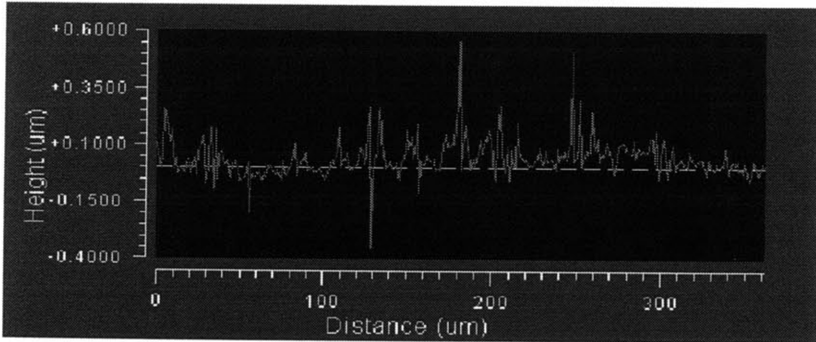

(iii) Line scan of the surface profile

Figure 4.11(a). Surface characteristics of 0.3 Al_2O_3 slurry polished surface with Au-plating. Scanned area: 360μm by 270μm. Objective: 50X Mirau.

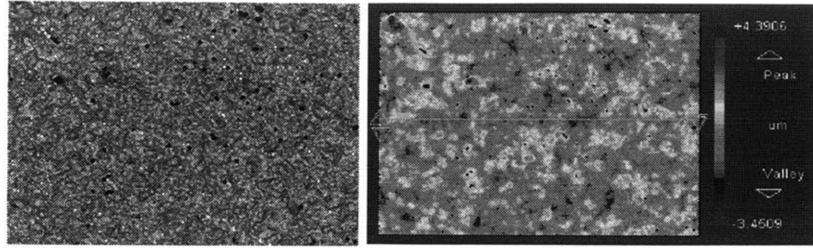

(i) Actual and enhanced images of the scanned topology

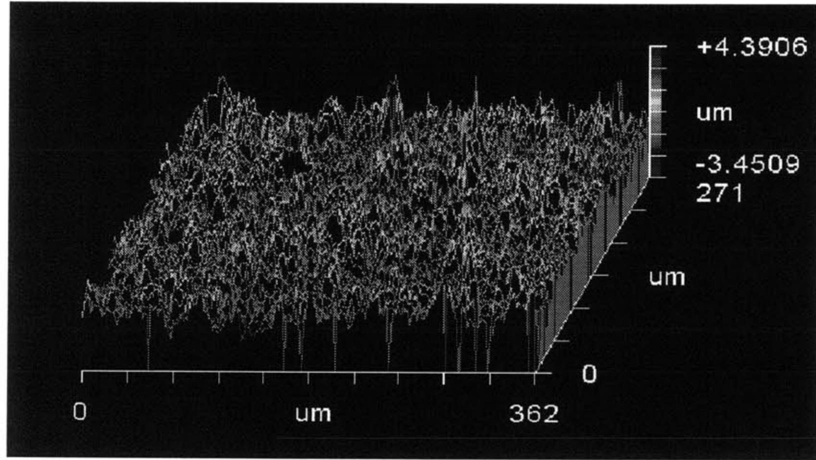

(ii) Oblique plot of the 3-D surface structure

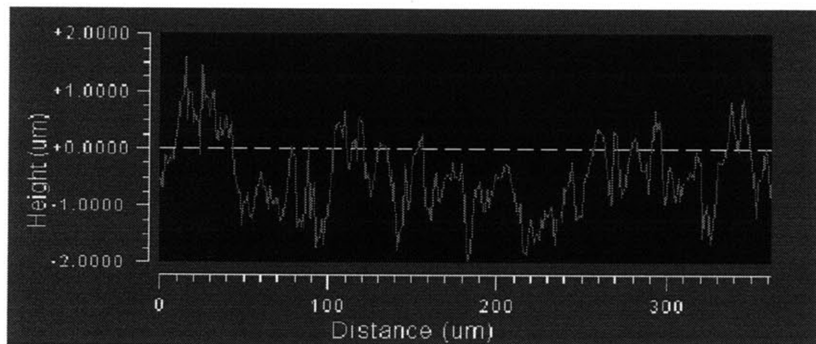

(iii) Line scan of the surface profile

Figure 4.11(b). Surface characteristics of 27 Al_2O_3 particle sandblasted surface with Au-plating. Scanned area: 360μm by 270μm. Objective: 50X Mirau.

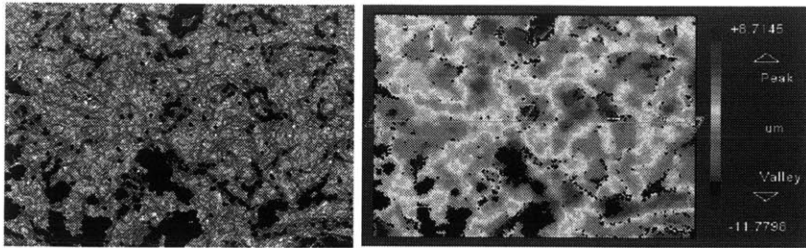

(i) Actual and enhanced images of the scanned topology

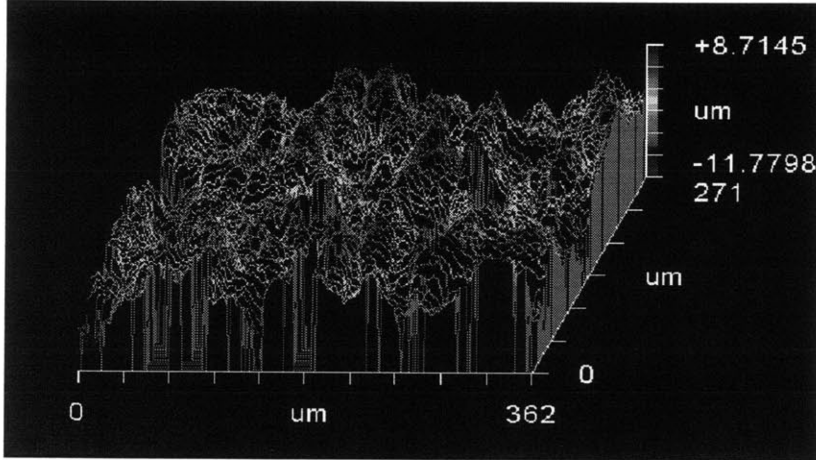

(ii) Oblique plot of the 3-D surface structure

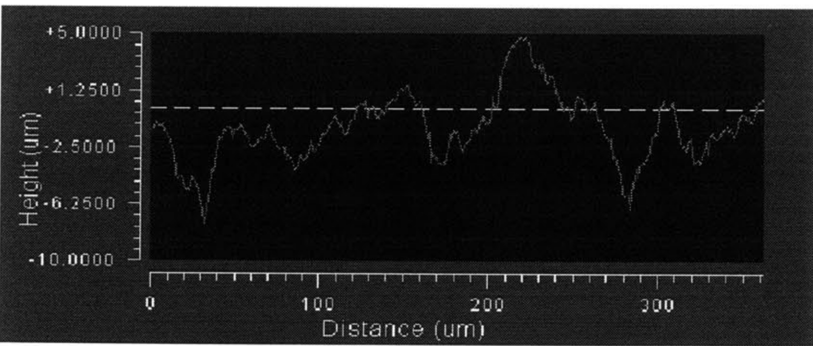

(iii) Line scan of the surface profile

Figure 4.11(c). Surface characteristics of 180 Al_2O_3 particle sandblasted surface with Au-plating. Scanned area: 360μm by 270μm. Objective: 50X Mirau.

Table 4.1. Measured and simulated defect characteristics of the test substrates.

Test substrates	Ra (μm)	Rz (μm)	x_p (μm)	Φ (°)
0.3μm Al_2O_3 slurry polished	0.02[1]	0.3	0.2[2]	71
27μm Al_2O_3 sandblasted	0.5[1]	2.5	10	26
180μm Al_2O_3 sandblasted	2.2[1]	6.4	100	7

[1] Obtained using the stylus-based profilometer (Tencor P-10)
[2] Minimum horizontal imaging resolution of the optical profilometer (Zygo NewView 5000)

Table 4.2. Measured and simulated wetting characteristics of the test substrates.

Test substrates	η	F_a	θ_e^* (°)	Ave. θ_e (°)
0.3μm Al_2O_3 slurry polished	0.96	0.98	32	28[1]
27μm Al_2O_3 sandblasted	0.59	0.72	55	52[1]
180μm Al_2O_3 sandblasted	0.24	0.39	70	73[1]

[1] Obtained from images of Pb-37wt% Sn solder drops on surface

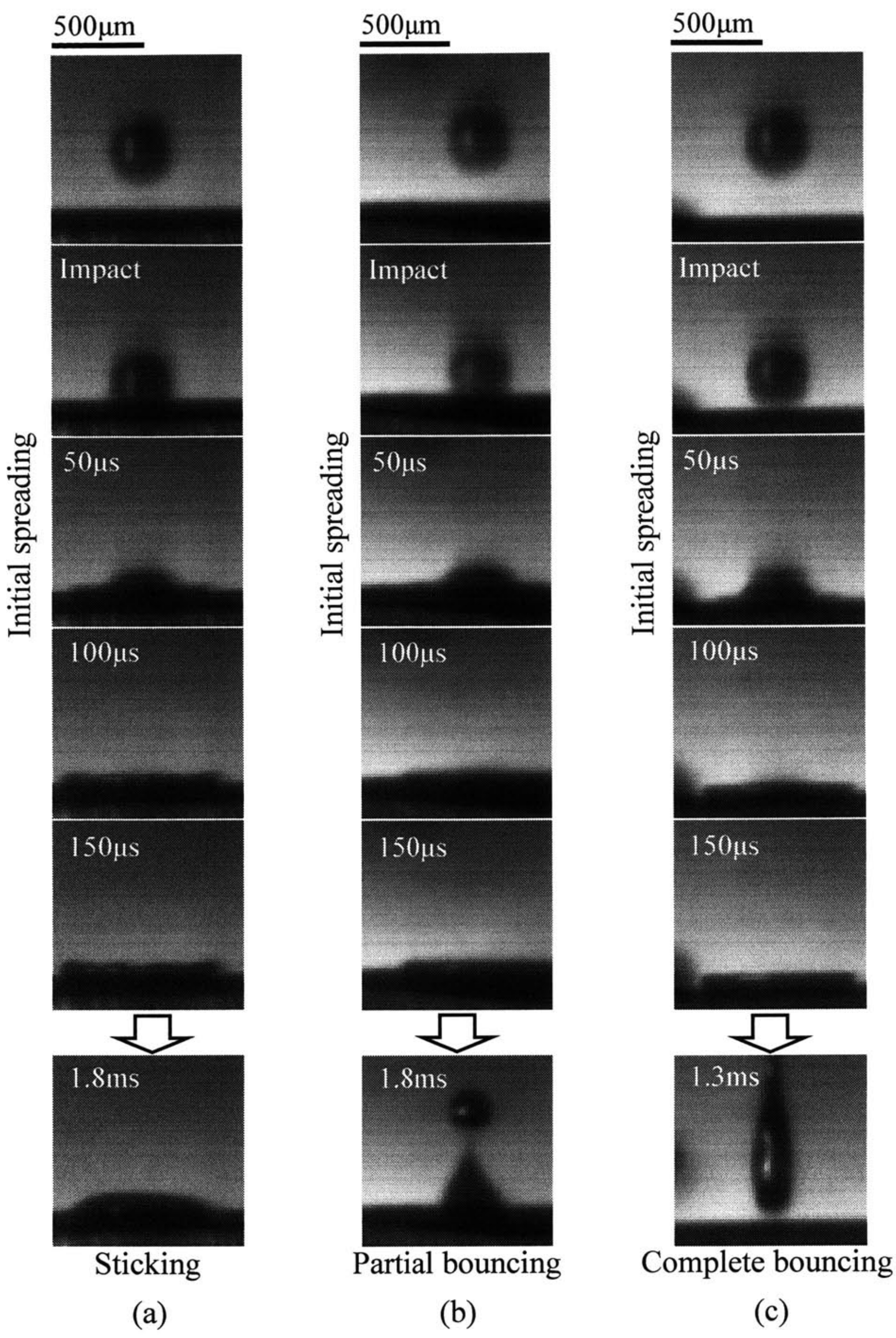

Figure 4.12. Droplets exhibit similar initial spreading dynamics when deposited on surfaces with different wetting conditions. Droplet material: Pb-37wt% Sn solder. (a) Sticking on Pd-plated surface. Droplet diameter: 287μm. Impact velocity: 3.6m/s. (b) Partial bouncing on Rh-plated surface. Droplet diameter: 287μm. Impact velocity: 4.1m/s. (c) Complete bouncing on Sn-plated surface. Droplet diameter: 283μm. Impact velocity: 3.9m/s.

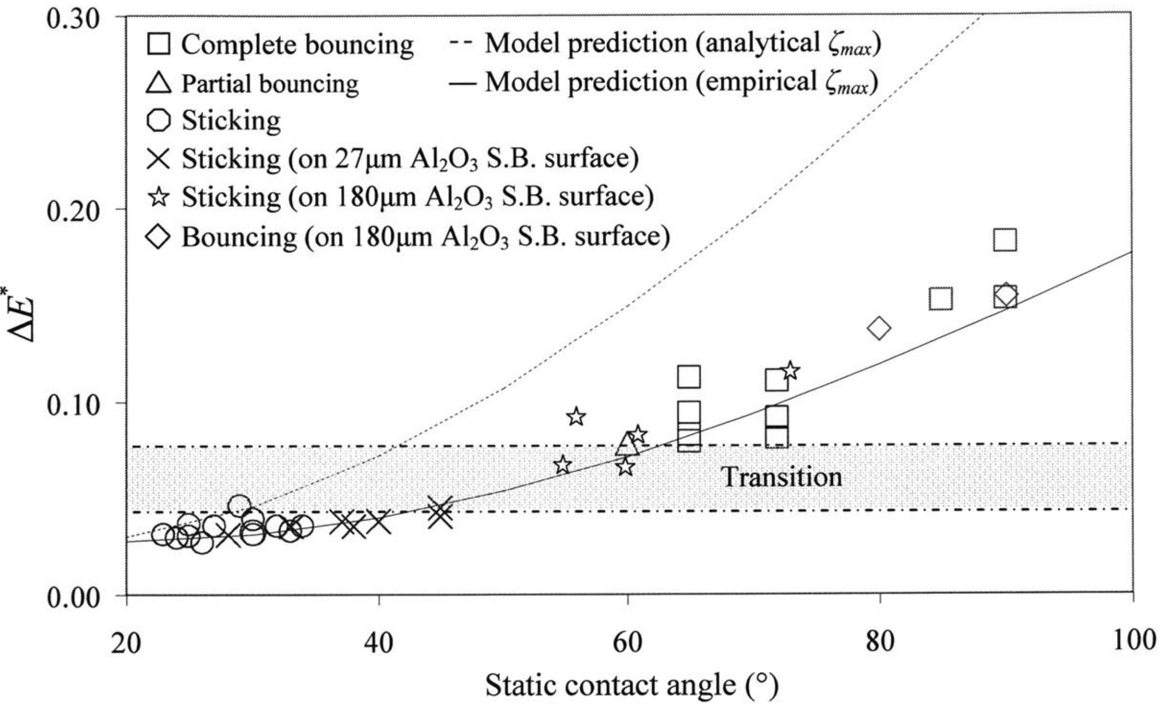

Figure 4.13. Threshold of transition determined by comparing empirical data to the model predictions. Squares, triangles, and circles denote droplets exhibit complete bouncing, partial bouncing, and sticking behaviors, respectively. Crosses and stars represent droplets exhibit sticking behavior on the 27μm and 180μm Al_2O_3 sandblasted surfaces. Diamonds represents bouncing droplet on the 180μm Al_2O_3 sandblasted surface.

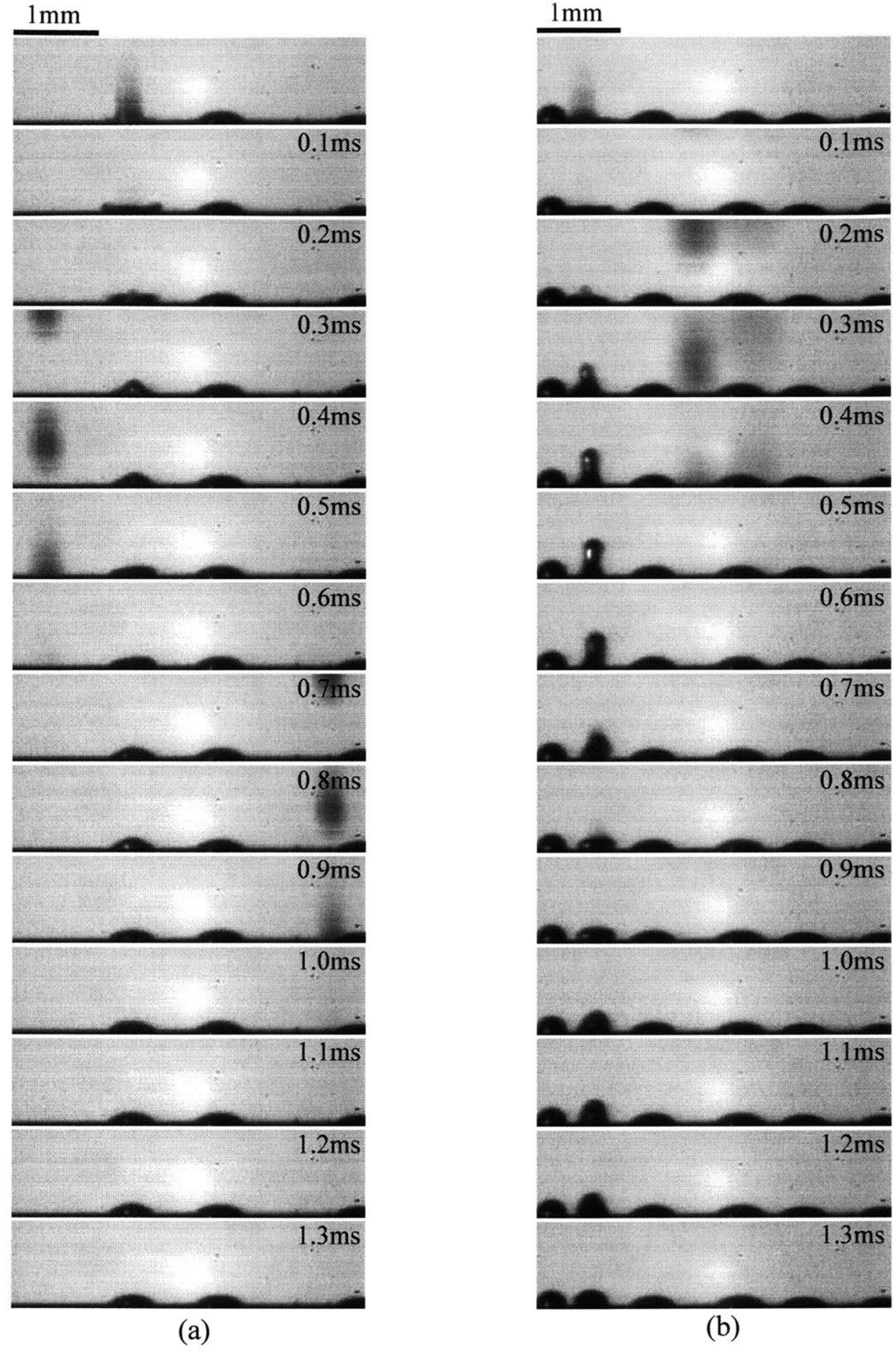

Figure 4.14. Local variations of the surface wetting condition on 27μm Al_2O_3 sandblasted surface. (a) Droplet deposited on the wetting region exhibits sticking behavior. (b) Droplet deposited on the poor-wetting region exhibits necking behavior.

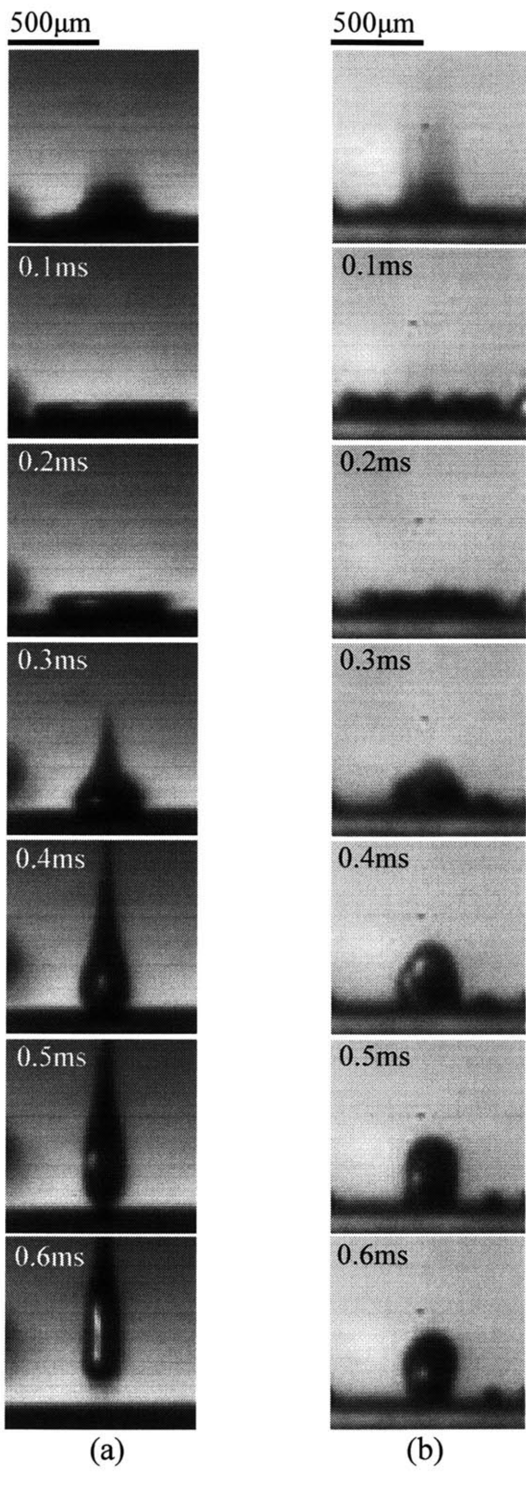

Figure 4.15. Variations of the droplet deformation processes on poor-wetting and roughened surfaces. (a) Pb-37wt% Sn droplet rebounds off Sn-plated surface ($\theta_e = 72°$). (b) Pb-37wt% Sn droplet necking on 180μm Al_2O_3 sandblasted, Au-plated surface ($\theta_e = 73°$).

Chapter 5. CONCLUSIONS

5.1 Summary of Findings

This thesis investigates the effects of droplet-surface wetting and target surface roughness on droplet bouncing in the parameter regime of a direct droplet deposition bumping process. The investigations aimed to identify the mechanisms responsible for both effects and to develop a practical criterion for the tendency for a deposited solder droplet to bounce. The analytical portion of the study examined the post-impact droplet deformation processes that lead to bouncing. Based on the principles of minimization of surface free energy and energy conservation, the following hypotheses were made:

I. The impact pressure of a UDS droplet deposited during direct droplet deposition bumping forces the droplet to deform and expand beyond its equilibrium spreading limit into a non-equilibrium disk shape. In contrast to the droplet's equilibrium shape, the non-equilibrium droplet configuration at maximum spreading has a greater surface free energy. The tendency for the droplet to minimize its surface free energy then forces it to recoil and restore its equilibrium, minimal energy configuration.

II. Droplet bouncing may be considered as a severe from of droplet recoiling. The recoiling of a droplet from its maximum spreading stage can be regarded as a process of converting the potential difference between the maximum spreading and equilibrium states into kinetic fluid motions. Since a droplet is momentarily at rest at maximum spreading and sessile at equilibrium, the energies at both states may be estimated solely by the associated surface energies. Therefore, the potential that drives the droplet recoiling may be represented as the differential surface energy between the maximum spreading and equilibrium states. A greater differential surface energy may translate into a more aggressive recoiling motion, and hence an increased tendency for droplet bouncing. Since the surface energy of a deformed droplet on surface is a function of the static droplet-surface contact angle, a quantitative measurement of the droplet-surface wetting, the effect

of wetting on bouncing is therefore implied. Specifically, improving the droplet-surface wetting should reduce the differential surface energy and retard bouncing.

III. The effect of surface roughness on bouncing is represented by the roughness-induced changes in droplet-surface wetting during deposition. Specifically, the gases trapped in the defects on a rough surface result in interfacial voids that prevent the deposited droplet from wetting the surface completely. The extent of the roughness-induced incomplete wetting can be quantified by the effective area fraction, defined as the ratio between the actual melt-surface contact area and the total area of a rough surface. The effective area fraction is shown to be proportional to the melt penetration into the surface defects. By modeling the characteristic defect of an actual rough surface as a conical notch, the melt penetration, and hence the effective area fraction, can be estimated analytically. The analysis shows that the melt penetration is a strong function of the surface defect geometry. Inspection of the bump-surface interfaces suggests that increase in the surface roughness is characterized by deeper defects with shallow slopes. The net effect of surface roughness on wetting is quantified by calculating the adjusted contact angle as a function of the effective area fraction. The analytical results suggest that an increase in surface roughness deteriorates droplet-surface wetting, and hence increases the potential for bouncing.

IV. The normalized differential surface energy, representing the non-dimensional form of the potential for bouncing, is adapted as a bouncing criterion. The bouncing criterion is expressed as a function of the intrinsic or the roughness-adjusted droplet-surface contact angle for a given set of droplet impact conditions. Improving the droplet-surface wetting and reducing the surface roughness decrease the bouncing criterion value, and hence suggest a reduced tendency for a deposited droplet to bounce.

The hypotheses proposed are verified by data obtained from the experimental portion of the present study, which consists of a bump morphology study and a high-speed imaging investigation of the droplet deposition behavior. The observations and conclusions drawn from them are presented below.

V. The morphologies of solder bumps formed on the prepared surfaces are shown to change from well-formed spherical caps to irregular splats and remnants of bounced droplets as

either the surface wetting condition deteriorates or the surface roughness increases. The observed changes in bump morphologies suggest a transition from droplet sticking to bouncing as the prevalent deposition behavior. Therefore, the results qualitatively confirm the general trends predicted by the analytical models.

VI. High-speed images of droplet deposition show that droplet bouncing is preceded by greater and faster base retraction, severely distorted droplet shape and more pronounced upward flow of the deposited melt. These observations therefore verify the hypotheses that droplet bouncing is a severe form of droplet recoiling after the initial, post-impact spreading.

VII. The droplet surface area evolution, extrapolated from the high-speed images, verifies quantitatively that the tendency for bouncing increases as the surface area difference between the maximum spreading and equilibrium states of a deposited droplet becomes greater. The greater surface area difference suggests an increase in the associated differential surface energy, which is verified by analyzing the surface energy dynamics of the deposited droplets empirically. Therefore, the droplet bouncing behavior is positively correlated with an increase in the differential surface energy.

VIII. The assumed correlation between the surface roughness and the characteristic defect geometry is verified by profiling the prepared rough surfaces using an optical profilometer. The 3-D profiles generated confirm qualitatively that as the surface roughness increases, the characteristic defects change from small indentations with steep slopes to deep notches with shallow slopes.

IX. The concept of incomplete droplet-surface wetting induced by roughness during droplet deposition is verified by simulating the actual rough surfaces with the proposed notched surface model and estimating the extent of melt penetration into the surface defect. The results confirm that an increase in surface roughness reduces melt penetration, and hence decreases the effective area fraction. The impact of roughness on wetting is quantified by calculating the adjusted contact angles using the estimated effective area fraction. The analytically determined angles are compared with the empirical measurements and are found to be in good agreement.

X. The bouncing criterion for droplets deposited in the high-speed imaging experiments is calculated based on the impact conditions and the target surface properties. The calculated values are shown to match the analytically predicted trends. Specifically, improving surface wetting and decreasing surface roughness are shown to decrease the potential for bouncing. A regime between criterion values of 0.05 and 0.08 is identified as a threshold of transition, indicating a shift from droplet sticking to bouncing. Consequently, droplet bouncing may become prevalent when bumping is conducted in this regime and hence process parameters may need to be modified accordingly.

5.2 Future Work

Based on the findings in this study, several areas of future work are identified below.

The current analytical model appears to overestimate the maximum spreading diameter of a deposited droplet. Since the bouncing criterion is a function of the maximum spreading factor, this deficiency degrades the accuracy of the analytical predictions. The error is most likely due to the insufficient sophistication in the modeling of viscous dissipation during spreading. Future improvement in this area is recommended.

The threshold indicating the transition from droplet sticking to bouncing behavior is currently represented as a range of bouncing criterion values. The ability to refine this range further is hindered by the lack of empirical data in this transition regime; information which hopefully will be amended by future investigations. It may be noted that the transition from sticking to bouncing may not occur at an exact point, since the phenomenon may be intrinsically random. However, this speculation needs to be verified by additional droplet deposition experiments in this regime.

Irregularities in the droplet deposition behavior on rough surfaces also require further examination. Specifically, droplets deposited on sandblasted surfaces sometimes fail to rebound, even when the wetting conditions suggest strong tendency for bouncing. The phenomenon suggests that the deposited droplets may be subjected to greater dissipation. There are two possible sources of increase in dissipation. First, the flow front instabilities observed on a droplet deforming on a rough surface signify that the droplet's internal fluid flows may have

been disturbed by the surface defects and become increasingly turbulent. The consequent unsteady fluid motions may have increased the amount of internal dissipation and reduced the potential for bouncing. Second, the rough surface may have induced greater dissipation by increasing the shear force at the droplet-surface interface during spreading and recoiling. Analogous to flow in a rough pipe, it is clear that roughness will only affect the flow resistance if the surface protrusions are at least similar in size as the laminar sublayer, i.e. $k = \delta$, where k is the height of a protrusion and δ is the boundary layer thickness [Schlichting, 1968]. k may be represented by the 10-point height, Rz of a roughened surface in this case, while δ may be estimated by the boundary layer thickness during droplet spreading, approximated by Pasandideh-Fard *et al.* [1996]

$$\delta = 2\frac{D_{ini}}{\sqrt{\mathrm{Re}}} \tag{5.1}$$

Based on the typical impact condition of a UDS droplet, δ is estimated to be around 6-10μm. The roughest surface used in the current experimental study, the 180μm Al_2O_3 sandblasted surface, has an average Rz of approximately 6-7μm. Therefore, it is possible that the surface roughness may have increased the flow resistance during droplet spreading and recoiling, and hence increased dissipation. Since greater dissipation may retard droplet bouncing, further investigations are strongly recommended to study the effect of roughness on dissipation during droplet deposition.

REFERENCES

Ablett, R., 1923, "An investigation of the angle of contact between paraffin wax and water," *Philos. Mag.*, vol. 46, pp. 244-256.

ANSI/ASME B46.1-1985, *Surface Roughness, Waviness, and Lay*, American National Standard Institute.

Aziz, S.D. and Chandra, S., 2000, "Impact, recoil and splashing of molten metal droplets," *International Journal of Heat and Mass Transfer*, vol. 43, pp. 2841-2857.

Bakoglu, H.B., 1990, *Circuits, Interconnections, and Packaging for VLSI*, Addison-Wesley, pp. 416-421.

Bennett, T. and Poulikakos, D., 1993, "Splat-quench solidifcationL estimating the maximum spreading of a droplet impacting a solid surface," *Journal of Materials Science*, vol. 28, pp. 963-970.

Bernardin, J.D., Stebbins, C.J., Mudawar, I., 1997, "Effects of surface roughness on water droplet impact history and heat transfer regimes," *Int. J. Heat Mass Transfer.*, vol. 40, no. 1, pp.73-88.

Cassie, A.B.D. and Baxter, S., 1944, *Trans. Faraday Soc.*, vol. 3, p. 11.

Chandra, S. and Avedisian, C.T., 1991, "On the collision of a droplet with a solid surface," *Proc. R. Soc. Lond.* A, vol. 432, pp. 13-41.

Chen, C.-A., 1996, "Droplet solidification and its effects on deposit microstructure in the uniform droplet spray process," Ph.D. Thesis, Massachusetts Institute of Technology, Cambridge, MA.

Chen, Y.Y. and Duh, J.-G., 2000, "The effect of substrate surface roughness on the wettability of Sn-Bi solders," *Journal of Materials Science: Materials in Electronics*, vol. 11, pp. 279-283.

Chun, J.-H. and Passow, C.H., 1992, "Study of spray forming using uniform droplet sprays," *Advances in Powder Metallurgy*, vol. 1, *Powder Production and Spray Forming*, pp. 377-391.

Drelich, J., Wilbur, J.L., Miller, J.D., and Whitesides, G.M., 1996, "Contact angles for liquid drops at a model heterogeneous surface consisting of alternating and parallel hydrophobic/hydrophilic strips," *Langmuir*, vol. 12, pp. 1913-1922.

Dussan V., E.B., 1979, "On the spreading of liquids on solid surfaces: static and dynamic contact lines," *Ann. Rev. Fluid Mech.*, vol. 11, pp. 371-400.

Elliot, G.E.P. and Riddiford, A.C., 1967, "Dynamic contact angles. I. The effect of impressed motion," *J. Colloid Interface Sci.*, vol. 23, pp. 389-398.

Engel, O.G., 1955, "Waterdrop collisions with soild surfaces," *Journal of Research of the National Bureau of Standards*, vol. 54, p.281.

Fukai, J., Zhao, Z., Poulikakos, D., Megaridis, M., and Miyatake, O., 1993, "Modeling of the deformation of a liquid droplet impinging upon a flat surface," *Phys. Fluids*, A, vol. 5, no. 11, pp. 2588-2599.

Harkins, W.D., *The Physical Chemistry of Surface Films*, Reinhold Publishing Corp., New York, pp. 80-82.

Harlow, F.H. and Shannon, J.P., 1967, "The splash of a liquid drop," *Journal of Applied Physics*, vol. 38, p. 3855.

Hayes, D.J., Wallace, D.B., Boldman, M.T., and Marusak, R.E., 1993, "Picoliter solder droplet dispensing," *International Journal of Microcircuits and Electronic Packaging*, vol. 16, no. 3, pp. 173-180.

Hukai, J., Shiiba, Y., Yamamoto, T., Miyatake, O., Poulikakos, D., Megaridis, C.M., and Zhao, Z., 1995, "Wetting effects on the spreading of a liquid droplet colliding with a flat surface: experiment and modeling," *Phys. Fluids*, vol. 7, no. 2, pp. 236-247.

Johnson, R.E. Jr. and Dettre, R.H., 1969, *Surf. Colloid Sci.*, vol. 2, p. 85.

Jones, H., 1971, "Cooling, freezing and substrate impact of droplets formed by rotary atomization," *J. Phys. D: Appl. Phys.*, vol. 4, pp. 1657-1660.

Kim, H.-Y., 1999, "Spreading behavior of molten metal microdroplets," Ph.D. Thesis, Massachusetts Institute of Technology, Cambridge, MA.

Kim, H.-Y., Feng, Z.C., and Chun, J.-H., 2000, "Instability of a liquid jet emerging from a droplet upon collision with a solid surface," *Physics of Fluids*, vol. 12, no. 3, pp. 531-541.

Lau, J.H. and Pao, Y.H., 1997, Solder Joint Reliability of BGA, CSP, Flip Chip, and Fine Pitch SMT Assemblies, McGraw-Hill, New York.

Lau, J.H., 2000, *Low Cost Flip Chip Technologies*, McGraw-Hill, New York.

Levin, Z.. and Hobbs, P.V., 1971, "Splashing of water drops on solid and wetted surfaces: hydrodynamic and charge separation," *Philosphical Transactions of the Royal Society of London*, A, vol. 269, pp. 555-585.

Liu, Q., Huang, C., and Orme, M., 2000, "Mutual electrostatic interactions between closely spaced charged solder droplets," *Atomization and Sprays: Journal of the*

International Institutions for Liquid Atomization and Spray Systems, vol. 10, no. 6, pp. 565-585.

Madejski, J., 1976, "Solidifcation of droplets on a cold surface," *Int. J. Heat Mass Transfer*, vol. 19, pp. 1009-1013.

Manufacturing Challenges in Electronic Packaging, 1998, eds. Lee, Y.C. and Chen, W.T., Chapmen & Hall.

Mao, T., Kuhn, D.C.S., Tran. H., 1997, "Spread and rebound of liquid droplets upon impact on flat surfaces," *AIChE Journal*, vol. 43, no. 9, pp. 2169-2179.

Marmanis, H. and Thoroddsen, S.T., 1996, "Scaling of the fingering pattern of an impacting drop," *Phys. Fluids*, vol. 8, no. 6, pp. 1344-1346.

Marmur, A., 1994, "Thermodynamic aspects of contact angle hyteresis," *Advances in Colloid and Interface Science*, vol. 50, pp. 121-141.

Marx, D.R., Lateef, A., and Clarke, A., 1998, "Sputtering deposits evaporation-quality UBM for flip-chip," *Semiconductor International*, vol. 21, no. 3, pp. 97-101.

McPherson, R., 1980, *J. Mater. Sci.*, vol. 15, p.3141.

Miller, L.F., 1969, "Controlled collapse reflow chip joining," *IBM J. Res. Dev.*, pp.239-250.

Morton, R.K., 2002, "Topography of surfaces," *ASM Handbook Volume 5: Surface Engineering*, ASM International, Materials Park, OH.

Mundo, C.H.R., Sommerfeld, M., and Tropea, C., 1995, "Droplet-wall collisions: experimental studies of the deformation and breakup process," *Int. J. Multiphase Flow*, vol. 21, no. 2, pp. 151-173.

Nakae, H., Inji, R., Hirata, Y., and Saito, H., 1998, "Effects of surface roughness on wettability," *Acta mater.*, vol. 46, no. 7, pp. 2313-2318.

NewView 5000 Operating Manual OMP-0423E, 2000, Zygo Corporation, Middlefield, CT.

Pasandideh-Fard, M., Qiao, Y.M., Chandra, S., and Mostaghimi, J., 1996, "Capillary effects during droplet impact on a solid surface," *Phys. Fluids*, vol. 8, no. 3, pp. 650-659.

Passow, C.H., 1992, "A study of spray forming using uniform droplet sprays," M.S. Thesis, Massachusetts Institute of Technology, Cambridge, MA.

Prasher, R.S., 2001, "Surface chemistry and characteristics based model for the thermal contact resistance of fluidic interstitial thermal interface materials," *Journal of Heat Transfer*, vol. 123, pp. 969-975.

Schiaffino, S. and Sonin, A.A., 1997, "Molten droplet deposition and solidification at low Weber numbers," *Phys. Fluids*, vol. 9, no. 11, pp. 3172-3187.

Shakeri, S. and Chandra, S., 2002, "Splashing of molten tin droplets on a rough steel surface," *International Journal of Heat and Mass Transfer*, vol. 45, pp. 4561-4575.

Shin, J.H., 1998, "Feasibility study of rapid prototyping using the uniform droplet spray process," B.S. Thesis, Massachusetts Institute of Technology, Cambridge, MA.

Shuttleworth, R. and Bailey, G.L.J., 1948, *Disc. Faraday Soc.*, vol. 3, 16.

Stow, C.D. and Hadfield, M.G., 1981, "An experimental investigation of fluid flow resulting from the impact of a water drop with an unyielding dry surface," *Proc. R. Soc. Lond.* A, vol. 373, pp. 419-441.

Tatsumi, K., Yamamoto, Y., Hashino, E., and Shimokawa, K., 2001, "Micro-ball bumping technology," *Nippon Steel Technical Report*, no. 84, pp. 46-52.

The National Technology Roadmap for Semiconductors 1994, Semiconductor Industry Association, San Jose, CA.

Thoroddsen, S.T. and Sakakibara, J., 1998, "Evolution of the fingering pattern of an impacting drop," *Physics of Fluids*, vol. 10, no. 6, pp. 1359-1374.

Trapaga, G. and Szekely, J., 1991, "Matnematical modeling of the isothermal impingement of liquid droplets in spraying processes," *Metallurgical Transactions*, B, vol. 22, no. 6, pp. 901-914.

Tsurutani, K., Yao, M., Senda, J., and Fujimoto, H., 1990, "Numerical analysis of the deformation process of a droplet impinging upon a wall," *JSME International Journal, II*, vol. 33, no. 3, pp. 555-561.

Vigness-Adler, M., 2002, "Physico-chemical aspects of forced wetting," *Drop-Surface Interactions*, pp. 103-157, eds. M. Rein, Springer Wien, New York.

Waldvogel, J.M. and Poulikakos, D., 1997, "Solidifcation phenomena in picoliter size solder droplet deposition on a composite substrate," *Int. J. Heat Mass Transfer*, vol. 40, no. 2, pp. 295-309.

Wang, G.-X. and Matthys, E.F., 1996, "On the heat transfer at the interface between a solidifying metal and a solid substrate," in Melt Spinning, Strip Casting and Slab Casting, ed. by Matthys, E.F. and Truckner, W.G., The Minerals, Metals & Materials Society, pp. 205-236.

Wenzel, R.N., 1936," Resistance of solid surfaces to wetting by water," *Industrial and Engineering Chemistry*, vol. 28, no. 8, pp. 988-994.

Wilson, S.D.R., 1975,"A note on the measurement of dynamic contact angles," *J. Colloid Interface Sci.*, vol. 51, pp. 532-534.

Wilson, T. and Sheppard, C.J.R., 1984, *Theory and Practice of Scanning Optical Microscopy*, Academic, New York.

Worthington, A.M., 1876, "On the form assumed by drops of liquids falling vertially on a horizontal plate," *Proceedings of the Royal Society of London*, vol. 25, pp. 261-272.

APPENDIX

Jones [1971] evaluated the viscous dissipation in his study on the flattening of rotary atomized droplets by modeling the deforming droplet as a disk of viscous fluid being flattened between two parallel plates. By assuming the flattening rate to be half of the impact velocity, u_{ini}, the viscous energy dissipated was estimated as

$$Diss_{1-2} = \frac{\pi}{198} \mu u_{ini} \frac{D_{ini}^{6}}{h} \tag{A.1}$$

where μ and h are fluid viscosity and splat height, respectively. The formulation is simple but its validity is questionable. First, the hydrodynamic situation simulated by the parallel plate hypothesis is not considered comparable with the fluid flow behavior of a post-impact, spreading droplet. Second, the low flattening rate assumed results in a relatively slow and steady radial droplet spreading rate. This slow spreading assumption contradicts with most empirical observations, which typically identify a fairly high initial expansion rate followed by rapid deceleration [Engel, 1955; Slow and Hadfield, 1981]. The lower spreading speed assumed in the model would underestimate the viscous dissipation and overestimate the flattening ratio. The fact that Jones' predictions fail to match the experimental results [McPherson, 1980], yielding splat thickness 5 times less than the typically observed values, appears to confirm the deficiency of the dissipation model.

Chandra and Avedisian [1991] incorporated viscous dissipation in their estimation of the spreading factors of n-heptane droplets impinging on hot surfaces. They approximated the viscous energy lost in deforming a droplet during impact as

$$Diss_{1-2} = \int_{0}^{t_s} \int_{v} \varphi \, dv \, dt \approx \varphi v t_s \tag{A.2}$$

Assuming a linear vertical velocity gradient, the dissipation function, φ, is given by

$$\varphi = \mu\left(\frac{\partial u_i}{\partial x_j} + \frac{\partial u_j}{\partial x_i}\right)\frac{\partial u_i}{\partial x_j} \approx \mu\left(\frac{u_{ini}}{h}\right)^2 \tag{A.3}$$

where u_{ini} and h are droplet impact velocity and height of a flattened droplet at its maximum spreading diameter, D_{max}, respectively. The volume of flattened droplet, v is determined as,

$$v = \frac{\pi}{4} D_{max}^2 h \tag{A.4}$$

while the spreading time, t_s is estimated by the time taken for the height of the impinging droplet to go from its initial diameter, D_{ini} to 0 assuming a constant velocity of u_{ini},

$$t_s \approx \frac{D_{ini}}{u_{ini}} \tag{A.5}$$

Combining Equations A.3, A.4, A.5, and Equation A.2 gives the viscous dissipation as

$$Diss_{1-2} = \frac{\pi}{4} D_{ini}\left(\frac{D_{max}^2}{h}\right)\frac{\mathrm{We}}{\mathrm{Re}} \tag{A.6}$$

Chandra and Avedisian's dissipation model may be verified by comparing their predicted spreading factors with the experimental data. However, their model predicts 20 to 40% greater than the empirical measurements, suggesting that the model underestimate viscous dissipation. The discrepancy is most likely a result of underestimating the shear stress in the viscous boundary layer by assuming the boundary layer to be the full thickness of the spreading droplet, *h*. In addition, their rudimentary treatment of the spreading time may also have underestimated the spreading time of a deforming droplet.

Pasandideh-Fard et al. [1996] refined Chandra and Avidisian's dissipation model by addressing the aforementioned modeling issues. By assuming the fluid motion inside an impinging droplet as axisymmetric stagnation point flow, the viscous boundary layer thickness is estimated as

$$\delta = \frac{2D_{ini}}{\sqrt{\text{Re}}} \tag{A.7}$$

The volume of the viscous fluid, v, is hence redefined as

$$v = \frac{\pi}{4} D_{max}^2 \delta \tag{A.8}$$

The spreading time, t_s is estimated by assuming the droplet spreads into cylindrical disk of diameter D and height h, as shown in Figure A.1. Based on conservation of mass and assuming an average value of $d \approx D_{ini}/2$, the droplet spreading rate can be represented as

$$\frac{dD}{dt} = \frac{3u_{ini} D_{max}^2}{16 D_{ini} D} \tag{A.9}$$

Integrating Equation A.9 from 0 to D_{max} gives the spreading time as

$$t_s = \frac{8}{3}\left(\frac{D_{ini}}{u_{ini}}\right) \tag{A.10}$$

Modifying Chandra and Avidisian's model by incorporating Equation A.7, A.8 and A.10, Pasandideh-Fard et al. expressed the viscous dissipation during droplet spreading as

$$Diss_{1-2} = \frac{\pi}{3} \frac{\rho u_{ini}^2 D_{ini} D_{max}^2}{\sqrt{\text{Re}}} \tag{A.11}$$

Rearranging terms in Equation A.11 yields the expression shown in Equation 2.37. Since the estimations for both the viscous boundary layer thickness and spreading time are improved in the current dissipation model, the prediction accuracy is expected to be enhanced as well. Pasandideh-Fard et al. have reported good agreement between the spreading factors predicted using this refined dissipation model and the experimental results.

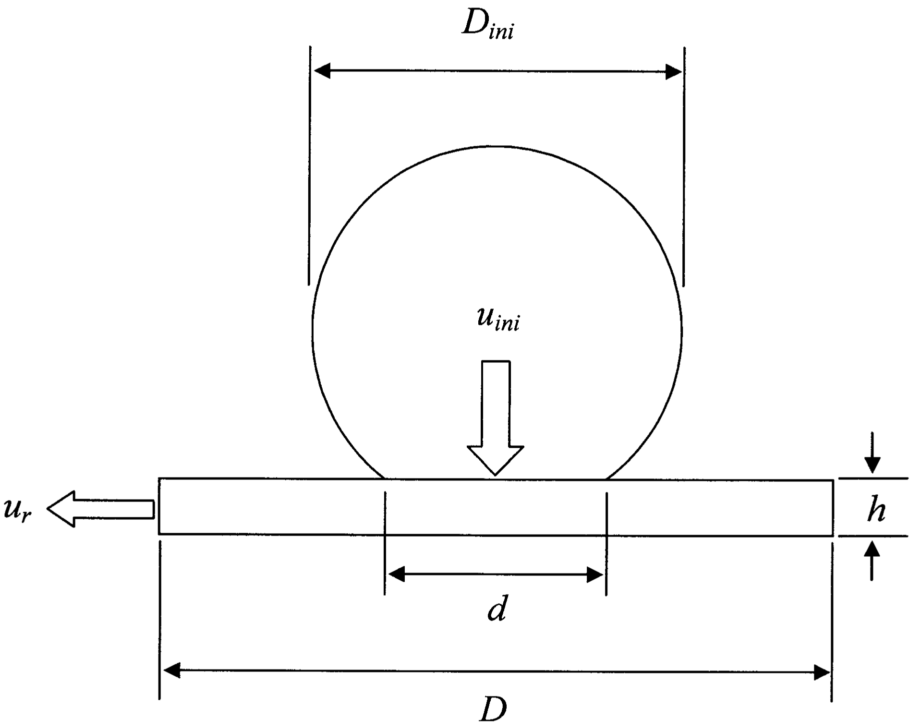

Figure A.1. Droplet spreading model for spreading time estimation [Pasandideh-Fard et al.].